4-23-2015

Wireless Simultaneous Stimulation-and-Recording Device (SRD) to Train Cortical Circuits in Rat Somatosensory Cortex

John T. Ramshur

WIRELESS SIMULTANEOUS STIMULATION-AND-RECORDING DEVICE (SRD) TO TRAIN CORTICAL CIRCUITS IN RAT SOMATOSENSORY CORTEX

by
John T. Ramshur

A Dissertation
Submitted in Partial Fulfillment of the
Requirements for the Degree
Doctor of Philosophy

Major: Biomedical Engineering

The University of Memphis
May 2015

ACKNOWLEDGEMENTS

I would like to thank my advisors Amy de Jongh Curry, Ph.D. and Robert Waters, Ph.D. for providing help and guidance throughout the entire project. I would also like to thank my additional committee members Bashir Morshed, Ph.D. and Eddie Jacobs, Ph.D. for their guidance and insights about the project. I would like to thank Cheng Li, M.D. for his patience and for sharing his knowledge of animal surgery procedures. For help with circuit related questions I would like to thank Sergi Pacareu and Israel Quintal.

ABSTRACT

Ramshur, John Thomas. Ph.D. The University of Memphis. May 2015. Wireless Simultaneous Stimulation-and-Recording Device to Train Cortical Circuits in Rat Somatosensory Cortex. Major Professor: Amy L. de Jongh Curry, Ph.D.

The primary goal of this project is to develop a wireless system for simultaneous recording-and-stimulation (SRD) to deliver low amplitude current pulses to the primary somatosensory cortex (SI) of rats to activate and enhance an interhemispheric cortical pathway. Despite the existence of an interhemispheric connection between similar forelimb representations of SI cortices, forelimb cortical neurons respond only to input from the contralateral (opposite side) forelimb and not to input from the ipsilateral (same side) forelimb. Given the existence of this interhemispheric pathway we have been able to strengthen/enhance the pathway through chronic intracortical microstimulation (ICMS) in previous acute experiments of anesthetized rats. In these acute experiments strengthening the interhemispheric pathway also brings about functional reorganization whereby cortical neurons in forelimb cortex respond to new input from the ipsilateral forelimb. Having the ability to modify cortical circuitry will have important applications in stroke patients and could serve to rescue and/or enhance responsiveness in surviving cells around the stroke region. Also, the ability to induce functional reorganization within the deafferented cortical map, which follows limb amputation, will also provide a vehicle for modulating maladaptive cortical reorganization often associated with phantom limb pain leading to reduced pain. In order to increase our understanding of the observed functional reorganization and enhanced pathway, we need to be able to test these observations in awake and behaving animals and eventually study how these changes persist over a prolonged period of time. To accomplish this a system was needed to allow

simultaneous recording and stimulation in awake rats. However, no such commercial or research system exists that meets all requirements for such an experiment. In this project we describe the (1) system design, (2) system testing, (3) system evaluation, and (4) system implementation of a wireless simultaneous stimulation-and-recording device (SRD) to be used to modulate cortical circuits in an awake rodent animal model.

TABLE OF CONTENTS

LIST OF TABLES

LIST OF FIGURES

LIST OF ABBREVIATIONS

ALBSF	anterior lateral barrel subfield
BT	Bluetooth
BCI	brain computer interface
BMI	brain machine interface
CPU	central processing unit
CNS	central nervous system
EIB	electrode interface board
FBS	forepaw barrel subfield
GABA	gamma-aminobutyric acid
GPIO	general purpose input/output
GUI	graphical user interface
HBS	hindpaw barrel subfield
IACUC	Institutional Animal Care and Use Committee
IDE	integrated development environment
ICMS	intracortical microstimulation
i.m.	intramuscular
IR	infrared
kPBS	potassium phosphate buffered saline
LiPo	lithium polymer
LLBSF	lower lip barrel subfield
LTP	long term potentiation
LDO	low drop-out
mux	multiplexer
NaPBS	sodium phosphate buffered saline
PCB	printed circuit board
PMBSF	posterior medial barrel subfield
PSoC	programmable system on a chip
QFN	quad-flat no lead
RF	receptive field
SPI	serial peripheral interface
SPP	serial port profile
SRD	stimulation and recording device
UART	universal asynchronous receiver/transmitter

1. Introduction

1.1 Rodent Barrel Cortex Model System

The primary somatosensory cortex (SI), a distinct area of the cerebral cortex, processes sensations related to touch, temperature, pain, vibration, and proprioception. Neurons of the mammalian cortex are cytoarchitecturally arranged in a series of six horizontal layers respectively labeled layers I-VI with layer I being the closet to the cortical surface [1]. An additional functional organization exist in SI cortex whereby a topographical map of the skin surface is represented in SI cortex [2]. Functional groupings of neurons are associated with specific contralateral body skin surface representation. In rat SI these groupings can be visualized within cortical layer IV by regions of cortex that stain dark with cytochrome oxidase (CO) and are surrounded by cell-dense walls. The term barrel is often used to describe these cell groupings due to their barrel-like shape as originally observed by Woolsey and Van der Loos when they described barrel structures related to the whiskers in the mouse [3]. Others then described barrel-like subfields associated with the representation of the forepaw [4–6] and hindpaw [7] in rats. The forepaw barrel subfield (FBS) in rat consist of nearly 25 barrels that are associated with regions of the forepaw skin surface [6,8]. Posterior to the FBS is a less organized region of diffuse labeling that is associated, in part, with the somatotopic representation of the wrist, followed by forearm, upper arm, and shoulder, respectively [9]. Figure 1 shows the organization of rat barrel cortex which also includes the posterior medial barrel subfield (PMBSF) and anterior lateral barrel subfield (ALBSF) associated with whiskers and sinus hairs on the face, respectively, lower lip barrel subfield (LLBSF)

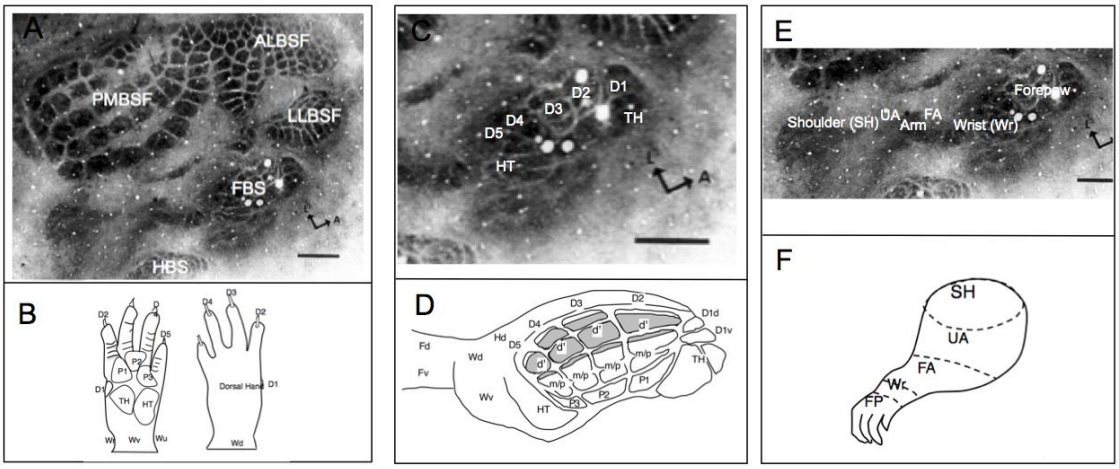

Figure 1. Photomicrographs and illustrations of rat barrel cortex. (A) Cytochrome oxidase (CO) stained section of the barrel field showing the locations of the FBS and other subfields. (B) Line drawing showing ventral glabrous and dorsal hairy skin surfaces of the forepaw along with nomenclature. (C) Photomicrograph showing the FBS along with the location of digit and pad representations. (D) Line drawing reconstruction showing locations of forepaw digits, palmar and digit pads, wrist, and forearm representations in C. (E) Location of the forelimb and shoulder representation in barrel cortex. (F) Line drawing showing forelimb and shoulder nomenclature in E. Adapted from Waters et al. 1995 [6]. Legend: posterior medial barrel subfield (PMBS), anterior lateral barrel subfield (ALBS), lower lip barrel subfield (LLBSF), forepaw barrel subfield (FBS), digits 1-5 (D1-D5), hyperthenar (HT), thenar (TH), pad 1-3 (P1-P3), radial wrist (Wr), unlar wrist (Wu), ventral wrist (Wv), dorsal wrist (Wd), forearm distal (Fd), forearm ventral (Fv), digit 1 dorsal, (D1d), digit 1 ventral (D1v), shoulder (SH), upper arm (UA), forearm (FA), wrist (Wr), forepaw (FP).

associated with the jaw and hair on the chin, and the hind paw barrel subfield associated with the representation of the hind paw.

Vertically organized modules called cortical columns are considered as the basic functional unit of cortical processing and extend across all layers of the cortex [10,11]. The barrel cortex is no exception to this, but has the advantage of being a visible form of this functional columnar organization [12]. This feature provides a convenient model to study the link between cortical structure and function.

Cutaneous sensory neurons originating at the periphery make synaptic connections at the spinal cord and in nuclei of the brainstem and thalamus in route to SI cortex. Afferent signals from peripheral receptors including mechanoreceptors (mechanical), thermoreceptors (thermal), nociceptors (pain), proprioceptors (limb position/location), and Pacinian (vibration) are carried by the dorsal column pathway and the spinothalamic (anterior and lateral) pathway [2,13,14]. Of interest to this study are the receptors responsible for the sensation of touch and vibration. Axons carrying signals from rat forelimb mechanoreceptors enter the spinal cord via a dorsal root and terminate in the dorsal horn [14]. Secondary projections from the dorsal horn travel ipsilateral and anterior in the spinal cord via the aforementioned dorsal column pathway and terminate in the ipsilateral brainstem within a sub-nucleus of the dorsal column nuclei called the cuneate nucleus [14,15]. Tertiary projections then terminate within the ventroposterio lateral (VPL) nucleus of the contralateral thalamus [16–20]. Finally, afferent neurons originating in thalamic VPL terminate in SI cortex [14,21–23]. Thalamocortical neurons terminate in various cortical layers within the rat SI cortex with layer IV receiving the

largest number of inputs [24,25]. Layer IV excitation then spreads to other cortical layers II/III, IV, and V [26–30], but more prominently to layer II/III [31].

1.2 Interhemispheric Connectivity

Early evidence of somatotopic input projections in cats suggested that SI cortex received and responded only to input from the contralateral skin surface [32,33]. Since that time others have reported that SI cortex does receive bilateral somatotopic input, although predominately contralateral input, in cat [34,35], monkey [36–40], flying fox [41,42], and rodent [43–47]. Connections that travel between hemispheres via the corpus callosum were shown primarily associated with representations of the midline such as the trunk, face, or head and not found in cortical regions associated with the limb [35,48,49]. However, more recent studies have established that bilateral sensory input does exist for the forelimb in cat [35,50,51], monkey [37,38,52], and flying fox [41]. In rat SI cortex bilateral somatotopic input has been described for hindlimb [44,46,47] and whisker [43,45].

Pidoux and Verley reported that ablation of rat whisker SI cortex contralateral to the whisker of interest eliminates ipsilateral evoked response to ipsilateral stimuli [37,43]. Similarly, Innocenti reported that interrupting interhemispheric communication with corpus callosum blockade greatly reduced ipsilateral evoked response to forepaw stimulation in cat [34]. A More recent functional imaging study by Pelled and colleagues showed that, in rats, partial denervation of the hindpaw or forepaw resulted in activation in the contralateral SI cortex as expected and that complete denervation of the hindpaw or forepaw resulted in bilateral activation when the intact forelimb paw was stimulated [53]. Furthermore, Pelled and colleagues reported that if the SI representation of the intact limb

was subsequently lesioned that ipsilateral activation was no longer detected [53]. Together, these findings suggest that ipsilateral responses are mediated via the corpus callosum and thus provide a substrate build our theory that modifying the interhemispheric connection between homotopic SI areas could lead to functional reorganization when that circuit is trained with the SRD in awake animals.

1.3 Cortical Reorganization

The somatosensory cortex is a dynamic system capable of adapting and reorganizing in response to experience and use. The term plasticity is often used to describe the brains ability to adapt. Forms of plasticity can range from functional modifications of existing synapses and neurons that alter neuronal excitability [54,55] to structural changes that cause physical rewiring of cortical circuits by establishing/removing synapses and morphological changes such as rewiring of the auditory cortex to process visual information [56]. Cortical reorganization and cortical plasticity are often used interchangeably. However, in this study cortical reorganization is used to describe plasticity that relates to the reorganizing of limb representations in areas of SI cortex or representational organization. Representational organization can occur after altering peripheral input to the deafferented SI cortex by nerve transection [57,58], digit amputation [59–61], forelimb amputation [9,62,63] whereby cells that responded to only one area of the forelimb skin surface before the loss of input begin to respond to neighboring forelimb skin representation. For example, Kalaska and Pomeranz showed that nerve transections of the nerves to the front paw caused cells within the paw representation in SI cortex to become responsive to electrical stimulation of the nerves of forearm [57]. Similarly, Merzenich et al. describe reorganization of monkey SI forelimb

cortex following median nerve transection where surrounding skin surface representations of digits 1 and 2 dorsal surfaces and hypothenar eminence expanded into the former median nerve zone that were not represented in that region prior to transection [64]. In rat, McCandlish et al showed that one month following the removal of digit 3 the representations of neighboring digits 2 and 4 expanded into the former representation of digit 3 [59].

1.4 Mechanisms of Cortical Reorganization

A balance of both excitatory and inhibitory influences determines the current state of neuron membrane potentials. Here we describe mechanism that account for increases in cortical responsiveness by the strengthening of excitatory connections and/or removal of inhibitory influences.

Long-term Potentiation

Long-term potentiation (LTP) is defined as a persistent strengthening of synapses based on recent patterns of activity [2]. With increased levels of excitability, such as repetitive stimulation, LTP occurs by the recruitment of additional N-methyl-D-aspartate (NMDA) receptors in the post-synaptic neuron or by increasing the size or number of synapses [2]. Potentiation produced by stimulation also follows the theory proposed by Hebb wherein the connection between two cells is strengthened when one cell repeatedly or persistently participates in the excitation and firing of a second cell [65]. LTP is a fundamental mechanism in the formation of memory and learning [66]. Synapses in rat barrel cortex experience LTP following tetanic stimulation of intracortical inputs [67,68]. Fetz and colleagues demonstrated that potentiation could be induced between both

primary motor cortices of monkey by delivering ICMS in one hemisphere that was dependent on the activity in the opposite hemisphere [69]. The result was that firing activity in the recording site began to resemble the activity in the stimulation site thus providing evidence of new synaptic connections.

Long-term Depression

Conversely, NMDA receptors and/or synaptic connections are reduce in long term depression (LTD) thus causing the synaptic connection to becomes less effective at producing activation [2]. High frequency stimulation has been indicated in several studies to induce LTP [70–72]. However, chronic microstimulation can also produce plasticity in the form of LTD [73] of synaptic efficiency of both excitatory and inhibitory connections [74]. Previous studies suggest that LTD following chronic stimulation occurs when the pathway being stimulated has both monosynaptic excitation and disynaptic inhibition and is facilitated by an increased excitation of inhibitory interneurons [74]. Quairiaux et al. reported that 24 hours of chronic whisker stimulation in rodent caused depressed responsiveness and was likely brought about by an increase in spineous GABAergic synapses [75].

GABAergic Inhibition

It has been shown that inhibitory interneurons in SI cortex are GABAergic [46,76–80] and are capable of modulating receptive fields of SI cortical neurons [76,81]. GABA related inhibition in cortical plasticity plays a key role in modulating synaptic responsiveness. Blocking the influence of GABAergic inhibitory neurons by adding GABA antagonist to rat barrel cortex the probability of inducing LTP increased during

tetanus [82]. Also, GABA antagonist have been shown to enhance evoked responses [76] and increase the size of receptive fields in SI [81]. Reducing inhibition by blocking the first leg of the inhibitory disynaptic connection between contralateral SI cortices also causes an cells to become more responsive to subthreshold activity resulting in enlargement in receptive field sizes [46,55].

The relevance of GABA down regulation following sensory deprivation is strengthened by the fact that functional reorganization also occurs following sensory deprivation [62]. Thus changes in intracortical inhibitory networks are partially responsible for long-term cortical reorganization via direct changes to GABAergic neurons or by changes to inhibitory inputs. We plan to repetitively stimulate the callosal pathway of SI homotopic cortices and thereby modulate local inhibitory circuits in the ipsilateral forelimb SI cortex.

1.5 Chronic Repetitive Stimulation of Interhemispheric Pathway

ICMS consist of delivering small electrical pulses by a microelectrode to small populations of neurons. ICMS has been a useful tool in studying the functional significance of groups of neurons. For example, Stewart and Preston used ICMS to describe the functional coupling between pyramidal tract and segmental motor neurons in cat [83] and primate [84]. Many others have used ICMS for mapping motor cortex of various species [85–88], understanding input/output relationships in motor cortex [89], examining sensorimotor [90–94] and thalamocortical [95–97] connectivity, and characterizing cortical plasticity [69,71,73]. Others have used ICMS not to study function but to induce changes. For example, chronic or repetitive ICMS has been shown to increases neuronal firing rates [98], enhance efficiency of transcallosal pathway [74], and

induce long-term potentiation (LTP) within SI cortex [67,82,98]. As mentioned above, Fetz and colleagues used chronic ICMS to artificially connect two sites in motor cortex of awake monkeys that persisted for a week suggesting formation of new synaptic connections (39,40). We have previously shown that repetitive stimulation of layer V neurons in anesthetized rat barrel cortex leads to an enhancement of the transcallosal pathway between homotopic cortices whereby evoked response firing rates were increased [99]. In this proposal, we will confirm our previous results with a newly designed wireless, stimulating and recording device worn by awake rats.

We propose to design and implement a wireless simultaneous stimulation-and-recording device (SRD) that will stimulate a known cortical circuit, record from the cortical circuit to test for efficacy of stimulation as seen by enhanced responsiveness, and test whether stimulation leads to expression of new functional inputs.

1.6 Clinical Significance

In the United States alone there are an estimated 1.7 million amputees with an additional 185,000 new cases annually[100,101]. In 2009, the associative hospital cost for amputation totaled more than $8.3 billion [102]. Regardless of the cause of limb loss [103] approximately 70% of amputees suffer some form of phantom limb pain [104] whereby pain is sensed in the part of the limb that is missing. Phantom limb pain has been correlated with the cortical reorganization that occurs following limb loss. Additionally, approximately 6.8 million stroke survivors live in the Unites States and each year an estimated 800,000 suffer from stroke [105]. The total cost of stroke from 2005 to 2050, in 2005 dollars, is projected to be more than $2.2 trillion [106].

Maladaptive cortical reorganization and changes in neuronal pathways and synaptic connectivity of cortical circuits in SI cortex are central neurological consequences that often follow limb loss [107–110] and cortex related stroke injuries [111–114]. Development of compensation strategies and rehabilitation therapies that modulate cortical circuits will aid in therapeutic treatment of phantom limb pain that almost always follows limb amputation and the plasticity that occurs in surviving neurons around a region of stroke.

Long term goals of this project are to use the SRD to treat patients suffering from intractable stroke and phantom limb pain following limb loss. For example, the SRD could be used to activate neurons at the edge of a stroke territory in an attempt to enhance responsiveness of surviving neurons to replace some of the lost function. Similarly, the SRD could deliver new input to deafferented cortical regions that follow limb amputation to potentially relieve phantom limb pain by modulating maladaptive reorganization that accompanies loss of limb.

1.7 Brain Computer Interface Review

A brain computer interface (BCI) is a system that interfaces the brain with hardware and software. BCI systems have become important tools in neuroscience research to study cortical plasticity and neuro-modulation. In the proposed study we will use a BCI to enhance brain circuits that will lead to functional reorganization in the rat barrel field cortex.

BCI systems have become increasingly smaller and more power efficient to the point of being completely implantable [115–117]. Most BCI's used in research operate as a tethered device requiring a cabled connection between the device and computer

system [116,118–123]. Tethered systems have the advantage of uninterruptible power supplies and higher data bandwidth, but can limit an animal's range of motion in experiments requiring freely behaving animals. While wireless systems are less intrusive, they often require larger and more complex designs with shorter operating times and less data bandwidth [115,117,124–150]. Relative to this study, the greatest limiting feature found in most systems is the lack of simultaneous recording and stimulation. Systems that do offer both are either too large [131] for rat or are constructed using non-commercial components [115,116,120,121,123,126,134,135,138–140,142,145,148,149,151–164].

Another problem with existing BCI designs is the public availability and usability of the system itself or specific system components such as the central processing chip. The various processing chips used in BCI designs can be categorized within two types: commercially available integrated circuits (IC) or custom application specific IC's (ASIC). Commercial IC's typically include standard microcontrollers, systems-on-a-chip (SoC), and field programmable gate arrays (FPGA). SoC's such as Cypress Semiconductor's PSoC incorporate many analog and digital components into a single package allowing it to be used in a variety of applications. Microcontrollers and SoC's are widely available and offer user friendly design tool chains. FPGA's provide faster processing speeds but lack most analog features and require a steeper learning curve. ASIC's provide the maximum optimization in speed and power efficiency, but are cost prohibited for most users or are available to a select group of people [165]. An exception to the rule of cost and availability of ASIC chips is a recent commercial ASIC designed for biopotential signal applications manufactured by Intan Technologies. The Intan ASIC will be used for this project and its specifications will be discussed later.

BCI system specifications for the proposed study require that it is wearable by a rat, unobtrusive, and allows for simultaneous stimulation and recording. Of the systems developed for research or for commercial production, almost none have all of our required capabilities in a single package. The existing BCI's are either capable of only recording [116,117,119,120,125,126,128,133–136,138–142,145,147,148,150–152,155,157,163,164], capable of only stimulating [122,124,127,137,153,154,158–162], use non-commercial ASIC designs [115,116,120,121,123,126,134,135,138–140,142,145,148,149,151–164], or do not provide untethered use [116,118–123]. Of all the systems reviewed, only two come close to providing all the required features. The Neurochip BCI [131,143] has all the functionality requirements, but it is designed for primates and is much too large for use in rats. The Neurochip BCI also uses older microprocessor technology that would require upgrades. Getting the Neurochip BCI to a useful state for this project would require significant work. A BCI developed by Ye and colleagues is of the correct size and functionality, but has very poor battery life of less than two hours [129]. Additionally, timing of their BCI's on-board stimulator is controlled by off-circuit wireless timing. Because of the separate timing circuit and stimulator circuit, their device would fail to sync well with neural recordings as needed for this project. To overcome the limitations of current BCI systems, we are designing a BCI system that can functionally meet the aforementioned requirements while keeping the design open and available to others and usable for other biopotential signal applications. We are referring to our system as a stimulating and recording device (SRD) to distinguish it from other systems that do not support simultaneous stimulation and recording.

Other stimulation techniques are also available. Development of optogenetics [166–168] and introduction of a wireless system by Rogers and colleagues [169] hold great promise for asking specific kinds of research questions but its use in therapies is likely a long way off and will involve dealing with transfecting human neurons with viruses. Recent advances in transcranial magnetic stimulation (TMS) that combine positron emission tomography have permitted localization of stimulation sites within millimeters [170], but difficulty in stimulating deep structures and inaccessibility due to skull thickness offset some of its advantages. Deep brain stimulation (DBS) has been effective in treating medically refractory movement disorders [171] although cognitive declines have been reported with DBS treatment [172].

1.8 SRD Innovation

Methodologies based on recording and stimulation through microelectrodes and arrays are widely used to record and stimulate the nervous system both in-vivo and in-vitro. However, there is a rapidly growing need for neuroscience platforms, which can perform simultaneous chronic recording and stimulation of neural tissue in a completely wireless fashion together with signal processing to facilitate the analysis of the chronic recording data. Our proposed system fulfills this need while providing additional benefits.

Our platform will be made available to the public in an open format that uses commercially available hardware components and freely available software and source code. The recording subsystem's flexibility allows the SRD to be used for different types of signals such as neural action potentials, local field potential, ECG, EMG, EOG, and EEG and is not restricted to our application. Using the SRD for other biopotential signals requires no hardware changes, and filter bandwidths can be set using the graphical user interface or GUI.

2. SRD System Design

2.1 System Overview

The SRD is a wireless brain computer interface system that is capable of simultaneous stimulation and recording in rat cortex in awake rats. All components used to build the SRD are commercial-off-the-shelf (COTS) components. Figure 2 illustrates an overview of the SRD's various subsystems and component interconnections. Biopotential signals from biological tissue are amplified, filtered, and digitized by an integrated digital electrophysiology interface chip. Digitized data are transferred to the CPU via serial peripheral interface (SPI) communication to a core processor and then buffered and transmitted to a host PC via Bluetooth for visualization and offline analysis. Bluetooth communication is also used to send stimulation, recording, calibration, and filter settings to the SRD from a GUI. The SRD is capable of simultaneously recording from two channels at a maximum sample rate of 15 kilo-samples/second (ksps) per channel. Users can select any two channels from 12 available channels, or have the system sweep through all channels two at a time. Biological tissue stimulation is

delivered using an adjustable constant current stimulator capable of delivering ±255 μA of current with a compliance voltage up to ±10 V.

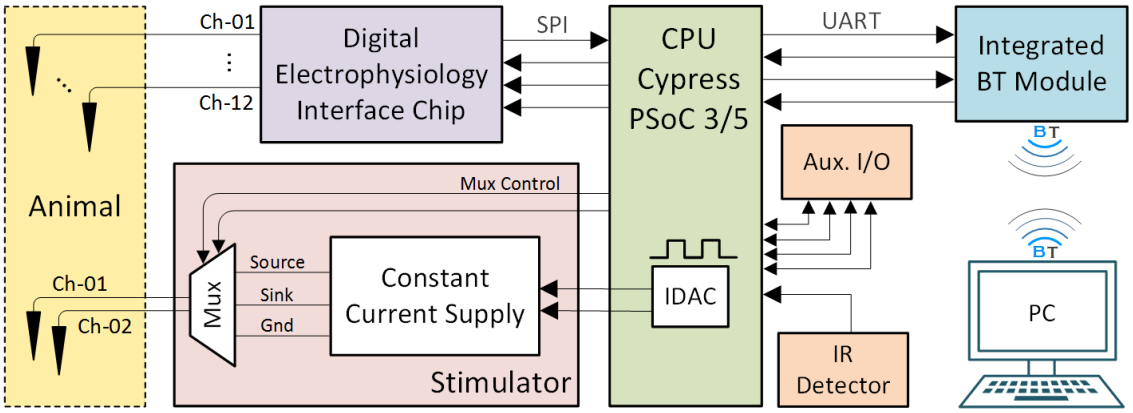

Figure 2. SRD system overview showing interconnections between CPU, Bluetooth (BT) module, host PC, stimulator, multiplexor (mux), digital electrophysiology interface chip, auxiliary input/output, infrared (IR) detector, and electrodes within animal tissue. A serial peripheral interface (SPI) and universal asynchronous receiver/transmitter (UART) interface are used for digital communication between the CPU and electrophysiology interface chip and between the CPU and BT module respectively.

The SRD's specifications are highlighted in Table 1 and includes specifications related to the system as a whole, such as enclosure and printed circuit board (PCB) size, and specifications related to only the recorder, stimulator, and power. Each of these specifications are discussed in more detail in section 2.4.

Table 1. Overview of SRD specifications.

Subsystem	Parameter	Specification
Whole System	Size (enclosure)	53.5 x 33.5 x 16.9 mm
	Size (PCB)	48.0 x 27.0 mm
	Weight	39 g (includes battery, PCB, and enclosure) Enclosure: 14.8g PCB: 7.1g Battery: 17.1 g EIB: 0.2 g Connector/wire: 0.7g
	Battery Life	37 hr. (during standard experimental operation)
Recorder	Sample Rate	1 - 15 ksps/channel
	Resolution	16 bit
	Channels	1 - 2 (12 available)
	Filter Bandwidths	0.1 - 500hz (high pass filter cut off) 100 - 20k Hz (low pass filter cut off) < 1 - 1655 Hz (digital high pass filter cut off)
	Noise Floor	± 5 µV (inputs grounded)
Stimulator	Waveform shapes	biphasic, monophasic, pseudophasic
	Phase Duration	0.5 - 5.0 ms
	Inter-Phase Interval	0.1 - 5.0 ms
	Frequency	0.2 - 5.0 Hz
	Amplitude	± 255 µA (1 µA increments)
	Stim Compliance Voltage	± 10 V
Power	Voltage Input	3.7 - 5.1 Volts
	Average Current	≈ 27 mA

2.2 System Cost

One of the key design requirements for the SRD was to keep the cost relatively low and therefore accessible to more users. Other than the integrated electrophysiology interface chip, the system components are relatively low cost. Totaling the SRD circuit components, backpack, wearable vest, and circuit board manufacturing services yields a cost of less than $500. A system cost breakdown grouped by PCB components, backpack components, and per experiment consumables are listed in Table 2.

Table 2. Summary of SRD cost by component category.

Category	**Component/Service**	**Cost**
Primary SRD PCB	RHD2216	$ 260
	PSOC3	$ 15
	RN42 BT Module	$ 15
	Power Supply	$ 10
	Stimulator	$ 10
	Misc. Supplies	$ 50
	PCB	$ 12
	Battery	$ 10
	Sub-Total:	$ 382
Backpack	Vest	$ 15
	Enclosure (3D print)	$ 30
	Sub-Total:	$ 45
	Device Total:	**$ 427**
Consumables	EIB (Custom or Commercial)	$ 30-90
	Electrodes (2x)	$ 30 each
	Total:	$ 90-150

2.3 Open-Source Availability

Design files for the circuit schematic, circuit PCB, SRD enclosure, SRD firmware, SRD GUI, and external sync device PCB will be made available to the public

at http://github.com/jramshur. If enough interest builds, a dedicated project will be created for the SRD on GitHub. GitHub allows other users to "fork" their own copies of the repositories. Users can then make changes and improvements as they see fit, and submit those improvements back to be incorporated into the original design if approved by an administrator. Hopefully, using this type of availability, a user community will develop and the SRD system will be improved by the users.

2.4 Hardware Design

Power Supply Subsystem

Power to the SRD is derived from a rechargeable single-cell lithium polymer (LiPo) battery or any voltage input from 3.5 - 5.1 V via a micro-USB jack. A micro-USB connector provides a low profile and more universal alternative to the standard 2-pin JST connectors typically used with LiPo's. A micro-USB jack also allows PC USB ports or any USB power supply, within the operating voltage range, to be used in place of the LiPo battery. However, care must be taken when using non-battery power sources such as PC USB ports and switch-mode USB power supplies because these supplies can be noisy and could introduce unwanted noise into the system. The LiPo battery used in this study was an 850 mAh LiPo battery from Sparkfun Electronics. Protection circuitry comes attached to the LiPo battery to prevent damaging discharge or recharge.

The SRD uses four separate power domains to supply power to analog, digital, negative stimulation, and positive stimulation circuitry. See Figure 3 for a power supply schematic. The digital and analog power domains each use a separate 3.3 V rail and are generated using one dual low-dropout (LDO) linear regulator (Micrel MIC5393).

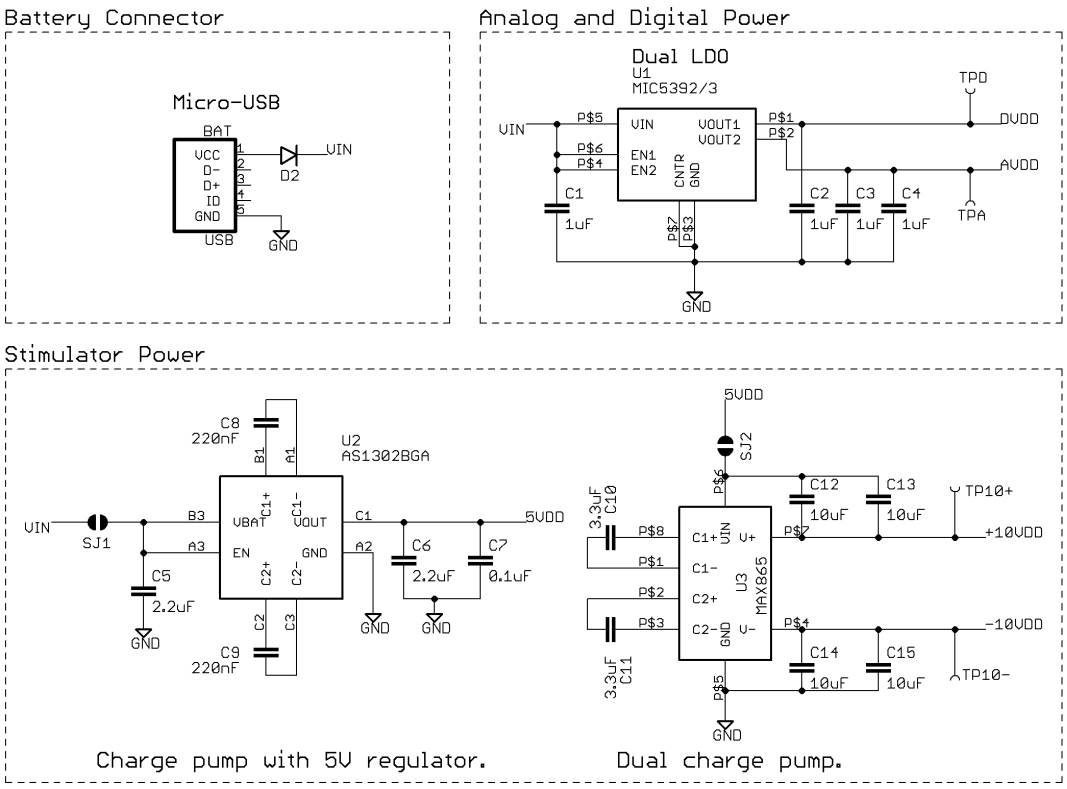

Figure 3. Schematic of the SRD's power system. Top left is a micro-USB battery connector. Top right is the dual linear regulator that generates 3.3 V for analog (AVDD) and digital (DVDD) components. The bottom components are power supplies that generate posative 10 V (+10VDD) and negative 10 V(-10VDD) used for stimulation components.

The MIC5393 integrates two high-performance 150 mA LDO's into a tiny 6-pin, 1.2 x 1.2 mm leadless dual-flat no-leads (DFN) package with more than 60 dB power supply ripple rejection. Drop out voltage is less than 155 mV at 150 mA which allows the SRD to operate until the battery drains to near 3.45 V.

Stimulator power is generated in two stages. The first stage boost the LiPo battery voltage up to 5 V using an AMS AS1302 30mA inductor-less boost converter that integrates both a double H-Bridge charge-pump and a 5V regulator for stable 5 V output. The AS1302 is packaged in an extremely small 1.2 x 1.2 mm 8-bump ball grid array (BGA). The second stage converts 5 V from stage one into both a -10 V (-10VDD) and +10 V (+10VDD) rail used for the generation of stimulation currents. Stage two uses a Maxim MAX865 dual-output charge pump in a 3 x 4.8 mm micromax small-outline package.

Core Processor Subsystem

The core processor chosen for the SRD is the Cypress Semiconductor's PSoC 3 programmable system-on-chip with 8051 microprocessor core. The PSoC family of chips are embedded design platforms that integrate configurable analog and programmable logic along with memory and a microcontroller on a single chip. PSoC allows the designer the ability to build a custom mixed-signal system-on-chip and to reconfigure the design and reroute signals by simply reprogramming via software. Many pre-built digital components are available such as universal asynchronous receiver/transmitter (UART) and SPI, but users also have the ability to build custom digital components using digital blocks with Verilog or state machine diagrams.

Within the SRD the PSoC 3 manages all aspects of the device including timing, analog sampling, stimulus control, auxiliary input/output, external IR sensing, and wireless communications. The PSoC chip version chosen was the CY8C3866, and the package chosen was an 8 mm x 8 mm 68-pin quad-flat no lead (QFN) package. If future applications require increased memory or processing speed the selected PSoC 3 can be exchanged for a PSoC 5 or PSoC 5LP chip without requiring PCB layout changes. Figure 4 shows a schematic of the PSoC along with some additional features of the SRD associated with the PSoC. Some of these features are a low-profile zero-insertion force (ZIF) socket to allow reprogramming of the PSoC, a second ZIF header for auxiliary analog or digital input/output, a reset button for system wide reset, a three color RGB (red-green-blue) LED for status indications, and a IR sensor circuit for external triggering which will be discussed in 0. The auxiliary header includes two pins dedicated for digital (AUX_D1 and AUX_D2), pins for DVDD and GND, and two pins dedicated for analog (AUX_A1 and AUX_A2) on a semi-isolated and decoupled range of pins for improved noise immunity. However, given the nature of the PSoC environment all four auxiliary pins can be configured for either digital or analog and as inputs or outputs. A 1.6 x 1.6 mm RGB LED (Kingbright APTF1616SEJ3ZGGVBDC) was used to give SRD status feedback to the user.

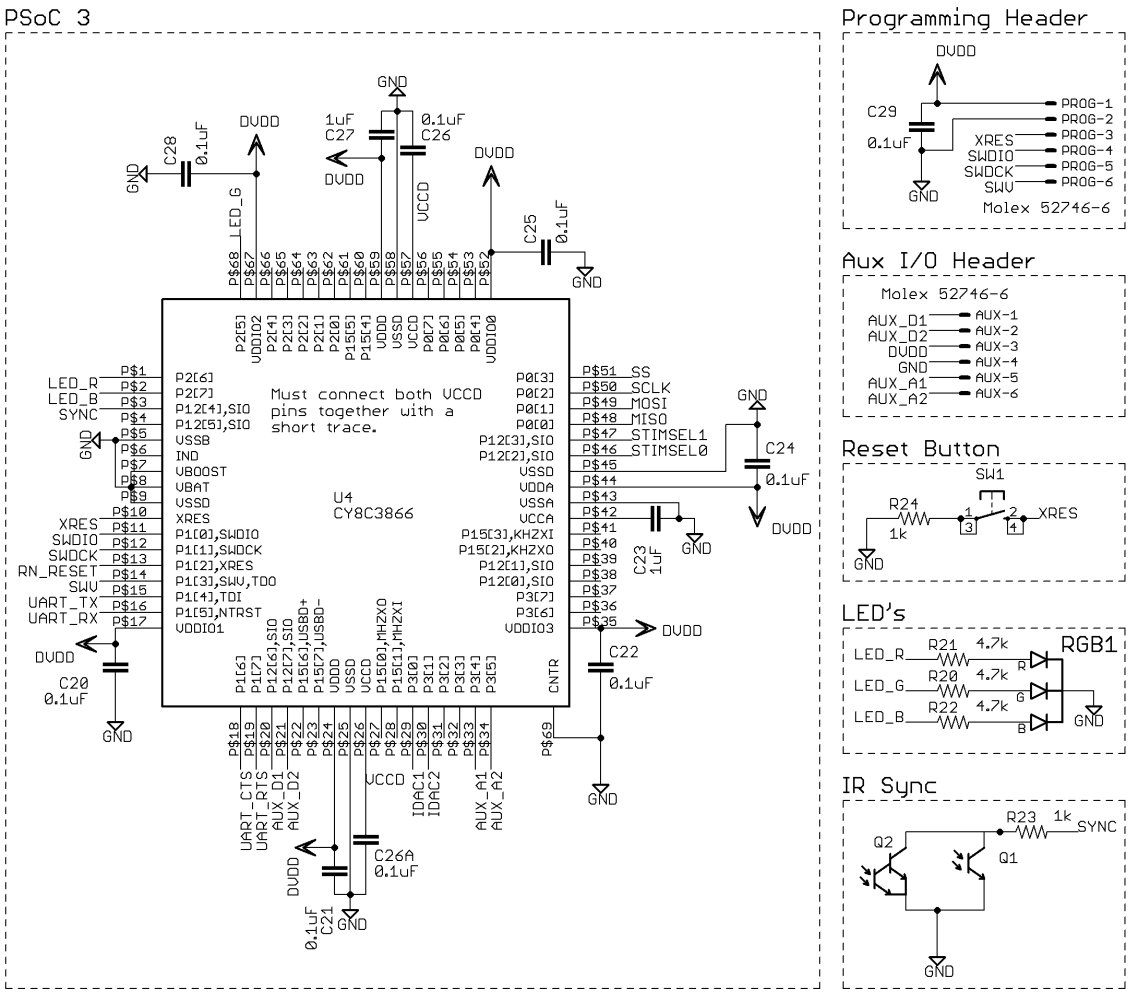

Figure 4. Schematic of core processing subsystem with PSoC and related features including programming header, auxiliary analog or digital input/output header, system reset button, three-color LED, and IR sync circuit.

Recording Subsystem

Analog biological signals are digitized using an Intan Technologies RHD2216 digital electrophysiology interface chip. Key features of the RHD2000 series include: programmable analog and digital filters, 16-bit analog-to-digital converter (ADC), 30 ksps/channel sample rate, bipolar or unipolar configurations, in-situ electrode impedance measurement capability, and 16-bit SPI communication. The RHD2216 is packaged in 8 × 8 mm QFN package and requires no external components other than two small decoupling capacitors and one optional decoupling capacitor. Figure 5 illustrates a simplified internal diagram of the RHD2216 chip.

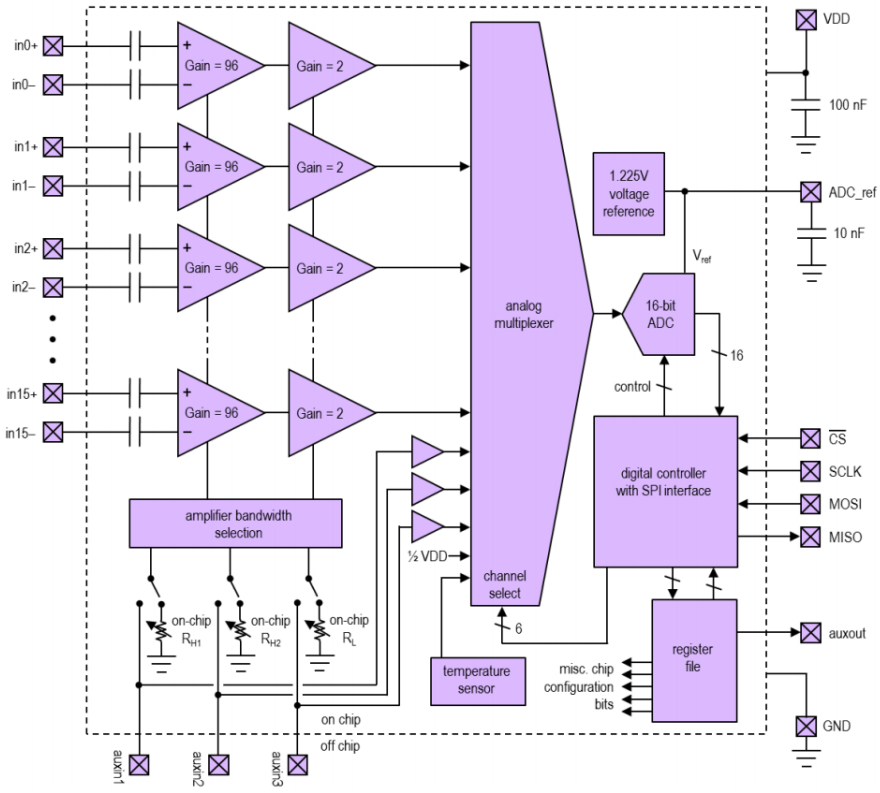

Figure 5. RHD2216 simplified internal diagram. Schematic from Intan RHD2000 series datasheet [173].

The SRD was configured for 12 unipolar recording channels with a maximum sample rate of 15 ksps/channel. Users have the ability to select any two channels from the 12 available channels, or have the SRD sweep through all channels two at a time. Sample rate, filter settings, and channel selection are adjustable using the GUI. A small 18-pin keyed Omnetics A79043 Neuro connector was used as the analog input/output header for cortical signals from electrodes and stimulation waveforms to the cortex. A schematic of how the Intan chip was wired on the SRD is shown in Figure 6.

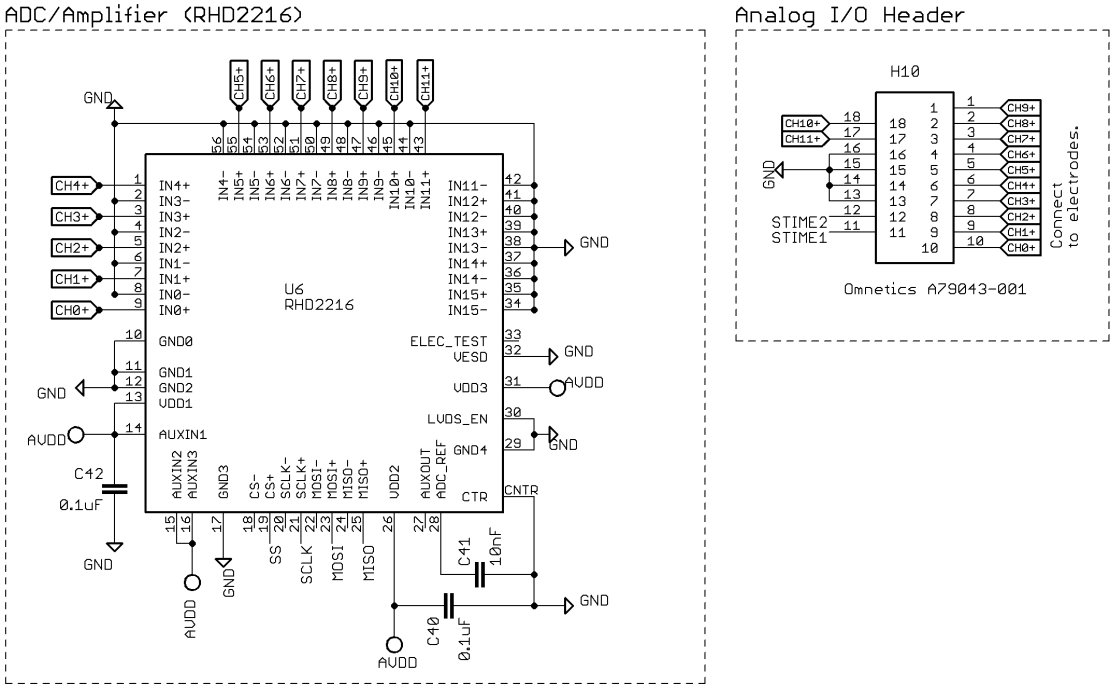

Figure 6. Schematic of the recording subsystem and analog I/O header.

The upper and lower bandwidths of the amplifiers can be dynamically programmed by means of internal registers on each chip. This flexibility allows the chips to be optimized for many different types of electrophysiological signals including electrocardiogram (ECG), electromyogram (EMG), electrocorticogram (ECoG),

electroencephalogram (EEG), neural spikes, and local field potentials. A 3rd order Butterworth low-pass filter defines the upper cutoff frequency of each amplifier and are set by on-chip registers. Upper bandwidth cutoff frequencies (f_H) are adjustable from 100 Hz to 20 kHz. Lower bandwidth frequencies are defined by a 1sr high-pass filter for each amplifier and are also set by on-chip registers. Lower bandwidth cutoff frequencies (f_L) are adjustable from 0.1 Hz to 500 Hz.

An optional digital offset removal feature can be enabled within the GUI to implement IIR based single-pole high-pass filters on each sampled amplifier channel similar to those of an analog high-pass filter implemented with a capacitor and resistor. The optional digital filter can be used to remove the residual DC offset voltages associated with the analog amplifiers. Enabling the digital filter adds an additional pole of high-pass filtering to the single-pole inherent in the analog amplifier circuits.

Some considerations noted in the datasheet need to be observed when using the digital high-pass filter. Since the DSP filter has perfect linearity while the analog amplifier circuits have imperfect linearity, it is good practice to set the digital cutoff frequency (f_C) higher than the analog amplifier lower cutoff frequency (f_L) to minimize the distortion of large signals. If a large signal is applied to an amplifier channel with the digital high-pass filter enabled, the sampled output will "hard limit" at the numerical minimum or maximum permitted by the 16 bit representation; it will not "roll over" due to numerical overflow or underflow. Also, the cutoff frequency of the digital high-pass filter is determined by the sampling rate and a variable k_{freq} with values stored within the RHD2000. For the SRD user, the sampling rate is considered and k_{freq} values are automatically computed within the GUI. The user simply selects the sampling rate and

chooses from a drop-down menu of available digital cutoff frequencies available for that sampling rate.

Stimulator Subsystem

A constant current stimulation circuit allows delivery of monophasic, biphasic, or pseudophasic current pulses of up to ±255 µA to the biological tissue. Current pulses can be directed to one of two monopolar electrodes. Several stimulation circuits were proposed and tested, but it was decided to take advantage of the PSoC's on-board current-mode digital-to-analog converters (iDAC) due to their ease of use and internalized components that reduce PCB size. These iDAC's have 3 output ranges (2,040 µA, 255 µA, and 31.875 µA) and two polarities (sink or source). For this application the 255 µA range was selected which gives 1 µA increments. PSoC iDAC's current output values are set by an 8-bit register or one command in the PSoC firmware.

However, to produce a current of desired specifications iDAC outputs need to be conditioned. This is accomplished by using a three stage process as illustrated in Figure 7. The first stage uses two built-in PSoC iDAC's to produce one 0-255 µA current source (positive polarity) and one 0-255 µA current sink (negative polarity) each of which have a compliance voltage of around 1 V. Compliance voltage is the voltage required in a circuit to maintain a constant current given by Ohm's Law (V=IR). Specific to the SRD circuit, compliance voltage is defined as the voltage required to maintain constant current across the combined animal and electrode load. An example of stimulation compliance voltage follows: if the SRD needs to deliver 100 µA to the tissue with effective impedance is 100 kΩ the voltage required is at least 10V (voltage = current x resistance).

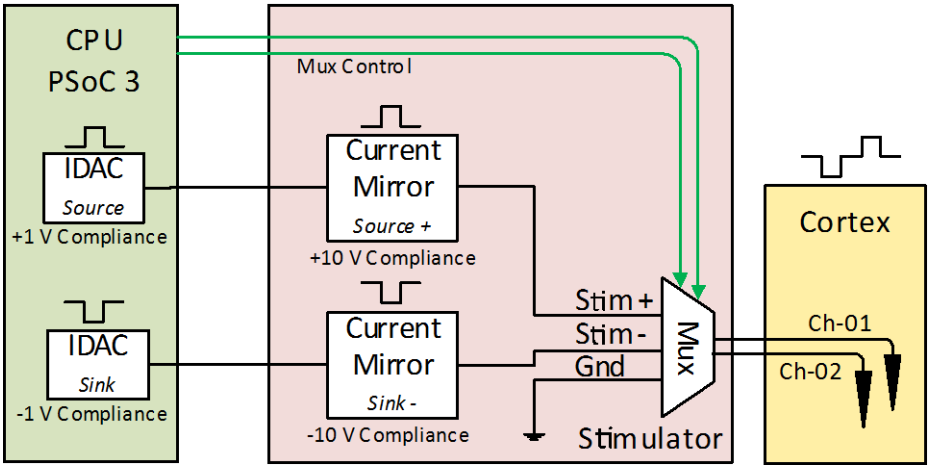

Figure 7. Simplified schematic of the SRD stimulator implementation. The PSoC3 (left) provides stimulator control current by means of two on-chip iDAC's. Control current is then mirrored by two independent current mirrors (center) to increase compliance voltage and directed to a user defined electrode (right) using a multiplexor.

Since the iDAC is only capable of about 1 V of compliance voltage the SRD requires additional circuitry to provide a 10 V compliance voltage. To boost the compliance voltage the SRD uses a second stage that simply mirrors the iDAC outputs. The second stage uses two current mirrors that accept control current on the input side from the iDAC and matches that current on the output side. Each SRD current mirror is constructed using one Advanced Linear Devices, Inc. ALD1105 dual N-channel and dual P-channel matched MOSFET pair as shown in Figure 8. Compliance voltage of the current sink mirror and current source mirror are -10 V and +10 V respectively.

The third and final stage allows the SRD to direct current into one of two available electrodes for tissue stimulation or to short both electrodes to ground for discharging if desired. This analog switching capability was accomplished using the Vishay DG9409 precision low-voltage analog multiplexer (BiCMOS). Some advantages to using the DG9409 include: break-before-make action, low on-resistance (3.9 Ω), fast switching times (t_{on}: 4.2 ns, t_{off} : 24ns), and a simple two wire logic interface. Switching

decisions are controlled by two GPIO pins on the PSoC. With an on-resistance of 3.9 Ω the resulting additional voltage drop across the device during stimulation will be negligible (255 µA x 3.9 Ω ≈ 1 mV). Another advantage given to the SRD by the multiplexer is the ability to choose whether the leading pulse of a biphasic/pseudophasic pulse or a monophasic pulse is cathodic (negative) or anodic (positive).

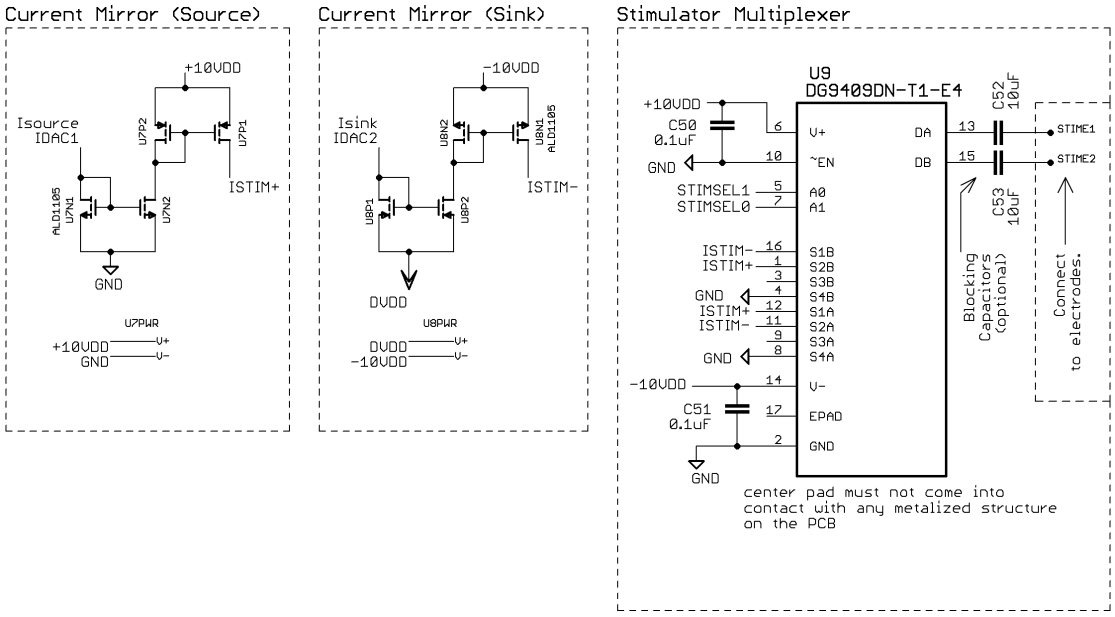

Figure 8. Schematic of stimulator subsystem with current "source" mirror, current "sink" mirror, and stimulator multiplexor.

Wireless Communication Subsystem

The SRD is capable of bidirectional wireless communication using a Microchip RN42 Class 2 Bluetooth 2.1 module with integrated PCB antenna. Although a Bluetooth v2.1 device, the RN42 is backwards compatible with v2.0, 1.2, and 1.1. The RN42 has embedded BT stack profiles GAP, SDP, RFCOMM and L2CAP protocols with SPP and DUN profile support requiring no host processor. Auto-discovery and pairing capabilities allows a pair of RN42's to be used with no software configuration thus acting as an

instant cable replacement. The RN42 settings and power modes can however be configured using simple text based commands via local UART communication or remotely using an established BT connection. Sustained SPP data rates are 240 kbps for slave mode and 300 kbps for master mode. The RN42 is available in a postage stamp sized surface mount package with dimensions of 13.4 x 25.8 x 2 mm and with operating voltages of 3.0 – 3.6 V. Typical operating current consumption for the RN42 are 26 µA in sleep mode, 3 mA when connected, and 30mA during transmutation, but transmission power can be reduced with a modified configuration discussed later.

The wireless subsystem of the SRD uses the RN42 operating at 3.3 V. A schematic of the wireless subsystem is shown in Figure 9. UART settings used by the SRD include 115,200 bps baud rate, 8 data bits, no parity, 1 stop bit, and no flow control. Both incoming setup commands and outgoing data are transferred via the SRD's Bluetooth connection. A red BT status LED on the SRD provides a visual indication of the module's operating mode or state. These modes (Table 3) include command mode, configurable mode, discoverable/idle mode, and connected mode; see the RN42 datasheet for specific descriptions of these modes. Additional features included in the SRD includes a RN42 factor reset jumper on port PIO4 and a pull-up resistor on PIO3 that causes the RN42 to default to a slave auto-discovery mode for establishing easier connections. Shorting PIO4 high three times immediately after reboot causes the RN42 settings to reset to factor defaults. Additionally there is a cut-able jumper on the SRD PCB to allow hardware flow control if needed.

Table 3. SRD wireless mode indicator LED.

BT Status LED	Mode
Fast blink, 10x/second	Command mode
Blinks 2x/second	Boot up, remotely configurable
Blinks 1x/second	Discoverable/idle
Solid on	Connected

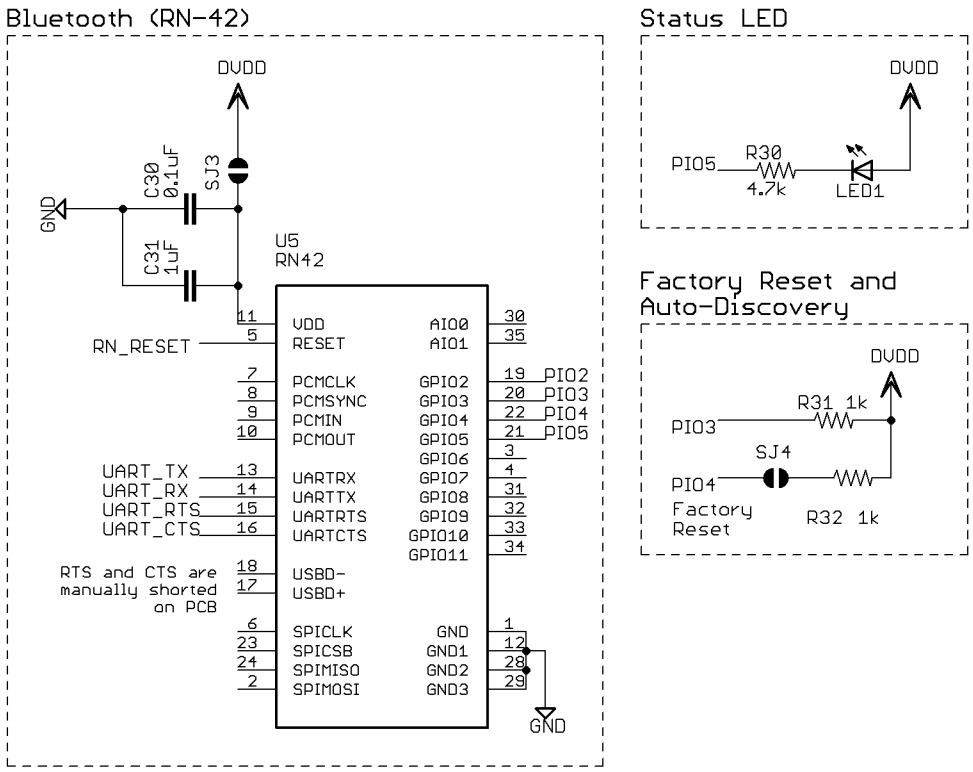

Figure 9. Schematic of wireless subsystem. Left block contains the RN42 BT module with solderable and two bypass capacitors. The two blocks on the left show the status LED, factory reset, and auto discovery configuration.

PCB

The SRD's PCB was designed with Eagle CAD v6 (CadSoft) and constructed using a 1.6mm 4-layer PCB with FR-4 material manufactured at Pentalogix (Lake Oswego, OR). Original prototypes PCB's were manufactured at Oshpark (Portland, OR). Final dimensions of the PCB were 27 x 48 mm. PCB dimensions could be reduced, but we decided to make the PCB only slightly smaller than the LiPo battery used in effort to save design time. 3D models of each PCB version were created to visualize the layout for problems and to be used later for creating a custom fit 3D printed enclosure. PCB 3D models were created by first exporting data from Eagle CAD using the EagleUp script (by Jerome Lamy). 3D models for each PCB component were downloaded or manually created using Google SketchUp. PCB data and component models where then imported into Google SketchUp using the EagleUp import plugin (by Jerome Lamy) to build the complete PCB model. Orthographic projections of the top and bottom sides of the PCB are shown in Figure 10.

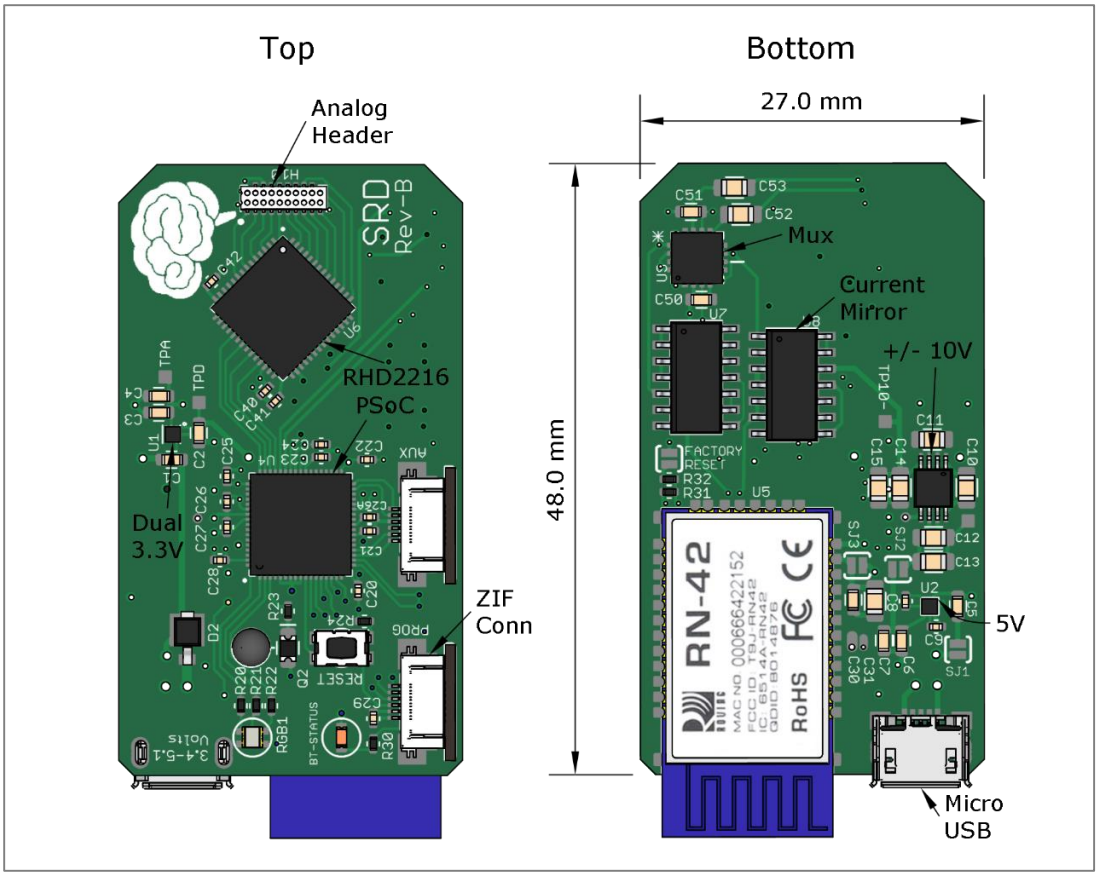

Figure 10. SRD PCB component layout of top and bottom sides. Dimensions of the SRD PCB were 27 x 48 mm.

Signal and power connections were routed according to established standards in efforts to minimize noise. Top and bottom copper layers contain signal layers with no copper fill while the second copper layer primarily contains a ground plane, and the third copper layer primarily contains a digital and analog power plane. Bluetooth module, stimulator power supplies and stimulator circuits are located on the bottom layer (Figure 10) in efforts to keep the potentially noisier elements away from the more sensitive analog components on top. The top layer is separated into a region for analog routing around the RHD2216 and a region for digital routing around the PSoC. All electrophysiology signals are routed to/from the electrophysiology interface chip via a

small analog header (Omnetics A7518-801 male connector) located near the edge of the PCB. Analog signal trace lengths were kept as short as possible between chip and header to minimize noise. The digital partition of the top layer contains all LED's, programming connector, auxiliary connector, reset button, and PSoC 3 chip. The analog and digital dual LDO regulator was placed between the two partitions so that the distance from both 3.3 V output pins travels a minimum distance to its respective power plane.

Enclosure

In order to protect the SRD components from damage during experiments and to create a unified housing for both battery and PCB, an enclosure was design and fabricated. The enclosure was designed around the PCB and battery to make it as small as possible. A 3D model of the enclosure was designed using Google SketchUp. The enclosure fits tightly around the PCB with 1 mm or less clearance. Design elements of the enclosure as shown in Figure 11 include: a compartment for easily removing batteries, access to the micro-USB power connector, light pipes to transfer light from status LEDs, hole to expose the IR sensor, access hole for the reset button, cutout for the analog header, cutout for BT antenna, and dimensions of 16.9 x 16.9 x 33.5 x 53.5 mm (H x W x L). The enclosure lid is held onto the primary enclosure body by four pair of 2x 2 mm cylindrical neodymium magnets. Figure 12 depicts an exploded view of how SRD PCB, battery, and enclosure fit together.

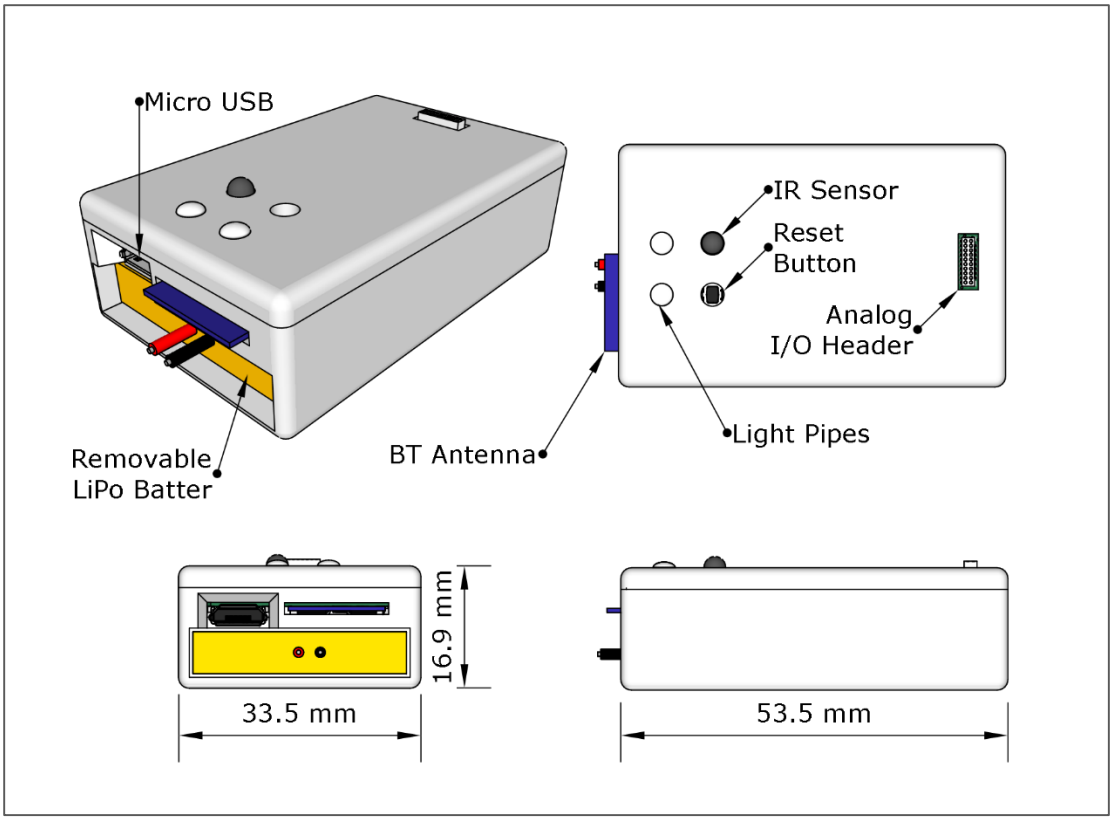

Figure 11. 3D model of SRD enclosure with several key features highlighted including the exposed micro USB connector, removable battery, exposed BT antenna, light pipes, IR sensor, recessed reset button, and analog header. Dimension of the SRD enclosure are 16.9 x 33.5 x 53.5 mm.

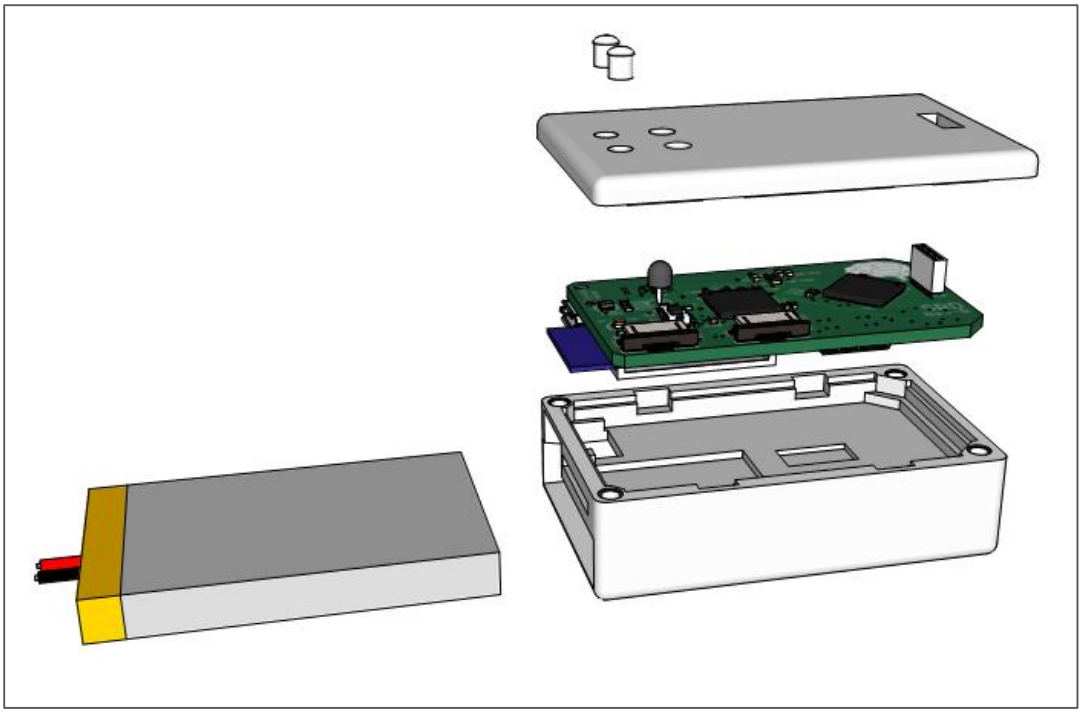

Figure 12. Exploded view of SRD enclosure 3D model with battery (left), PCB (middle) and enclosure top and bottom.

Backpack and Headstage

In order to stimulate and record in an awake animal for extended periods of time, the SRD must be worn by the rat and a headstage must be affixed to the animal. A headstage includes chronically implanted electrodes coupled to an exposed connector all of which is bonded to the animal's skull. For creating a wearable SRD the SRD enclosure was fixed via Velcro to a stretchable rodent jacket by Lomir Biomedical Inc. as depicted in Figure 13.

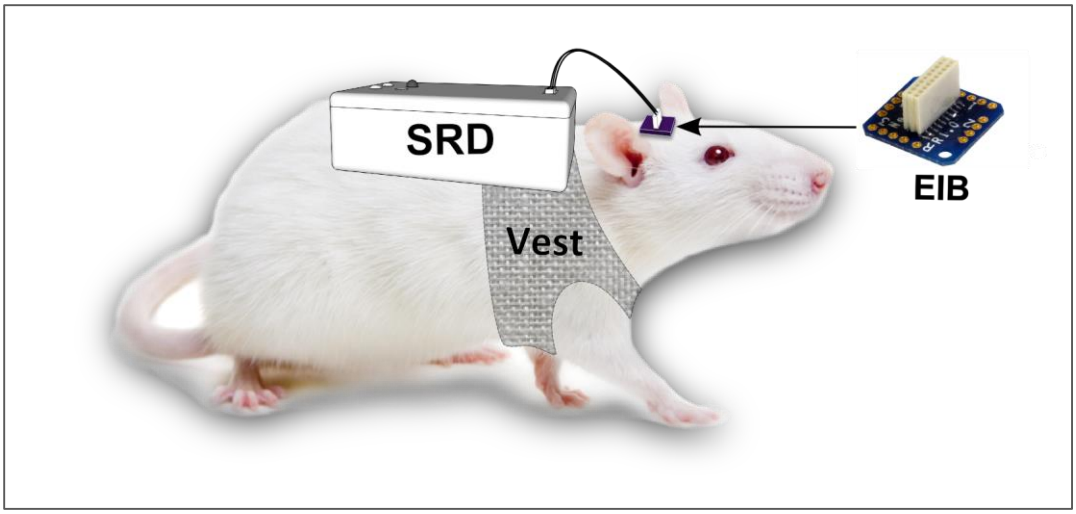

Figure 13. Illustration of SRD system on animal including vest, SRD with enclosure, wire interconnect, and electrode interface board (EIB).

The headstage consist of a chronically implanted stimulating electrode, implanted recording electrode, and a 1 x 1 cm electrode interface board (EIB) attached to the rat's skull as illustrated in Figure 14. Two types of EIB's were used with the SRD. One EIB option was a commercially available EIB (model: EIB-16) by Neuralynx, Inc. (Boxeman, MT). The second EIB used was an in-house reproduction of the Neuralynx EIB-16 made by using a custom printed PCB from Oshpark and an Omnetics (Minneapolis, MN) A7518-801 male connector. This is the same connector used as the SRD analog header. Figure 15 shows the schematic, PCB top, PCB bottom, and 3D model of the custom EIB.

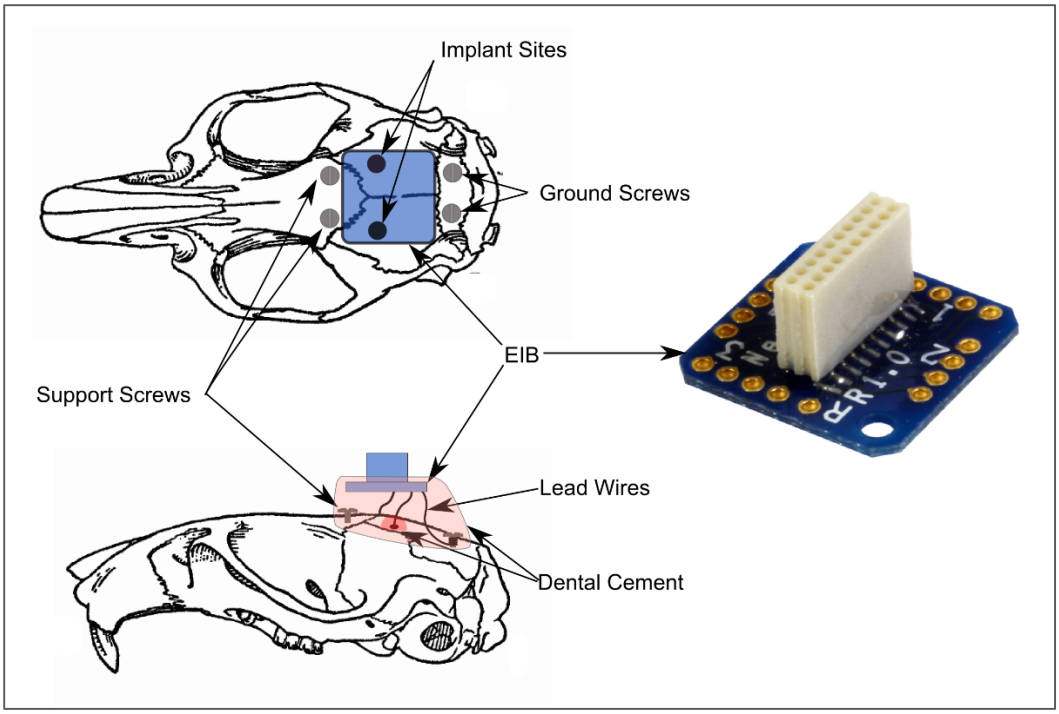

Figure 14. Illustration of SRD headstage with EIB, approximate locations of implant sites, screws, lead wires, and encapsulating dental cement.

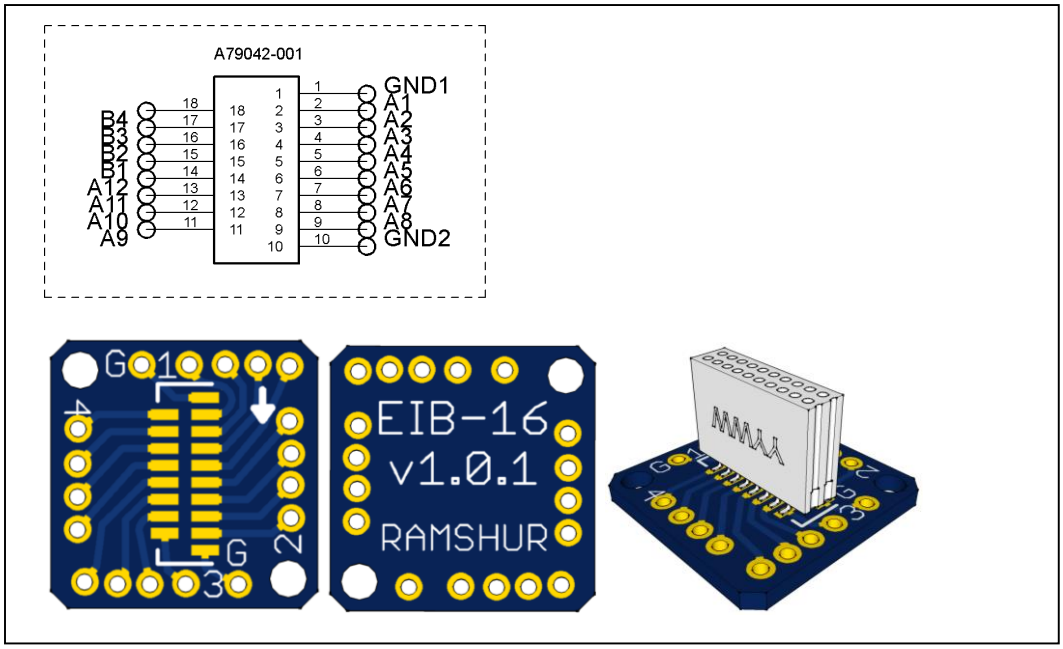

Figure 15. Electrode interface board schematic and PCB. Top row shows schematic of EIB. Shown on bottom row from left to right are the EIB top, EIB bottom, and 3D rendering of EIB with connector attached.

A description of electrode implantation is presented in the appendices (Appendix E: Pictorial Sequence of Electrode Implantation). Electrode lead wires were secured to the EIB using gold plated friction pins, size large from Neuralynx. Figure 14 illustrates how the EIB was positioned relative to the skull. A stainless steel screw was used as a low impedance ground electrode, and additional anchoring screws were placed into the skull surrounding the implanted electrodes to provide anchors for an encapsulating layer of dental cement. Encapsulation bonds the EIB onto the rat's skull and covers all lead wires and exposed bone screws. Finally, the headstage and SRD were connected via a detachable and flexible wire interconnect constructed using 18 34-gauge stranded and insulated wires and two Omnetics A9847-801 female connectors.

External IR Trigger

Some applications require the user to sync the SRD recording or stimulation with an external system. For example, we use an external device to deliver peripheral stimulation while simultaneously recording evoked responses. Both tethered and non-tethered solutions were examined, but to adhere to the overall wireless nature of the SRD a wireless, IR based solution was chosen. The SRD includes an onboard IR sensing circuit capable of triggering a SRD recording or stimulation event. The IR pulse sensor is an IR sensitive phototransistor (Osram MTD8000M3B) connected to a PSoC SIO pin configured as a digital input using the resistive pull-up mode as shown in lower right schematic of Figure 16.

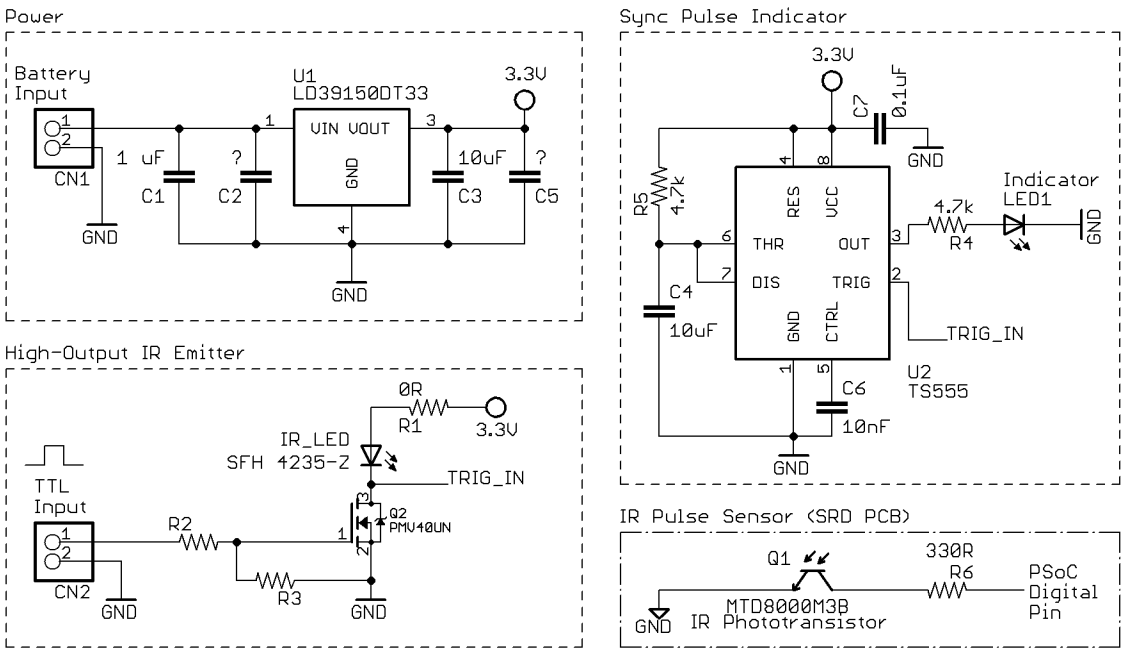

Figure 16. Schematic of IR sync pulse emitter showing its power supply, input/output, and pulse indicator circuits. All schematic sections physically reside on the IR emitter PCB except for the section in the lower right indicated by "SRD PCB". This section resides on the SRD PCB.

A separate PCB was designed and manufactured (Oshpark) that allows 3 - 5 V pulses from external devices to generate IR sync pulses, as input to the SRD's IR pulse detector. A schematic of the IR pulse circuit is also shown in Figure 16. Power for the IR pulse emitter board is provided using a single cell LiPo battery or three standard AA batteries and 3.3 V LDO linear regulator (LD3915). Incoming 3 - 5 V square wave pulses causes an N-channel enhanced mode MOSFET (PMV40UN) to allow current flow through a high intensity IR emitter (Osram SFH 4235). Subsequent emitted IR light pulses are of the same duration as the original input pulse. IR pulses should be kept to under 10ms as to not damage to IR emitter. For convenience, an additional standard LED is used to give a visible confirmation of IR pulses. Given that the input pulse durations may be too short to produce a visible LED pulse, a monostable TS555 circuit was used

(Figure 16) to create a visible light pulse with duration independent of the input or IR pulse duration. The TS555 is a CMOS version of the standard 555 timer IC, but offers significantly lower operating current and offers operating voltages lower than the typical 5 V requirement such as our 3.3 V supply. Figure 17 shows a photograph of the IR sync device PCB housed inside a clear-top water resistant enclosure. The enclosure has an on/off toggle switch to disable PCB power and a BNC input signal connector. Both the IR emitter LED and the standard indicator LED are projecting through the clear top. Shown at the bottom of the photograph is the custom shape PCB without components.

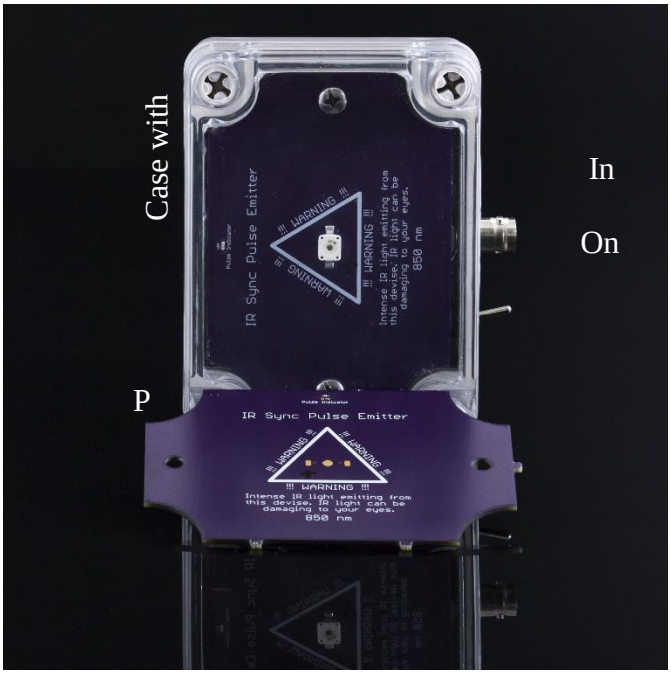

Figure 17. Photograph of IR transmitter PCB inside its clear top enclosure (top) and of the PCB alone (bottom). To the right of the enclosure is a BNC connector for 3 - 5 V square wave inputs and an on/off toggle switch for power.

The scenario of how the IR sync device would typically be used in this projects experiments is illustrated in Figure 18. This scenario depicts the SRD being used to record cortical signals while an external system provide stimulation to the animal

forepaw. The external system and IR sync device are connected via a cable that transmits a 3 - 5 V square wave pulse to the IR device. Effectively the external system is triggering the SRD to record at a specific time relative to the stimulus event. Although this scenario depicts the use of an external stimulation system, the SRD and IR sync device could also be used to record from an external system and stimulate cortex using the SRD.

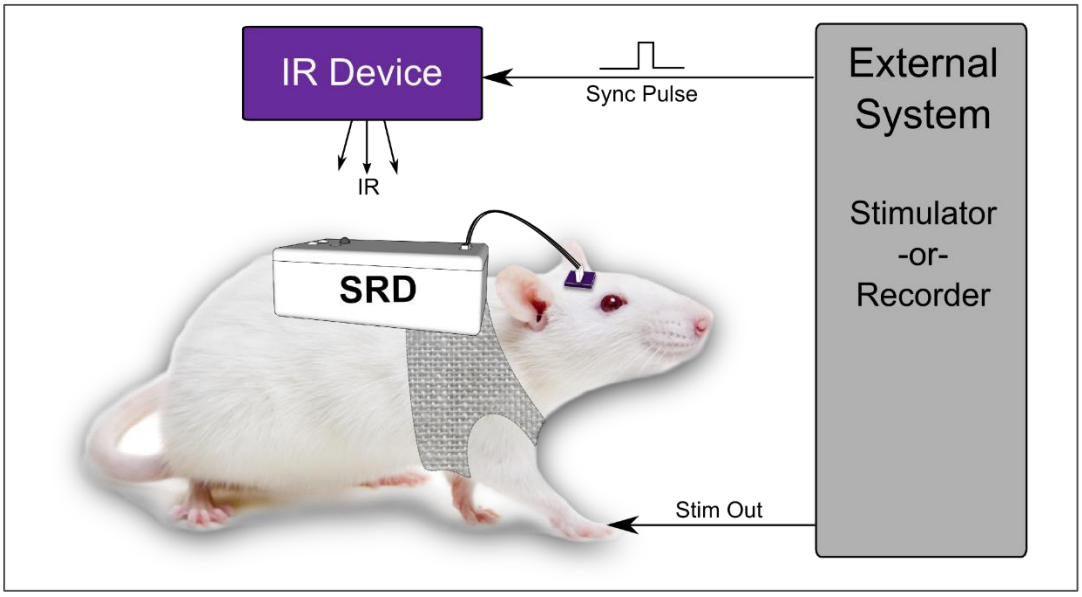

Figure 18. Example use scenario of the external IR sync device being used to synchronize SRD recording with external forepaw stimulation provided by an external stimulation system.

Caution must be observed when using the IR emitter device because the IR emitter chosen emits highly concentrated non-visible infrared light which can be hazardous to the human eye. Keeping the pulse duration short as possible and the direction of emission away from direct viewing should minimize any retinal exposure to the subject or to the human user. The SRD should be capable of detecting IR pulses less than 1 ms based on results shown in Section 0.

2.5 Software Design

This section will briefly discuss software designed for the SRD system including the application firmware and the GUI. In-depth details of the software will be included in instruction manuals and within code comments found on the projects GitHub pages.

Firmware

The first type of software operates within the SRD's hardware or more specifically within the PSoC CPU. This type of software is often referred to as application firmware. SRD's firmware handles all hardware control and processing that takes place on the SRD PCB. Firmware for the SRD was designed using Cypress Semiconductor's PSoC Creator 3.0. PSoC Creator is a free Windows-based integrated development environment (IDE) which allows concurrent hardware and application firmware design of the PSoC. All firmware code was written using C source code and compiled using the PSoC Creator's integrated compiler.

GUI

The second type of software used with the SRD is the GUI. The GUI allows users to interact with the SRD via a PC. All of the SRD's stimulation and recording settings are configurable using the GUI along with an ability to view and save live signals streaming from the SRD. Here we will only discuss some of the key design features of the GUI and not details of the underlying source code.

Six SRD operating modes are available from the GUI and shown in Figure19(A). These modes include Off, Automatic, Continuous, External Stimulation, External Recording, and Look-Ahead External. Off mode simply places the SRD in a quiescent

mode whereby no stimulation, recording, or wireless outbound data transmissions are occurring. Several of the PSoC components are also switched to a low power operating state to conserve energy. Automatic mode is an "autonomous" mode that stimulates and records on a user programmed schedule. All signals are buffered on-chip and then sent to the PC. Once set, the SRD runs in a loop until manually stopped by the user. The user can set an active (T1) and sleep period (T2) where the SRD is either actively stimulating/recording or sleeping until the next period of activity. These timing parameters are discussed in the Timing Settings section below. Continuous mode samples signals from the amplifiers and immediately sends signal data to the PC for viewing in a streaming fashion. This mode is limited to a single channel. External Stimulation mode is used to trigger the SRD's stimulation function using an external source. By default, the on-board IR sensor is used as the trigger input source, but any of the auxiliary inputs could be programmed for trigger inputs within the firmware. Once an IR pulse is detected the SRD stimulates the tissue with a single stimulation event according to the stimulation settings defined in the GUI. Stimulation frequency and delay are irrelevant for this mode. Similarly, External Recording mode is used to trigger the SRD to record a single trace via an external source. Again, the default trigger input source is the on-board IR sensor. Finally, the Look-Ahead External mode continually buffers signals from the amplifiers and only sends signal data to the PC when an external trigger is detected. The buffering feature allows the SRD to capture pre-event and post-event signals without the need to know when the external trigger/event will occur. This mode could be useful in behavioral experiments where the animal triggers the external event.

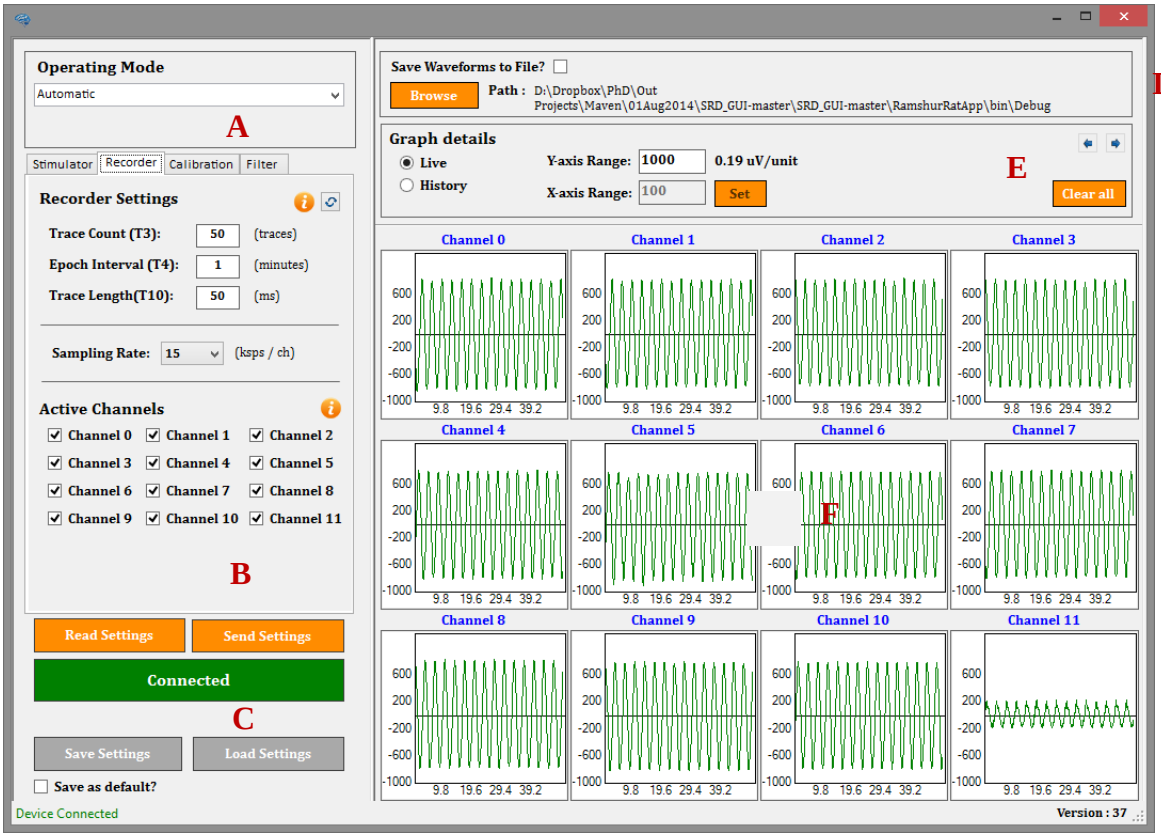

Figure 19. Screenshot of the graphical user interface (GUI) with highlighted sections of controls and live streaming of a sine wave to all SRD inputs for reference. These sections are (A) operating modes, (B) stimulator, recorder, calibration, and filter settings tabs, (C) buttons for connecting to the SRD, sending/receiving settings to/from SRD, and saving/loading settings from a file saved to the PC, (D) options for saving waveforms to file, (E) options for viewing live or previous waveform files, and (F) graphs of all 12 available channels with sinusoidal waveforms inputs shown for demonstration purposes.

SRD settings for stimulation, recording, calibration, and filter bandwidths are separately partitioned into respective tabs on the GUI as shown in Figure 19(B). All four available tabs are shown sequentially in Figure 20. Available settings for stimulation include stimulation amplitudes, durations, inter-phase interval, stimulation interval, and stimulation delay (relative to start of recording). Available settings for recording include the trace count (number of traces captured during each recording epoch used in automatic mode), epoch interval, trace length, sampling rate, and active channels. Available settings for calibration include ADC calibration and stimulation calibration gain and offset (assumes linear calibration). Available settings for the filters include -3 dB cutoff frequencies for F_L, F_H, and digital F_C defined in 0.

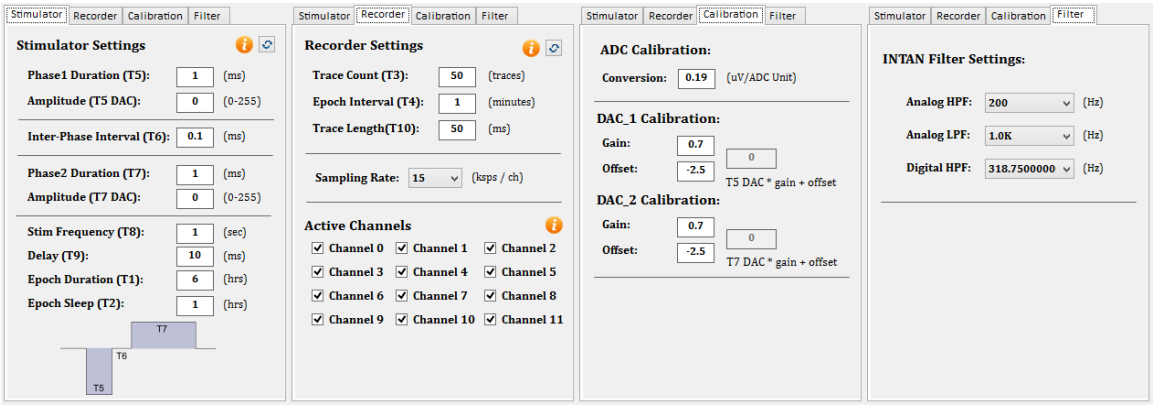

Figure 20. GUI settings tabs. From left to right are stimulator settings, recorder settings, calibration settings, and filter settings.

As mentioned earlier signals/waveforms from the SRD can be viewed and saved in the GUI. The GUI allows the user to save or not save incoming signals (Figure 19(D)) and to define the saved file locations. Axis ranges for x and y axes can be adjusted to zoom in/out of the signal waveforms (Figure 19(E)). However, x-axis can only be adjusted during continuous mode at this time. A radio button defines whether the GUI

will display live signals or review signals from “history” that were previously saved to file. Users can scroll through saved signals contained within a selected file folder. Signal waveforms from each channel are displayed in the corresponding graph labeled from channels 0 to 11 (Figure 19(F)).

Timing Settings

All user definable timing settings available within the GUI are illustrated and described in Figure 21. These settings are available for all operating modes, but some timing settings are only applicable to specific operating modes. Stimulation and recording events are grouped into “epochs” or subdivisions of time. These epochs are only applicable to the automatic operating mode and include timing settings T1-T4. Stimulation epochs are defined by the epoch duration T1 (hours) and the period of inactivity and sleep defined by T2 (hours). Recording or acquisition epochs durations are defined by T3 (# of traces) and have an inter-epoch period defined by T4 (minutes). Acquisition epochs only occur within stimulation epochs as was desired for this project. Our project needs the ability to stimulate cortical tissue for periods of time and periodically recorded corticocortical evoked potentials. Looking at smaller scale timing settings we see timings for individual stimulation and acquisition events. Stimulation event timing include the pulse duration of phase one defined by T5 (ms), inter-phase interval defined by T6 (ms), pulse duration of phase two defined by T7, and the stimulation frequency/period defined by T8 (seconds). Acquisition trace durations are defined by T10 (ms) and the delay between start of data acquisition and start of stimulation is defined by T9 (ms).

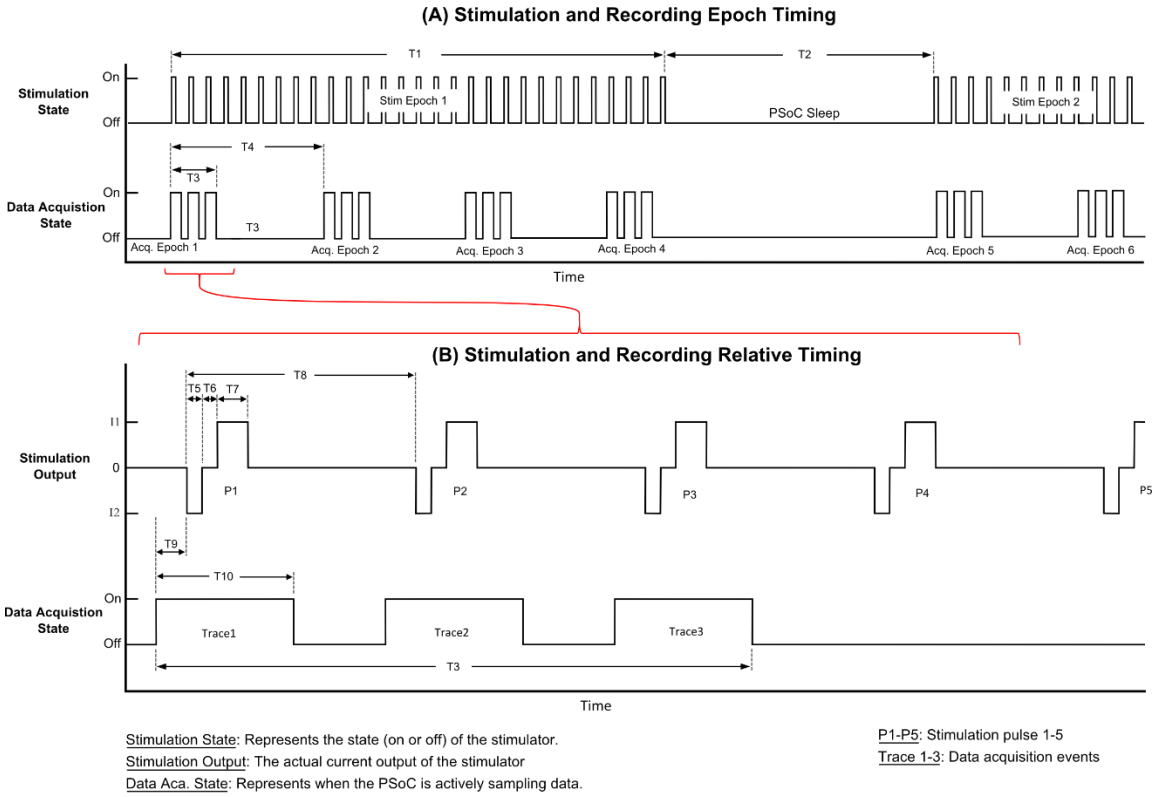

(C) Event Timing Descriptions

Timing Number (see above)	Description	Scale
T1	Total duration of stimulation epoch	1-6 hrs
T2	Time between stimulation epochs	1-15 hrs
T3	Total duration of data acquistion epoch -or- number of traces	1-50 traces
T4	Time between data acquistion epochs	
T5	Duration of stimulation - phase 1	0.5-5 ms
T6	Duration between stimulation phase 1 and phase 2	0-5 ms
T7	Duration of stimulation - phase 2	0-5 ms
T8	Time between stimulation events	0.1-5 sec
T9	Time delay between start of data acquistion and onset of stimulation	0-10 ms
T10	Duration of single data acquistion event (trace length)	50-500 ms

Figure 21. SRD experiment timing parameters. Each timing parameter T1 – T10 is shown visually (A and B) and described (C). Timing parameters T1-T4 (A) describe the relationship of stimulation and recoding epochs where both stimulation and data acquisition is represented as either on/off state. Timing parameters T5 – T10 (B) describe how individual stimulation and data acquisition events are related. Stimulation output in B represents the actual current waveform delivered by the SRD stimulator.

3. SRD System Testing

Test were performed on each of the SRD's subsystems to evaluate and demonstrate performance and to ensure that all systems meet the desired project specifications. Evaluations included both bench and in vivo test along with simulations of certain elements of the circuit design.

3.1 Bench Testing

Power System Testing

Power Consumption

Input current was measured for each subsystem and/or primary components of the subsystem during normal operating conditions including stimulation, recording, and wireless transmission. Currents were measured using the µCurrent Gold precision current meter (EEVBlog) and sampled at 10 ksps with a DATAQ Instruments DI-155 data acquisition device. Average current and power consumption was computed over 15 seconds of sampled data. Average cumulative current consumed by the stimulation components, mux and current mirrors, while generating 255 µA biphasic stimulus pulses at 1 Hz, was approximately 1 mA (10 mW). The CPU subsystem, PSoC and LED, average current consumption was 8.2 mA (27.1 mW) during operation. The wireless components including the BT module and indicator LED consumed an average of 13.8 mA (52.1 mW) when operating with sniff mode set to 100 ms and transmitting 100 ms of signal data every 1 second. Average current consumption of the recording subsystem, RHD2216 chip, was 0.9 mA (3.0 mW) while having 12 channels activated and sampling

100 ms of signal data every 1 second at 15 ksps. Thus, when summed together the average current consumed by all the SRD components (excluding voltage converting circuits) was 25.9 mA with an average power consumption of 92.2 mW. These values are summarized Table 4. Efficiencies of the associated power supplies (PS) are discussed in section 0. Using the measured subsystem current and efficiency, a subsystem input current can be calculated (current / efficiency) that represents the portion of total current required at the SRD's battery input. These calculated input currents are 2.5, 9.6, 16.2, and 2.5 mA for the stimulation, CPU, wireless, and recording subsystems respectively. The total calculated average input current was 29.6 mA. For comparison the actual measured input current averaged over 15 seconds of operation was approximately 27 mA.

Table 4. Average current and power consumption.

Subsystem	**Component(s)**	**Current (mA)**	**Power (mW)**	**PS Efficiency (%)**	**PS Input Current Calculated (mA)**
Stimulation	Mux + Mirrors	0.5	5	40	1.25
CPU	PSoC (w/ LED)	8.2	27.1	85	9.6
Wireless	BT (w/ LED)	13.8	52.1	80	16.2
Recording	Intan RHD2216	0.9	3.0	40	2.5
	Totals:	25.9	92.2		29.6
	Total Average Input Current Measured+:				**27 mA**

Battery Life

SRD operating time was initially evaluated using three single-cell lithium-polymer (LiPo) batteries, each with different capacities (850, 1000, and 1300 mAh). Each battery was discharged using a 30 mA constant current load to simulate approximate SRD current consumption based on preliminary calculations and measurements. Constant

current loads were produced using a custom programmable dummy load described in Appendix D. Battery voltages and output currents were monitored and logged using a custom Arduino controlled triple battery test station (Appendix E). Once a battery's voltage drained to 3 V the Arduino disconnected the load from its respective battery to prevent battery damage. Each battery was discharged three times using a different programmable load during each discharge. Average time to discharge each battery from full charge down to the SRD's minimum operating voltage of 3.45 V were approximately 28 hrs. (850 mAh), 36 hrs. (1000 mAh), and 46 hrs. (1300 mAh). Figure 22(A) shows the average discharge curve for all three batteries using 30 mA loads. The 1300 mAh battery had a slightly different discharge curve shape and was attributed to the fact that it was produced by a different manufacture than the other two batteries.

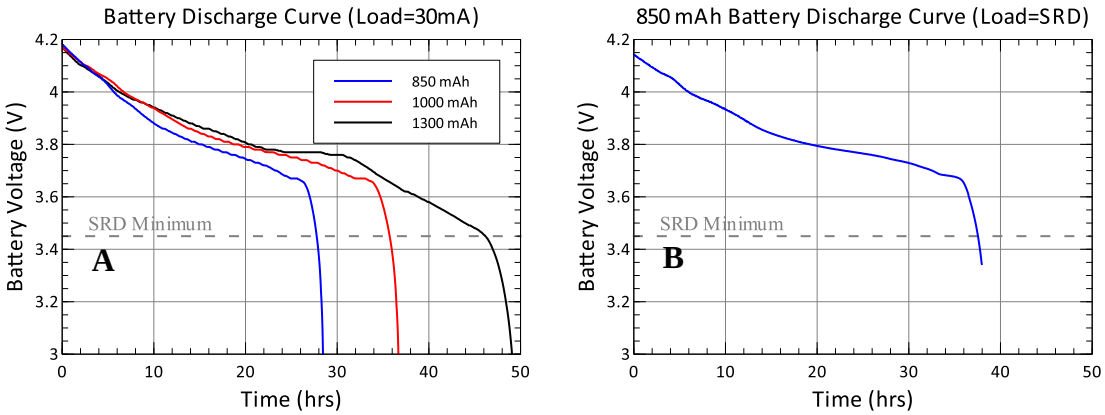

Figure 22. (A) Battery discharge curves for 850, 1000, and 1300 mAh lithium polymer single-cell batteries. Load current was fixed at 30 mA using a programmable load. 1300 mAh battery was made by a different manufacturer. (B) Battery discharge curve for the 850 mAh battery with the SRD operating in automatic mode, recording from single channel, single channel biphasic stimulating across a 10 kΩ resistive load, and transmitting data to the PC.

Based on the above test results the smallest capacity battery would be capable of yielding at least 24 hours of operation as needed for SRD system requirements. A second battery discharge test was performed using the 850 mAh battery and SRD as the load instead of a dummy load. The SRD was setup to operate in automatic mode with biphasic stimulation (±100 µA, 1ms duration, 1 Hz frequency) into a resistive load, and fifty 100ms traces of data being transmitted to the PC every 3 min. This setup would be typical for a prolonged awake animal experiment. Again, an Arduino controlled battery testing station monitored and logged battery voltages and output currents. The battery was allowed to discharge to 3.3 V before being automatically disconnected by the battery testing circuit. Figure 22(B) shows the battery discharge curve of the 850 mAh battery while the SRD operated under normal experimental settings. These results show that the SRD can operate for approximately 37 hours while using the smaller 850 mAh battery as a power source.

Power Supply Efficency

Combining SRD requirements of a small size, long operating time, and battery power necessitate measuring efficiency of the SRD's power supply system. When power supplies convert power from one voltage to another a portion of the input power is wasted due to system inefficiencies. Wasting power is a relevant issue for small, low power designs such as the SRD. Power supply efficiency has a direct impact on the required battery capacity, heat generated by a system, and maximum operating time. A common way to characterize these losses are efficiency measures. The relationship of power and efficiency is defined by

$$Efficiency = \frac{P_{out}}{P_{in}} = \frac{I_{out} * V_{out}}{I_{in} * V_{in}}. \quad (1)$$

Therefore to calculate efficiency of an electrical circuit one must measure the power supply's input current (I_{in}), input voltage (V_{in}), output current (I_{out}) or load, and output voltage (V_{out}) simultaneously.

The SRD converts the LiPo battery voltage into four separate voltages for supplying power to subsystems or domains. A voltage regulator (MIC5393) generates two independent 3.3V rails for digital and analog domains. Stimulation voltage is generated by first converting battery voltages into 5V with a DC-DC step-up converter (AS1302). The second stage then converts the 5V into ±10V.

Efficiency for all three power supply chips (5 voltage rails) were calculated using the following methods. I_{out} and I_{in} were measured using two µCurrent precision current meters. Voltage outputs from the current meters were sampled using a DATAQ Instruments DI-155 data acquisition device. V_{in} and V_{out} were simultaneously sampled using the DI-155. All sampled data was captured in real-time and logged onto a PC using DATAQ Instruments WinDAQ acquisition software. V_{in} for the SRD is simply the battery voltage. I_{out} is the current or load required by the components on the power supply's output. To determine efficiency changes with respect to the battery voltage and the circuit load a constant-voltage bench-top power supply (Circuit Specialist CSI3003X-5) was used to vary V_{in} from 4.2 V to 3.3 V to simulate the 850 mAh battery's typical operating voltage range. The load (I_{out}) was varied using an adjustable constant current dummy load. The range of I_{out} depended on the power supply under test and was based on previous measures of current consumption (see 0) for each power domain. The sequence of measuring the input/output voltages and current was to hold V_{in} at a constant voltage

and then incremental vary I_{out} while logging all current and voltage data. Once I_{out} was swept through its relevant operating range, V_{in} was adjusted by one increment, and varying I_{out} was repeated.

All current and voltage data was sorted and 2D interpolation of calculated efficiencies were performed in MATLAB. Figure 23(A1-D1) shows heatmaps illustrating how efficiency varies with V_{in} and I_{out} for each power supply where the color indicates efficiency using the color bar as reference. Figure 23(A2-D2) shows efficiency vs. V_{in} curves for each power supply at three specific loads.

Efficiency was calculated for each of the dual regulators within the MIC5393 however due to the redundant information, efficiency plots for only one regulator is shown in Figure 23. The MIC5393's efficiency becomes higher as V_{in} approaches the regulated 3.3V V_{out} and increases with increased load as shown Figure 23(A1). Given that the total average current required for digital components was approximately 22 mA (section 0), the efficiency is 60-90%. Additionally, given that during a single battery discharge cycle battery voltage, V_{in}, remains between 4.0-3.6 V for majority of the cycle (Figure 22), the efficiency is 80-90% for majority of the operating time and this power domain consumes about 85% of the total current required by the SRD. The second 3.3 V regulator of the MIC5393 provides power to the analog components which consume 0.9 mA (Figure 23(A1)) and corresponds to an efficiency of 30-40% for the majority of operating time.

The AS1302 and MAX865 were both used for generating stimulation power. The MAX865 is a dual output voltage converter generating a negative (-) and positive (+) 10 V output. Similar to the previous power supply the efficiency for the AS1302,

MAX865(+) , and MAX865(-) show an increase in efficiency with increased loads. AS1302's efficiency curve (Figure 23(B2)) also remains relatively flat, around 40%, over changes in V_{in}. Similarly, efficiency curves remain relatively flat over changes in V_{in} for both the MAX865(+) and (-) power supplies, but V_{in} is fixed at 5.0 V as AS1302 supplies both. Efficiency for the MAX865(+) and MAX865(-) supplies are below 30% and 20% respectively for loads less than 0.5 mA. Note that all three of these power supplies are inefficient at such low loads; therefore, we also measured the average I_{in} for the MAX865 to determine efficiency and current requirements of the stimulation circuit. Given that $I_{in\_MAX865} = I_{out\_AS1302}$ = 1mA and AS1302 efficiency is 40%, a load of 1 mA requires approximately 3.5 mA of input current base on Equation 1. Current consumed by the stimulator system is significantly lower than the digital power domain that includes the PSoC and BT module.

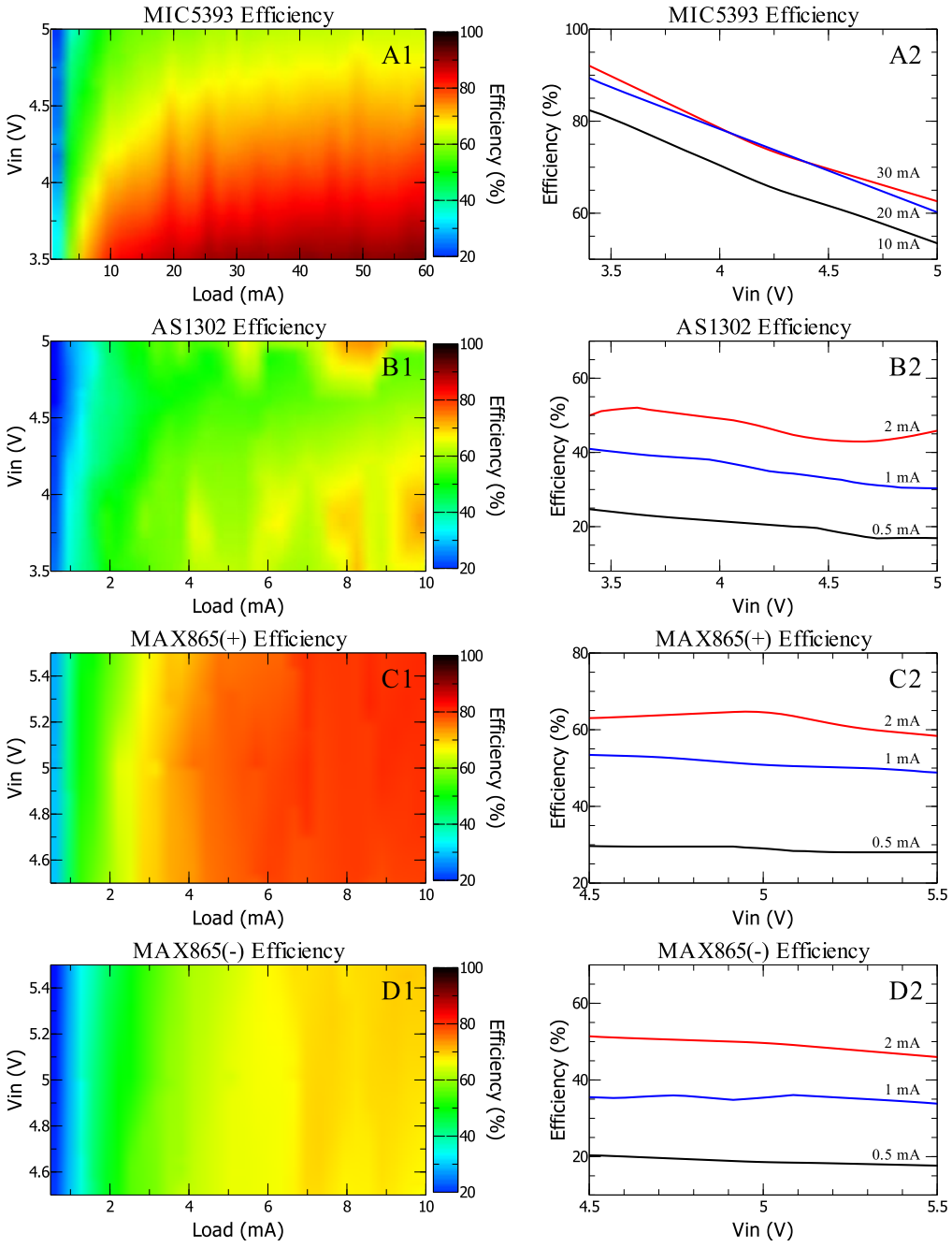

Figure 23. Power supply efficiency for each power supply. Heatmaps (A1-D1) illustrate efficiency with respect to V_{in} and Load. Efficiency curves (A2-D2) illustrate efficiency vs. V_{in} for three specific loads around the respective measured circuit loads.

Thermal Considerations

Waste power during voltage conversion is often manifested as the generation of heat. This heat has the potential to build up within the power supply chip or on/around the neighboring components. If component temperatures rise above their stated operating temperatures unexpected behavior or damage can result. Components on the SRD most likely to generate heat of significant interest are the PSoC, Bluetooth module, and dual LDO power supply chip. Both the PSoC and Bluetooth module are reasonably "grounded" thermally and will not be discussed. However, the dual LDO power supply chip (MIC5393) is supplying almost all the operating current required for SRD operation. The MIC5393 supplies the 3.3 V digital and analog domain and is housed in an extremely small 1.2 mm x 1.2 mm chip. Because of its small size and relatively high current output we must consider the thermal characteristics during maximum operating parameters.

The maximum ambient operating temperature of the dual LDO was calculated based on the output current and the voltage drop across the component. The peak current consumption measured for the digital system and analog system of the SRD were 60 mA and 2 mA respectively. These peak measurements have short durations, but for a conservative estimate of temperature the maximum currents were used. The actual power dissipation (P_D) of the dual LDO can be determined using the equations:

$$P_D = (V_{IN} - V_{OUT1})I_{OUT1} + (V_{IN} - V_{OUT2})I_{OUT2} + V_{IN}I_{GND} \quad (2)$$

$$P_{D(max)} = (5.1V - 3.3V) \times 60mA + (5.1V - 3.3V) \times 2mA + 5.1V \times 90uA \quad (3)$$

$$P_{D(max)} = 112 \text{ mW}. \quad (4)$$

The following basic equation was used to determine the maximum ambient operating temperature, $T_{A(max)}$:

$$P_{D(max)} = \left(\frac{T_{J(max)} - T_{A(max)}}{\theta_{JA}}\right) \quad (5)$$

where $T_{J(max)}$ is the maximum junction temperature and θ_{JA} is the junction-to-ambient thermal resistance of the device as defined in the datasheet. Substituting values into the above and solving for $T_{A(max)}$ yields:

$$T_{A(max)} = T_{J(max)} - \left(P_{D(max)}\theta_{JA}\right) \quad (6)$$

$$T_{A(\max)} = 125\,°C - \left(0.112W \times 173\,°\frac{C}{W}\right) \quad (7)$$

$$T_{A(max)} = 105.6\,°C \quad (8)$$

Therefore, a dual 3.3 V application, such as this one, with corresponding 60 mA and 2 mA output currents can operate normally in an ambient temperature of approximately 105 °C. The maximum measured operating temperature recorded within the SRD enclosure or on the PCB after 3 hours of operation on a rat was 30°C which is below that of the maximum allowed ambient operating temperature calculated above.

Recording Testing

In order to characterize the SRD's filters both simulations and physical measurements were performed. The amplifiers within the RHD2000 series digital electrophysiology interface chips have a band-pass behavior, passing signals between a user-programmable lower cutoff frequency (f_L) and upper cutoff frequency (f_H). The cutoff frequencies f_L and f_H represent points where the gain has decreased by a factor of 3

dB. Gain expressed linearly (e.g., in V/V) is converted to dB (decibels) using the following relationships: $\text{Gain}_{\text{dB}} = 20 \cdot \log_{10} \text{Gain}_{\text{V/V}}$.

Upper Cutoff Frequency (f_H): The upper limit of the amplifier pass band has a three-pole 3rd-order Butterworth low-pass filter characteristic. This filter is described by the following complex transfer function:

$$H_H(s) = \frac{1}{\left(\frac{s}{\omega_H}\right)\left(\left(\frac{s}{\omega_H}\right)^2 + \frac{s}{\omega_H} + 1\right)} \tag{9}$$

where $s = j\omega$, $j^2 = -1$, and ω is frequency in radians/second. The upper cutoff frequency is expressed as $\omega_H = 2\pi f_H$. Solving for amplitude (i.e., gain), and writing frequency in units of Hertz for convenience, results in:

$$|H_H(f)| = \frac{1}{\sqrt{1 + \left(\frac{f}{f_H}\right)^6}} \tag{10}$$

Solving the 3rd-order Butterworth filter characteristic for phase angle, results in:

$$\angle H_H(f) = -\tan^{-1}\left(\frac{2\left(\frac{f}{f_H}\right) - \left(\frac{f}{f_H}\right)^3}{1 - 2\left(\frac{f}{f_H}\right)^2}\right) \tag{11}$$

Lower Cutoff Frequency (f_L): The lower limit of the amplifier pass band has a simple one-pole high-pass filter characteristic. This filter is described by the following complex transfer function:

$$H_L(s) = \frac{1}{s + \omega_L} \tag{12}$$

where $\omega_L = 2\pi f_L$ is the lower cutoff frequency. Solving for amplitude (i.e., gain), and writing frequency in units of Hertz for convenience, results in:

$$|H_L(f)| = \frac{1}{\sqrt{1 + \left(\frac{f_L}{f}\right)^2}} \tag{13}$$

The gain is close to unity for frequencies much less higher than f_L. At the cutoff frequency f_L, the gain is $1/\sqrt{2}$ = -3 dB. Solving for phase angle gives the following:

$$\angle H_L(f) = \tan^{-1}\left(\frac{f_L}{f}\right) \tag{14}$$

Digital, Low Cutoff Frequency (f_D): The RHD2000 series chips contain an optional digital high-pass filter to remove small DC voltage offsets that accumulate in the analog amplifier circuitry. This digital filter closely approximates the characteristics of the continuous-time one-pole high-pass filter described above for the lower cutoff frequency f_L. The gain and phase equations for the digital offset removal filter may be determined by using Equations 15 and 16 and substituting f_D for f_L.

Complete Amplifier Transfer Function: The complete amplifier transfer function is calculated by multiplying the three complex functions that define each filter. This is equivalent to multiplying their amplitudes (gains) and summing their phase angles:

$$\begin{aligned} \left|H_{amp}(f)\right| &= |H_L(f)| \cdot |H_H(f)| \cdot |H_D(f)| \\ &= \frac{1}{\sqrt{1 + \left(\frac{f_L}{f}\right)^2}} \cdot \frac{1}{\sqrt{1 + \left(\frac{f}{f_H}\right)^6}} \cdot \frac{1}{\sqrt{1 + \left(\frac{f_D}{f}\right)^2}} \end{aligned} \tag{15}$$

$$\begin{aligned} \angle H_{amp}(f) &= \angle H_L(f) + \angle H_H(f) + \angle H_D(f) \\ &= \tan^{-1}\left(\frac{f_L}{f}\right) - \tan^{-1}\left(\frac{2\left(\frac{f}{f_H}\right) - \left(\frac{f}{f_H}\right)^3}{1 - 2\left(\frac{f}{f_H}\right)^2}\right) + \tan^{-1}\left(\frac{f_D}{f}\right) \end{aligned} \tag{16}$$

Gain and phase calculations were computed in MATLAB using a lower cutoff frequency of 100 Hz and upper cutoff frequency of 1 kHz representing typical bandwidths for extracellular recordings performed in our lab. Gain and phase were also generated with the optional digital high-pass filter enabled and set to 318 Hz.

Frequency responses for the RHD2000 was measured by using the same filter bandwidths and digital filter options as above and sweeping a sine wave with known amplitude through a range of frequencies. At each frequency step the input magnitude, sampled output magnitude, and frequency was noted. Gain verse frequency curves were then generated.

Figure 24(A) shows frequency response plots of the simulated gain and gain computed with bench measurements. Figure 24(B) shows frequency response plots of the simulated phase. Signals near the cutoff frequencies are subject to phase shifts due to the action of the filters. All plots we produced with analog filter bandwidths set to 100 Hz – 1000 Hz and the optional digital high-pass filter either disabled (dashed curves) or set to 318 Hz (solid curves).

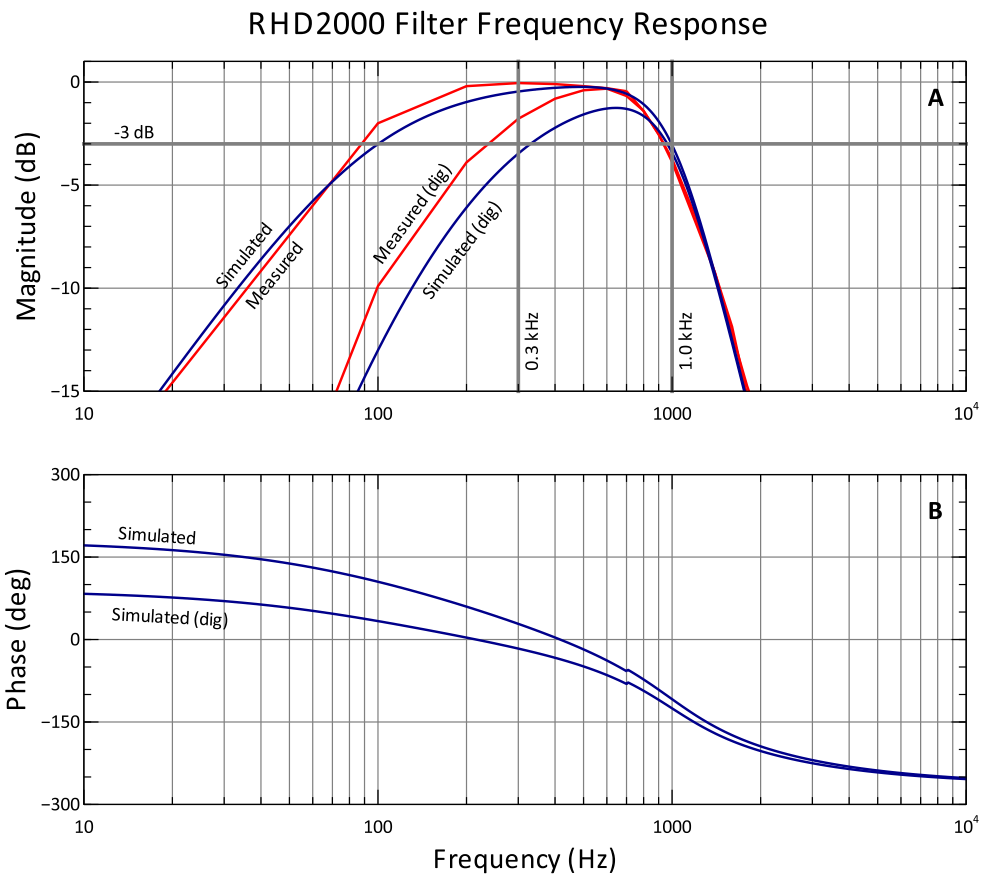

Figure 24. RHD2000 frequency response. (A) Frequency response of simulated (blue) and measured (red) gains. Lower cutoff frequency (F_L) was set to 100 Hz and high cutoff frequency (f_H) was set to 1 kHz. (B) Frequency response of simulated phase angle. Dashed curves represent frequency responses with the digital high-pass filter (offset removal filter) disabled while solid curves represent the digital filter enabled cutoff frequency F_D set to 318 Hz. Vertical lines in (A) represent the desired overall filter bandwidth of 300 Hz – 1 kHz. The horizontal line in (A) marks the -3 dB gain.

Simulated -3 dB cutoff frequencies for the RHD2000 were F_L = 100 Hz and F_H = 995 Hz with no digital filter and F_L = 329 Hz and F_H = 964 Hz when the digital filter was set to 318 Hz (Figure 24(A)). Phase angle shifts near the programmed lower cutoff frequencies were 104° with no digital filter and -16° with digital filter set to 318 Hz (Figure 24(B)). Phase angle shifts near the programmed upper cutoff frequency were -108° without digital filter and -125° with digital filter set to 318 Hz (Figure 24(B)).

Measured -3 dB cutoff frequencies for the RHD2000 at the bench were F_L = 90 Hz and F_H = 933 Hz with no digital filter and F_L = 240 Hz and F_H = 933 Hz when the digital filter was set to 318 Hz (Figure 24(A)). With no digital filter enabled both the simulated and bench results were comparable. With the digital filter enabled the -3 dB lower cutoff frequency F_L was 89 Hz lower in bench test verses simulated results. F_H was comparable for both bench and simulated results. Measured lower cutoff frequency F_L was not ideal relative to the desired 300 Hz but acceptable. The measured lower cutoff frequency could be shifted closer to 300 Hz by choosing a higher analog F_L or higher digital F_L if desired.

Stimulator Testing

The stimulator's range of operation and ability to generate monophasic, biphasic, and pseudophasic waveforms based on user defined parameters was assessed. Stimulating current was applied to a 10 kΩ resistive load while measuring output current using a digital oscilloscope (Rigol DS2702), and µCurrent precision current meter. Figure 25 shows measured stimulation current waveforms for monophasic (cathodic: 100 µA, 1 ms), biphasic (cathodic: 100 µA, 0.5 ms; anodic: 100 µA, 0.5 ms), and pseudophasic (cathodic: 75 µA, 0.5 ms; anodic: 25 µA, 1.5 ms). The SRD was able to produce accurate stimulation amplitudes and timing characteristics using a resistive load. In vivo stimulator test are discussed in later sections.

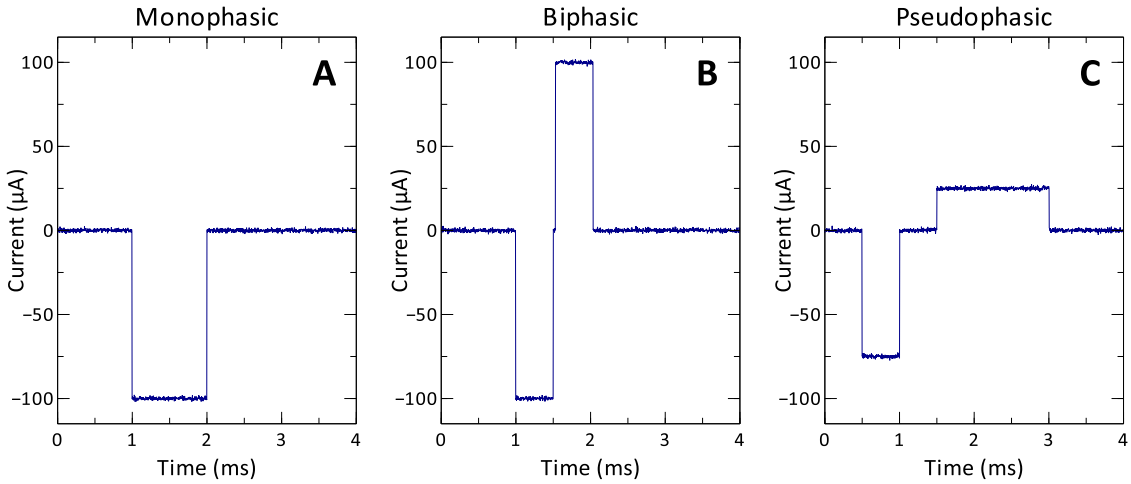

Figure 25. Stimulator bench test. Measured stimulation current waveforms for (**A**) monophasic (cathodic: 100 µA, 1 ms), (**B**) biphasic (cathodic: 100 µA, 0.5 ms; anodic: 100 µA, 0.5 ms), and (**C**) pseudophasic (cathodic: 75 µA, 0.5 ms; anodic: 25 µA, 1.5 ms)

Stimulation tests were also conducted on the bench while electrodes were placed in saline solution. These results are not shown due to the inclusion of more relevant in vivo test results found in section 3.2. Additional results not shown are aspects of the current steering. However, Figure 25 demonstrates successful operation of the SRD's current steering abilities at producing both a cathodic and anodic pulse. Switching time of the multiplexor used for current steering added only a few microseconds to the rise and fall time of current pulses, and adds less than 5 ohms of resistance to the current path.

Wireless Testing

Basic evaluations of data transmission capabilities and wireless transmission range of the SRD were performed. First we confirmed that the SRD was capable of sending captured data to the PC before the next data acquisition event occurred. This was evaluated by calculating the maximum time needed to send data to the PC per acquisition event. The SRD's BT module was capable of transmitting up to 960,000 bits/s. Standard

values of 115,200 and 230,400 bits/s were used by the SRD, but the former was set as the default rate. However, when framing bits are considered the effective data rate is reduced. The SRD used two additional framing bits (1 start bit and 1 stop bit) per byte (8bits) of data acquired or 10 bits per 8 effective bits. To compute the maximum time needed to transmit a single trace of data we multiply the maximum amount of data required for one trace by the effective data rate where the maximum amount data per trace is a multiple of the ADC bit resolution, sampling rate, simultaneous channel count, and maximum signal trace length plus any extra data for headers. This equated to less than 50 kbits when sampling two channels at the maximum sample rate of 15 ksps and using the maximum trace length of 100 ms (16 bits x 15 ksps/ch x 2 ch x 0.1 s + header < 50 kbits). Therefore, the maximum time required to send a 100 ms trace of data for two simultaneous channels was calculated to be 0.55 s (50 kbits / 115,200bits/s * 10/8 bits/bits) for the rate of 115,200 bits/s and 0.27 s (50 kbits / 234,000bits/s * 10/8 bits/bits) for the rate of 234,000 bits/s.

Next, an evaluation was performed to see whether the SRD transmission rates of 115,200 and 230,400 bits/s were sufficient to send data in a real world test using maximum sampling rates. A known sinusoidal signal was sampled by the SRD and transmitted to the PC and subsequently compared to the data received after wireless transmission. The SRD was successful at accurately capturing and sending data to the PC.

Finally, the SRD's wireless range was evaluated by increasing the distance between the SRD and PC while monitoring sampled signals. Both in vivo and sinusoidal

signals were used during range testing. Wireless range of the SRD was at least 100 ft. unobstructed and at least 50 ft. with one wall between the SRD and PC.

External IR Sync

Testing of the external IR sync system was performed to characterize two essential characteristics: (1) operating distance between external IR trigger device and SRD and (2) timing latency between external events and SRD action. Total latency was evaluated as two components: (1) the latency between initiation of the input/trigger signal and the time at which the PSoC input pin voltage reaches its lower threshold value and (2) the latency between PSoC input pin reaching threshold and start of SRD sampling or stimulation depending on the mode of operation.

Operating distance and the second PSoC input latency component above were tested simultaneously. Distance (6 in – 24 in) and angle (30 – 60 degrees relative to horizontal) were adjusted while simultaneously capturing the input/trigger signal for the external IR trigger device and capturing the voltage at the PSoC's input pin for the IR detector. Additionally the effect of ambient light was tested by performing these test with the room lights on and off. Pin latencies shown in Figure 26 were determined by measuring the time from the start of the trigger signal until the point at which the pin voltage crosses the lower threshold value shown as the dotted grey line at 0.99 V. The PSoC pin thresholds are 0.3 x Vddio which equates to 0.99 V for this application. Trigger signals were 10 ms pulses generated by a Winston Electronics Model A65 timer and are shown as the solid grey curve labeled as "trigger".

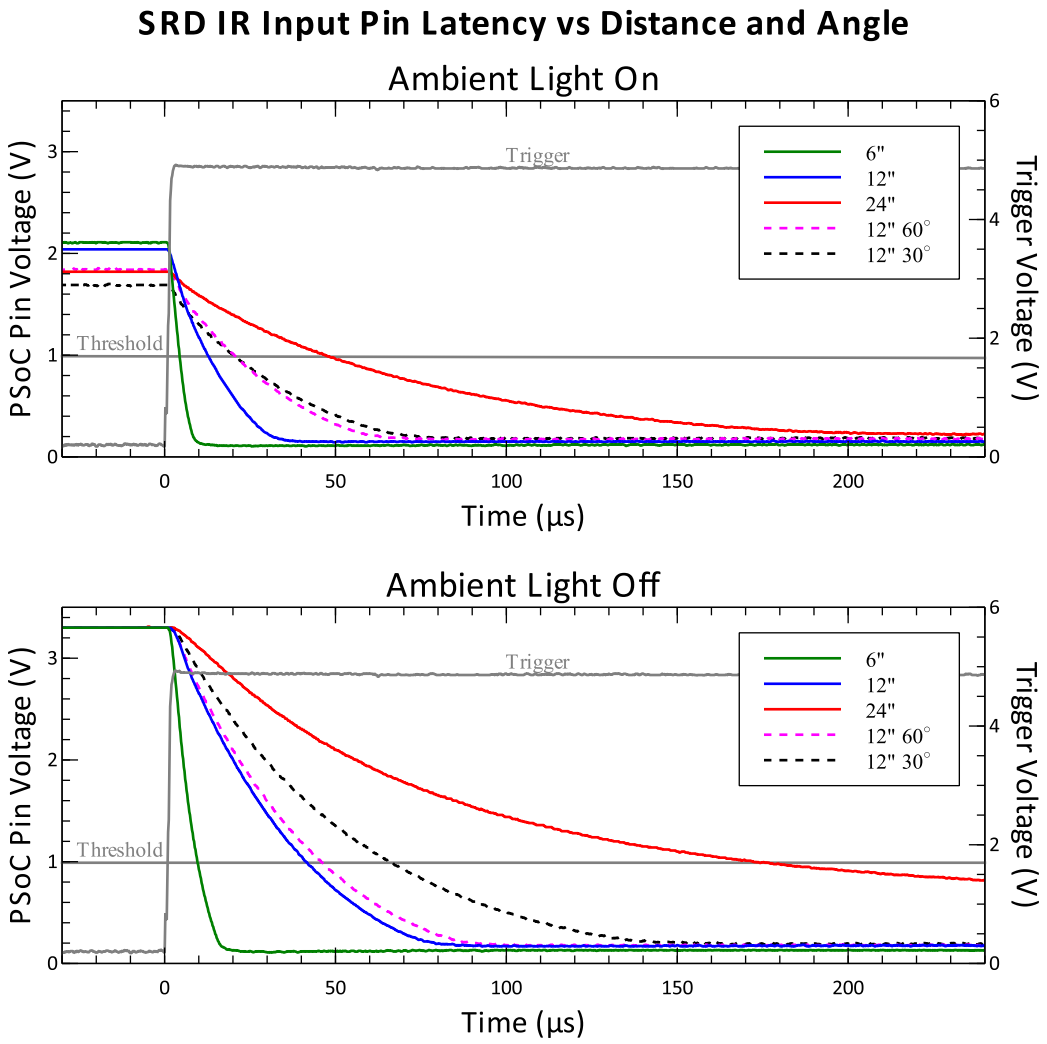

Figure 26. External IR system latencies at PSoC pin comparing various distances and angles between external IR trigger device and SRD. Latencies represent time from start of trigger signal (grey curve) to the time point at which pin voltage drops below the pin threshold voltage (dashed grey line). Pin limit low threshold is 0.3xVddio or approximately 0.99V. Top plot represent latencies with ambient lights turned on. Bottom plot represent latencies with ambient lights turned off.

IR system latencies at the pin with ambient lights on were 5, 13, 49, 21, and 20 µs for positions of 6”, 12”, 24”, 12” at 60°, and 12” at 30° respectively. Latencies at the pin with ambient lights off were 10, 42, 176, 46, and 66 µs for positions of 6”, 12”, 24”, 12” at 60°, and 12” at 30° respectively. As expected latencies with ambient lights turned on produce shorter latencies because the IR phototransistor used on the SRD is also partially sensitive to light wavelengths outside the 850 nm peak sensitivity range. Therefore, ambient lights cause partial activation of the transistor allowing current to flow from the pin’s resistive pull-up circuitry to ground and ultimately lowering the baseline voltage at the pin. Lower baseline voltage leads to less time required for the pin voltage to drop below threshold levels when activated by IR light. Also, at 12” introducing angles of 30° and 60° relative to horizontal increase latencies by less than 8 µs with ambient lights on and less than 24 µs with ambient lights off. It is not expected that distances greater than 12”-24” would be needed for experiments requiring externally synced events.

Total SRD latencies were also evaluated at 12” by measuring the time from the start of trigger signal to initiation of data sampling by the SRD when operating in external recording mode. Results show that the SRD starts sampling approximately 18 ms after the external IR device initiates an IR pulse.

3.2 In Vivo Testing

In vivo test evaluated the SRD’s ability to stimulate and record in living tissue of the rat SI cortex. Test of the SRD’s stimulator, recording, and simultaneous stimulation and recording capabilities are discussed below.

Animal Preparation and Surgery

Methods for animal preparation, surgery, cortex mapping, and electrode insertions into cortex are described in detail in Section 4.1. A summary of animal preparation methods include: animals were anesthetized, incision made in scalp, craniotomies performed over each SI forelimb cortex, and dura removed. Electrodes were then inserted into homotopic representations within forelimb cortices and connected to the SRD circuit for testing.

In Vivo Stimulator Testing

The SRD was used to deliver monophasic, biphasic, and pseudophasic current pulses to cortical layer V of the rat SI cortex. Stimulation electrodes used in these tests were platinum/iridium alloy metal microelectrodes (Microprobes) with impedance of 100 kΩ at 1 kHz. Stimulation current and voltage drop across the stimulating electrode were captured with a Rigol DS2072 digital oscilloscope and μCurrent precision current meter. Figure 27 shows four stimulation current waveforms with accompanying voltage waveforms delivered to rat cortex by the SRD using various amplitude and timing settings. Based on these stimulator tests the maximum compliance voltage required to generate 100 μA using a 100 kΩ electrode was 2.6 V and well below the allowable 10V SRD compliance voltage. Also, leakage current measured from the SRD during interphase intervals was 9 nA.

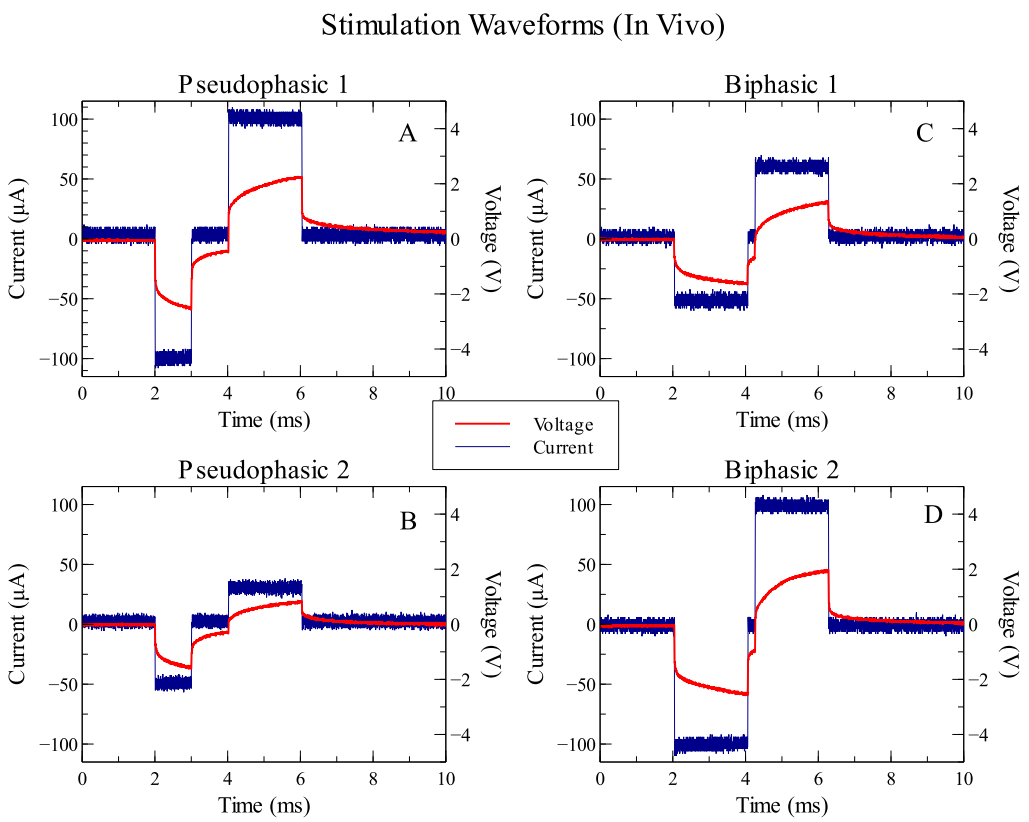

Figure 27. In vivo examples of pseudophasic and biphasic constant current stimuli delivered to rat cortex with 100 kΩ Pt/Ir Microprobe electrode. Measured output current is shown in blue and simultaneously measured voltage drop across the tissue/electrode load is shown in red.

In Vivo Simultaneous Recording and Stimulation

To demonstrate the SRD's ability to simultaneously record and stimulate in vivo we combined recording in rat SI forelimb cortex while simultaneously delivering intra-cortical microstimulation (ICMS) to the homotopic forelimb cortex in the opposite hemisphere. Corticocortical (cortex to cortex) evoked responses were recorded using both the existing rack recording/stimulation system (Figure 28(A)) and the SRD (Figure 28(B)) for comparison purposes. All signals were recorded during the same experiment. Blue traces represent multiple 100 ms recordings overlaid while the red trace represents a

mean instantaneous root mean square (RMS) signal. The RMS signal represents the averaged time-varying signal power within the selected cortical signal traces. Definitions and equations for the RMS signal are discussed in 0. Both systems show the typical stimulus artifact denoted by a large voltage deflection starting at time = 10 ms. Following the stimulus artifact, evoked cortical cell activity occurs in response to ICMS in the opposite forelimb cortex. The burst of cell activity produced by stimulation is defined as an evoked response. The SRD was capable of repeatedly recording evoked responses. Evoked responses in Figure 28 are indicated by the increase in instantaneous mean RMS signal and increases in signal peak-to-peak amplitude starting approximately 7-10 ms following stimulation. One notable observation was that signal-to-noise ratio (not quantified) was greater for the SRD system than the rack system. Alternatively, the background noise of the SRD system was lower than the rack system.

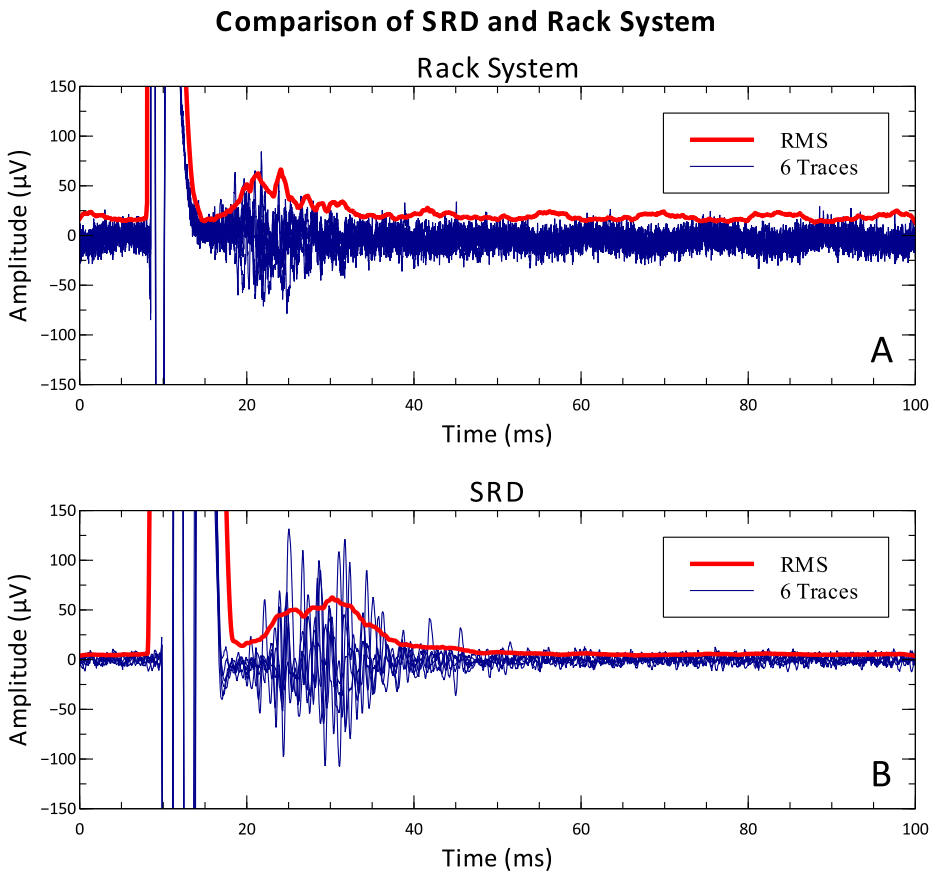

Figure 28. In vivo examples of corticocortical evoked responses. ICMS (1 Hz, 50 µA) was delivered to forelimb somatosensory cortex representing digit 4. Six 100 ms traces (blue) were recorded in the homotopic cortex and overlaid (blue) for both the (A) rack system and the (B) SRD system. Mean instantaneous RMS signals (red) were computed using a 2 ms window.

In Vivo IR Sync Test

In vivo test of the SRD's ability to synchronize with external stimulation systems was also performed. Evoked cortical signals were recorded in SI forelimb cortex while electrically stimulating the contralateral forelimb skin surface with an external stimulator probe (100 μA, 1 ms, 1 Hz). The contralateral hindlimb and ipsilateral forelimb (not shown) were also stimulated for control testing. The external IR sync device was connected to the external system and positioned 12 inches above the SRD (see Figure 18). The SRD was able to record contralateral forelimb evoked responses (Figure 29(A)) while also recording the absence of contralateral hindlimb evoked responses (Figure 29(B)) as expected.

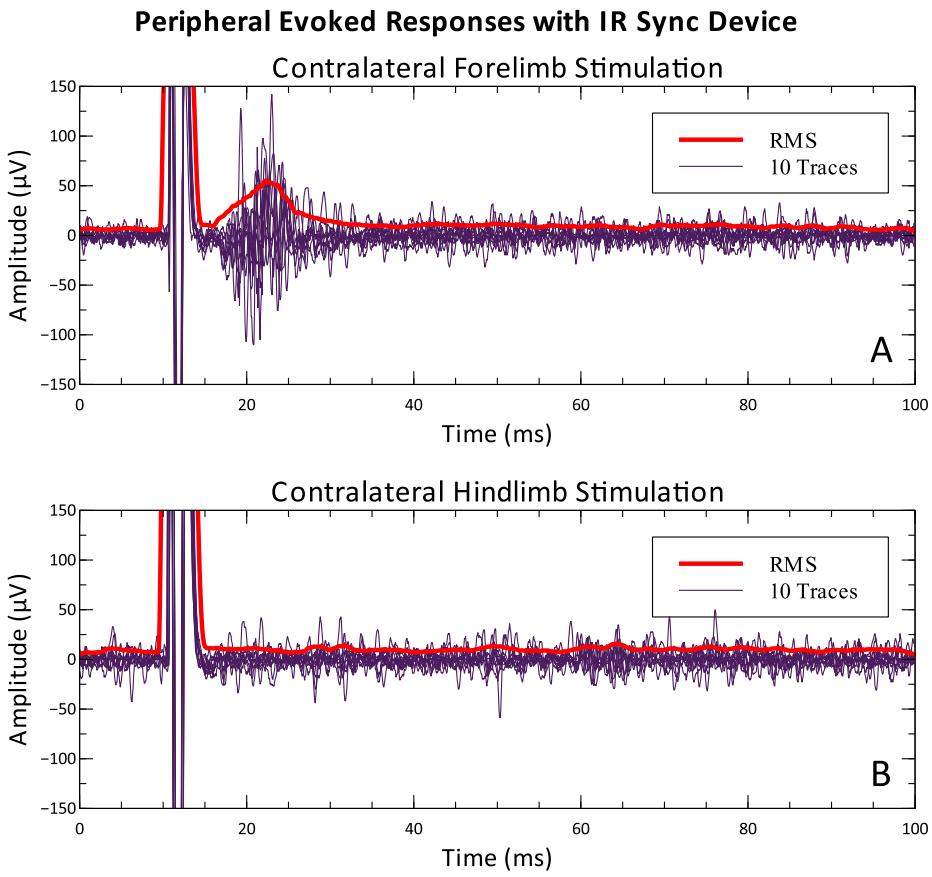

Figure 29. In vivo example of using the IR Sync Device to synchronize the SRD with an external stimulation system. Ten peripheral evoked responses (purple) were recorded during electrical stimulation (1 Hz, 50 µA, 1 ms duration) of contralateral (A) forelimb and (B) contralateral hindlimb. Mean instantaneous RMS signals (red) were computed using a 2 ms window.

3.3 Testing Summary

The SRD's performance was evaluated using bench testing and in vivo testing in anesthetized rats. Results confirmed that the SRD was capable of delivering accurate constant-current monophasic, biphasic, and pseudophasic stimulus waveforms to both bench top resistive loads and in vivo rat cortex. Our telemetry controlled SRD was also capable of simultaneously recording cortical signals that were comparable to those recorded using rack mounted recording and stimulating equipment.

4. SRD Evaluation: Training Cortical Circuits in Anesthetized Animals

In the above sections we described SRD system design and subsequent testing of that system. In order to progress towards implementing the SRD in awake animal models we first evaluated the system's ability to enhance forelimb SI-to-SI interhemispheric pathway and produce functional reorganization in anesthetized animals. Specifically we used the SRD to deliver chronic ICMS to a physiologically identified region in SI cortex and record evoked responses in a homotopic site in contralateral SI to test the hypothesis that chronic ICMS delivered by the SRD enhances the interhemispheric pathway and leads to functional reorganization in anesthetized rats.

4.1 Methods

Animal Preparation and Surgery

These experiments conformed to The Guide for the Care and Use of Laboratory Animals (NIH publication No. 86-23, revised 1985) and have been approved by the Institutional Animal Care and Use Committee at the University of Tennessee Health

Science Center. Sprague Dawley rats (n=3) were anesthetized with ketamine/xylazine (100 mg/kg) and supplemented with 50 mg/kg to maintain areflexia. The hair on top of the head and forelimb was shaved. The animal was placed on a water-circulating heating pad to maintain body temperature between 36.5° C and 38.0° C. Animals were placed into a Narishige stereotaxic surgical frame throughout surgery and electrophysiological recordings. A local anesthetic (Marcaine) was injected into the scalp and midsagital incision was made in the skin to expose the underlying bone. Anterior-posterior and medial-lateral measurements were taken in reference to Bregma to locate the presumptive region of SI representing the forepaw, wrist or forearm, and two craniotomies were performed over both hemispheres. The dura was pierced using a small hook fashioned from a sterile hypodermic needle of small gauge (e.g. < 28 gauge). The tip of the needle was pressed against a flat surface (such as the flat part of a scalpel) and tilting slightly to form a 90 degree bend at the point. This hook was used to catch the surface of the dura, and lift upwards from the brain surface. After piercing the dura, it was then cut using micro scissors or torn using two pair of fine tip forceps. Once cut, the dura was reflected outward and the brain surface was irrigated with warm saline (0.9%) to prevent drying. A recording chamber was constructed around both craniotomies using dental cement and the exposed cortices were bathed in silicon fluid (10,000 cSt).

Physiological Mapping

The overall goal of physiological mapping was to identify homotopic forelimb representations in layer V of both SI cortices because we had previously shown that interhemispheric connectivity existed between these regions [174]. A carbon fiber electrode [175] was inserted into SI of one hemisphere using a Canberra-type Narishige

microdrive. One or more electrode insertion locations were made to locate desired receptive fields and were based on stereotaxic coordinates from previous experiments. Receptive field(s) of SI neurons were evaluated by monitoring extracellular signals from the carbon fiber electrode while simultaneously mechanically stimulating the contralateral forelimb skin surface with a small wooden probe. Extracellular signals were amplified using a custom amplifier (1500x) and sent to both an audio monitor and oscilloscope. Receptive fields were defined by the area of skin surface that evoked maximum audible cortical responses to minimal stimulation. Receptive fields were evaluated for depths of 700 to 1400 μm below the cortical surface. Once a desired receptive field was located the electrode was held in that location while a second carbon fiber electrode was inserted into a comparable location in SI of the opposite hemisphere. Physiological mapping was then performed as above for the second electrode. In order to find a similar receptive field on the contralateral forelimb.

Interhemispheric Pathway Enhancement

After mapping homotopic receptive fields, interhemispheric connectivity between mapped representations was examined. ICMS (biphasic pulse, 1.5 × baseline threshold, 1 ms duration, 1 Hz) was delivered by an AM Systems (Model 2100) stimulator to the electrode (stimulating electrode) in contralateral SI cortex while using the other electrode (recording electrode) to record corticocortical evoked responses in ipsilateral SI cortex. Depth adjustments within layer V were made to either the recording or stimulating electrode in search for the minimum threshold to evoke corticocortical responses. The contralateral (stimulating) carbon fiber electrode was then replaced with a lower impedance platinum/iridium electrode (Microprobes, 10 kΩ at 1 kHz). Both receptive

fields and corticocortical evoked responses were rechecked and minimum stimulation thresholds to produce corticocortical evoked responses were noted.

All hardware used during mapping and corticocortical response verification was disconnected from the two electrodes and replaced by the SRD. The SRD was then used to deliver ICMS (biphasic pulse, 1.5 × baseline threshold, 1 ms duration, 1 Hz) to the stimulating electrode in layer V for 0.5-3 hrs. Baseline threshold was defined as the minimum stimulation current required to evoke a cortical response. Corticocortical evoked responses to ICMS were recorded throughout chromic stimulation to determine level of enhancement.

Functional Reorganization

To examine functional reorganization ipsilateral evoked responses following forelimb electrical stimulation of the ipsilateral forelimb were collected at 0.5 – 1.0 hour intervals. 20-50 consecutive peripheral evoked responses were captured prior to, during, and following chronic ICMS. Lastly, after functional reorganization had been examined, electrolytic lesions (5-7 µA, 10 s) were made at both stimulating and recording sites using a custom built lesion maker.

Histological Procedures

Animals were euthanized by administering a lethal dose of Nembutal (100 mg/kg, i.p.) and transcardially perfused. Excised brains were fixed in paraformaldehyde, sectioned (100 µm), and stained with 3,3'-Diaminobenzidine (DAB, Sigma D5637) to examine stimulation/recording sites in relation to the barrel field.

Data Analysis

Transcallosal pathway enhancement was defined as a 50% increase in corticocortical evoked response amplitudes and/or 50% increase in peak amplitude of the average instantaneous RMS signal within the time window corresponding to corticocortical evoked response activity (7 - 20 ms). Functional reorganization was defined as the appearance of evoked responses in ipsilateral forelimb cortex following ipsilateral forelimb peripheral stimulation that was not present prior to enhancement. All signal analysis was performed in MATLAB.

The average instantaneous RMS signal was computed as follows. If *x* is a discrete time series signal the time-varying or instantaneous RMS power of *x* can be computed using an *m*-point rectangular window centered at each point in the signal using the equation below. At each data point *x(j)* the RMS value of *m* data points around *j* is computed yielding a signal of the same size as *x* and contains, for each point in *x*, an estimate of the instantaneous power expressed in the signal. The instantaneous RMS signal is defined by

$$RMS(i) = \sqrt{\frac{1}{m}\sum_{j=i-m/2}^{i+m/2} x(j)^2} \tag{17}$$

where *m* is the rectangular window size and *x* is the original time series signal. Therefore, the mean instantaneous RMS signal of multiple cortical signal traces is the mean of each computed instantaneous RMS signal as defined by

$$RMS_{mean}(i) = \frac{1}{n}\sum_{i=1}^{n} RMS(i) \tag{18}$$

where *n* is the number of RMS signals.

Instantaneous RMS signals are often used in surface electromyography (EMG) to determine muscle contraction onset and quantifying motor unit recruitment levels [148,176,177]. Surface EMG signals have bandwidths and signal structure similar to that of multi-unit extracellular cortical recordings like the recorded signals used in this project [178]. Therefore instantaneous RMS signals were relevant and useful tool in comparing our recorded signals. The RMS statistic chosen for comparison is the peak value of the mean instantaneous RMS signal within the time window corresponding to the associated evoked response activity.

4.2 Results

The SRD's ability to produce interhemispheric pathway enhancement and functional reorganization in layer V SI cortex was examined between homotopic wrist representations in 3 animals. An example of stimulation and recording sites are shown in Figure 30. Lesions in each hemisphere of the photomicrograph indicate locations of stimulation (right) and recording (left) electrodes. All recordings and stimulation sites were localized to layer V.

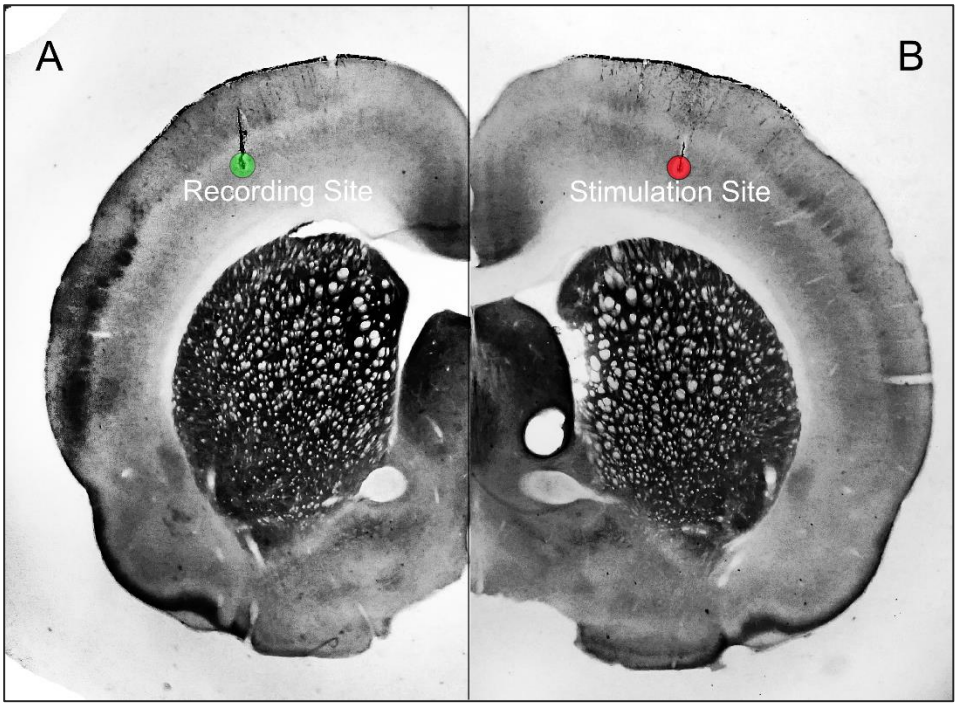

Figure 30. Photomicrograph of coronal slice showing lesions made at stimulation and recording electrode tips. Lesions indicate recording and stimulation locations within the cortex. Both the recording (green circle) and stimulation (red circle) electrode were located in layer V. Panel A shows the left hemisphere with recording electrode site, and panel B shows the right hemisphere with stimulating electrode site. Subject: JTFB_01

Table 5 summarizes experimental results of using the SRD in anesthetized animals. Of the 3 anesthetized rats used, chronic ICMS induced interhemispheric enhancement and functional reorganization in 2 animals. Stimulation and recording depths were 1000 µm for all animals. ICMS thresholds to produce corticocortical evoked responses were 15-20 µA. Following 45 minutes of chronic ICMS (30 µA, BCI_Test_4) and 30 minutes of chronic ICMS (30 µA, JTFB_1), enhancement of evoked responses were evaluated by capturing 10 consecutive responses to ICMS. Percent changes in corticocortical peak amplitude of the average instantaneous RMS signal compared to baseline evoked responses were 113% and 80% for BCI_Test_4 and JTBF_1, respectively, and both exceed our definition of enhancement (50% increase). Immediately

following the assessment of enhancement, functional reorganization was evaluated by recording evoked responses to peripheral electrical stimulation of the ipsilateral wrist. Ipsilateral peripheral stimulation evoked a response in both BCI_Test4 (15-44 ms post-stimulation) and JTFB_1 (16-34 ms post-stimulation) that were not present at baseline (Figure 31 and Figure 32).

Table 5. Interhemispheric pathway enhancement and functional reorganization summary data using the SRD in anesthetized animals.

Experiment No.	Receptive Field	Depth Rec/Stim (μm)	Enhance-ment	CoCo Stim Threshold (μA)	CoCo RMS % Change	Ipsilateral Response	Ipsilateral Stimulation Current (μA)	Time to Ipsilateral Response (min)
BCI_Test_4	W	1000/1000	Y	20	113%	Y	100	45
BCI_Test_6	W	1000/1000	N	15	-	N	200	-
JTFB_1	W	1000/1000	Y	20	80%	Y	100	30

Legend: Columns 1-3 show the experiment number, receptive fields, and electrode site depths for each experiment. Columns 4-6 show whether ICMS produced cortical enhancement, the ICMS threshold to produce corticocortical evoked responses, and the % change in peak RMS after chronic ICMS compared to baseline. Columns 7-9 show functional reorganization data including the ability to produce ipsilateral responses, the peripheral stimulation used to evoke ipsilateral responses, and the relative time at which ipsilateral responses were first observed. W: wrist, CoCo: corticocortical

Figure 31 and Figure 32 show ten examples of evoked responses (blue) to ICMS and to ipsilateral electrical stimulation are shown along with the corresponding average instantaneous RMS signal (red) for the two anesthetized animals that displayed enhancement and functional reorganization. After 30-45 minutes of chronic ICMS, corticocortical evoked responses showed a visual increase in cortical signal amplitudes and a measurable increase in peak RMS (Figure 31 and 32, panel A2). Again, following verification of enhancement it was then observed that stimulation of the ipsilateral

forelimb produced evoked cortical responses (Figure 31 and 32, panel B2) that were absent prior to enhancement (panel B1).

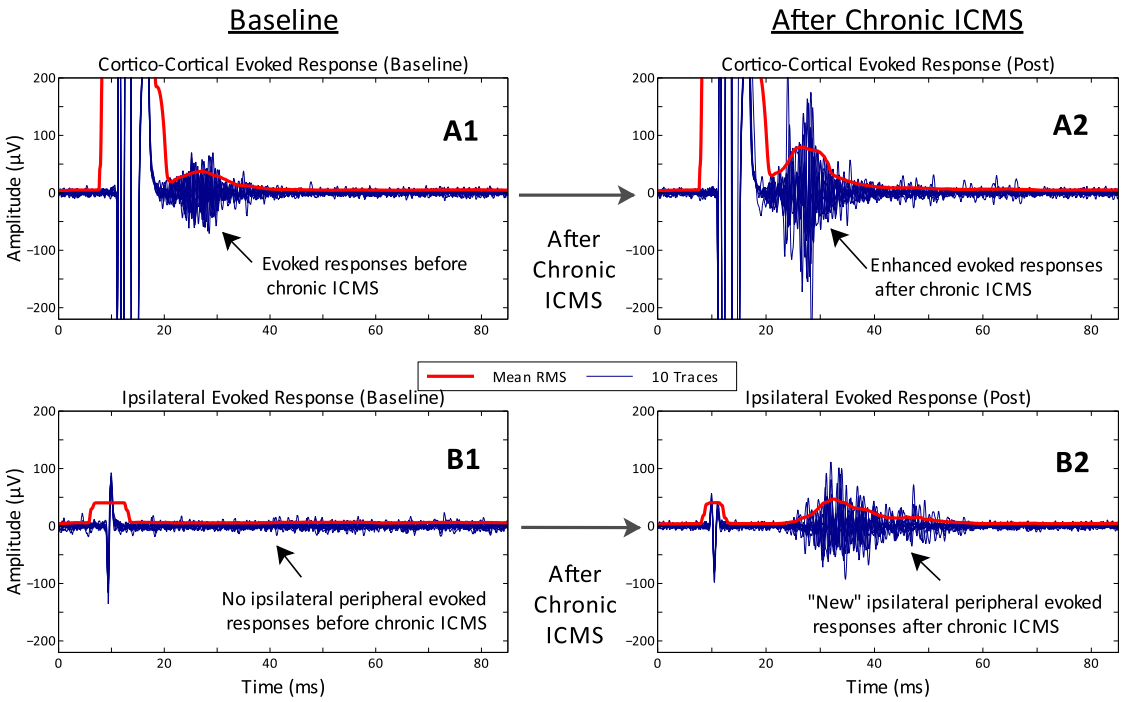

Figure 31. Experiment: BCI_Test_4. Illustration of enhancement and functional reorganization using the SRD in anesthetized rat. Each graph contains 10 traces (blue) and average instantaneous RMS signal (red). ICMS evoked responses at baseline (A1) and following 45 minutes of chronic ICMS (A2) are shown in the top graphs with 113% increase in peak RMS. Evoked response to peripheral electrical stimulation of the wrist at baseline (B1) and following chronic ICMS (B2) are shown in the bottom graphs.

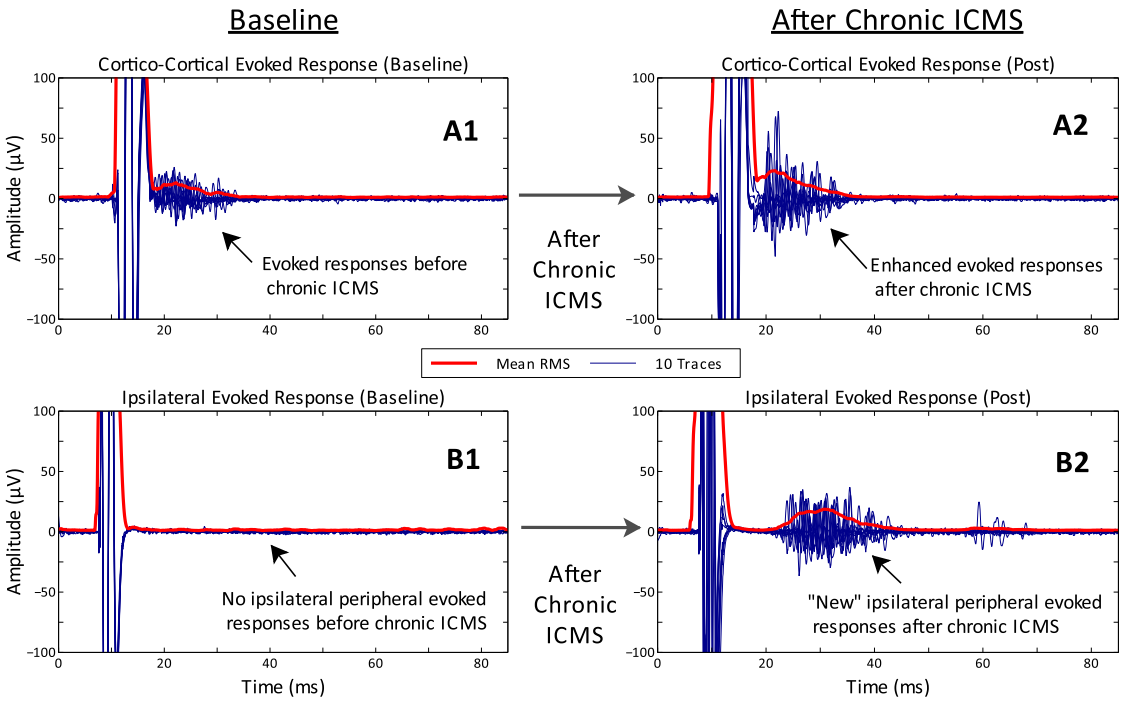

Figure 32. Experiment: JTFB_01. Illustration of enhancement and functional reorganization using the SRD in anesthetized rat. Each graph contains 10 traces (blue) and average instantaneous RMS signal (red). ICMS evoked responses at baseline (A1) and following 30 minutes of chronic ICMS (A2) are shown in the top graphs with an 80% increase in peak RMS. Evoked response to peripheral electrical stimulation of the wrist at baseline (B1) and following chronic ICMS (B2) are shown in the bottom graphs.

4.3 Discussion

Successful enhancement and functional reorganization were observe in 2 of 3 animals. The absence of enhancement or functional organization in the other animal could be attributed to differences in surgery success. During the BCI_Test_6 experiment cortical tissue was damaged prior to starting chronic ICMS. We were still able to evoke corticocortical evoked responses using ICMS and decided to proceed with chronic stimulation, but latencies were greater (20 ms) compared to the expected 7-10 ms. Three 30 minute sessions of chronic stimulation were performed with enhancement and functional reorganization assessed after each session. No enhancement or ipsilateral evoked responses were observed. Although we could evoke a response with ICMS, the non-typical latencies likely point to some cortical connectivity alterations resulting from the damaged cortex. The lack of enhancement was thus contributed to this damage.

Results from previous studies in anesthetized animals using rack mounted stimulation and recording system show that ICMS delivered in 2 out of 10 animals did not lead to enhancement [179]. Thus we assume that enhancement and functional reorganization may not be produced in all animals. The SRD was able to enhance interhemispheric pathways leading to functional reorganization in 2 of 3 animals or 66.6%. SRD system specific causes in the absence of cortical enhancement and ipsilateral responsiveness were ruled out with confirmatory recordings using the rack system.

Our results, using the SRD in anesthetized rats were similar to previous findings from rack mounted equipment [179]. For example, ipsilateral evoked response latencies following ipsilateral forelimb stimulation were comparable using the SRD (15-16 ms) and rack system (17.14 ± 1.95 ms). Furthermore, ipsilateral forelimb stimulation current

used to produce ipsilateral evoked responses by the SRD (100-200 µA) were comparable to stimulus currents required in the rack system experiments (215.91 ± 100.27 µA).

The last consideration was the ICMS amplitude used during chronic ICMS. Current amplitudes required for chronic ICMS (1.5 x threshold) using the SRD were 30 µA for all animals while amplitudes required with the rack system were 42.73 ± 15.55 µA. Not only were stimulation currents required for ICMS lower with the SRD, but biphasic stimulation may produce less tissue damage at the electrode tissue interface compared to cathodic only stimulation. In general, when current is delivered to cortical tissue using typical metal microelectrodes, there are faradaic and non-faradaic reactions occurring. The fundamental process that occurs at the electrode-tissue interface is a transfer of charge carriers from electrons in the metal electrode to ions in the electrolyte [180–182]. Recall that biphasic current waveforms are comprised of both a cathodic (negative) and an anodic (positive) current phase. In both the biphasic and monophasic waveforms the cathodic phase is used to elicit a desired physiological effect such as activation of cortical action potentials in our case. However, with the biphasic waveform the second phase is a reversal phase of anodic current that greatly increases the likelihood that reversible reactions at the electrode-tissue interface will be returned to pre-stimulus states. Following the monophasic stimulus the electrode potential remains relatively negative during the inter stimulus interval. During this time faradaic reactions can continue leading to reduction of oxygen and formation of reactive oxygen species implicated in tissue damage [183,184]. Biphasic waveforms immediately return the electrode potential to a value closer to zero as seen with SRD in vivo results (section 0)

resulting in reduced possibility of tissue and electrode damage which is of concern when the SRD is used for longer duration experiments in awake animals.

4.4 Conclusion

In this evaluation we tested the SRD's ability to enhance the interhemispheric pathway between homotopic layer V forelimb representations of SI and whether SRD enhancement lead to functional reorganization in anesthetized animals. The SRD was successful in delivering chronic biphasic ICMS to contralateral SI cortex while simultaneously recording corticocortical evoked responses in the homotopic ipsilateral SI cortex of anesthetized animals. In two of three experiments the SRD was successful in enhancing the interhemispheric pathway which was measured by means of increased peak amplitude in the average instantaneous RMS signal. Following the delivery of chronic ICMS from the SRD, ipsilateral responsiveness was observed whereby cortical neurons in the ipsilateral forelimb cortex became responsive to new input from the ipsilateral forelimb. The SRD was able to capture these ipsilateral responses by successfully recording cortical activity while simultaneously synchronizing with an external stimulator via the SRD's IR sync companion device. Ipsilateral evoked response latencies and stimulation thresholds were comparable to results obtained with previous rack stimulation and recording equipment. In conclusion the SRD was able to produce enhancement and functional reorganization in anesthetized animals using lower ICMS amplitudes and safer biphasic stimulus waveforms compared to the rack system.

5. SRD Implementation: Training Cortical Circuits in Awake Animals

The final goal of this project was to test the hypothesis that chronic stimulation enhances the interhemispheric pathway between SI cortices and leads to functional reorganization in awake rats as seen in anesthetized rats using the SRD system and rack system. Following electrode implantation in SI forelimb cortex, the SRD was attached to awake animals and implemented in a set of in-vivo experiments in which the SRD was used to deliver chronic ICMS to the SI forelimb cortex while simultaneously recording evoked responses in the contralateral forelimb SI cortex.

5.1 Methods

Experiments conformed to The Guide for the Care and Use of Laboratory Animals (NIH publication No. 86-23, revised 1985) and have been approved by the Institutional Animal Care and Use Committee at University of Tennessee Health Science Center.

Pre-implantation Procedures

Sprague Dawley rats (n=6) were induced with isoflurane (5%, 1 L/min O_2, 3-5 minutes) and maintained with isoflurane (1.5-2.5%, 0.2-0.4 L O_2) throughout surgery. Animals were placed in a Narishige stereotaxic apparatus for surgery and electrode implantation. Left and right ear bars of the stereotaxic frame were placed into the auditory meatus. A lubricant was then applied to the eyes, and the head was scrubbed with isopropyl alcohol followed by betadine. Surgical equipment and electrodes were sanitized with 90% isopropyl alcohol and instruments were sterilized in a bead sterilizer.

Pre-implantation Surgery

A local anesthetic (2% Marcaine) was applied around the base of each ear and around the intended incision site. A scalpel was used to create midline incision to expose the dorsal skull and the skin was retracted. Using four small clamps. The exposed bone was scraped to remove any connective tissue, cleaned using hydrogen peroxide and sterile cotton swabs, and dried using sterile gauze. Any bleeding within the exposed tissue or skull was cauterized. The head was leveled within the sagittal plane by positioning both lambda and bregma at equal vertical positions referenced by a wooden probe attached to a microdrive. Markings for electrode implant sites were placed onto the skull over both SI cortices using a fine point marker centered at 0.3 mm posterior and 3.5 mm lateral relative to bregma. A 2-3 mm diameter circular craniotomy or burr hole was performed centered on these marks. The dura mater was left intact unless difficulty with electrode penetration was encountered. Two holes were drilled into the skull posterior to lambda for grounding screws and two holes anterior to bregma for additional anchoring screws. The screws used were stainless steel 303 screws sized 3/32" (#00-90, Antrin Miniature Specialties, Inc., supplied by Amazon Small Parts).

Electrode Implant Procedures

A single chronic platinum/iridium metal microelectrode (FHC, 1 MΩ at 1 kHz) was inserted through the dura and into the cortex at desired stereotaxic coordinates with a Narishige microdrive. The first inserted electrode was used as the recording electrode and inserted ipsilateral to the target forelimb. Desired locations were layer V wrist or forearm representations within SI and at depths of 900-1400 µm. Receptive field(s) of SI neurons were evaluated by audibly monitoring extracellular signals from the electrode while

simultaneously mechanically stimulating the contralateral forelimb skin surface with a small wooden probe. Extracellular signals were amplified using a pre-existing custom amplifier (1500x) and sent to both an audio monitor and oscilloscope. Receptive fields were defined by the area of skin surface that evoked maximum audible cortical responses to minimal mechanical stimulation.

Once a desired receptive field was located the electrode was held in that location for fixation to the skull. A small amount of saline soaked gel foam was placed over the dura for protection. Dental cement was then applied into the craniotomy and onto the electrode shaft. Multiple layers of cement were applied until it reached the top of the electrode's epoxy ball (Figure 33), but not allowed to flow beyond bregma/midline or into the contralateral craniotomy. Once cement had hardened the electrode's friction fit guide tube was retracted using the microdrive, leaving the exposed electrode lead wire and electrode guide post exposed. The guide post was snipped off flush with the dental cement using sharp wire cutters.

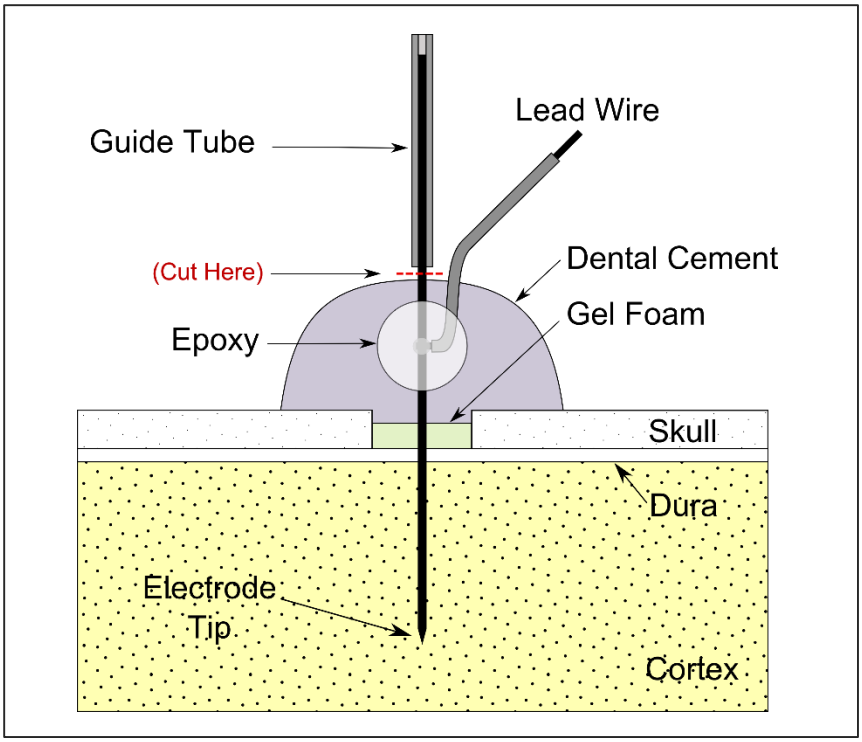

Figure 33. Illustration of chronic electrode implanted into cortex. Electrode is secured to the skull by dental cement. After the dental cement was cured the remaining electrode shaft and guide tube was cut just above the cured cement.

After implanting the recording electrode a stimulating electrode was implanted using the same implant procedures. The stimulating electrode was also a chronic platinum/iridium metal-microelectrode but with lower impedance values to reduce voltage compliance needed during stimulation (FHC, 10 kΩ at 1 kHz). Again, the electrode was inserted into a homotopic representation in layer V forelimb SI cortex of the opposite hemisphere at a depth of 900-1400 µm. This electrode was contralateral to the target forelimb. After confirming homotopic receptive fields but before electrode fixation, ICMS (10-50 µA) was delivered to the stimulating electrode using an A-M Systems Model 2100 stimulator while simultaneously monitoring the recording electrode for cortical evoked responses using the previously mentioned custom amplifier and

oscilloscope. The stimulating electrode was not fixed in place until we confirmed interhemispheric connectivity by evoking responses with ICMS using both the SRD and rack recording and stimulation system. Once confirmed, gel foam and dental cement was used to fix the stimulating electrode as before and leaving only the electrode lead wire. Note: For future reference, the custom amplifier used for mapping and the A-M systems stimulator was used in previously mentioned acute animal experiments and will be referred to as the rack system in the following text.

An electrode interface board (EIB, Figure 15) was then lowered into position just over the implant sites. Electrode lead wires were placed into their appropriate through-holes on the EIB and secured using friction-fit gold plated pins (Neuralynx, Inc.) and excess lead wire was trimmed with wire cutters. A dental cement cap was formed over all screws, lead wires, and EIB. The SRD was then connected to the newly formed headstage using a custom cable. Interhemispheric connectivity was again confirmed by delivering ICMS (10-50 μA) to the stimulating electrode (contralateral cortex) and simultaneously recording evoked responses from the recording electrode (ipsilateral cortex). The anterior and posterior ends of the incision were closed using staples and cleaned.

Post-Operative Care

Immediately following surgery animals were given an antibiotic (i.m., Penicillin G Potassium, 0.05 mL, 12,500 units) and a sedative (i.m., Buprenorphine Hydrochloride, 0.03 mg/kg), and antibiotic ointment was applied around the incision. Animals were monitored until regaining consciousness for rate and ease of respiration and ease of movement. Once the animal began to recover from sedation, interhemispheric connectivity was confirmed a final time using the SRD. Animals were periodically

monitored for 3-7 days for any signs of post-operative complications or signs of distress that included lack of eating or drinking, swelling, and mucous discharge around the implant site.

Chronic Stimulation and Recordings

Following successful SRD attachment, functional validation, and animal recovery, all experimental parameters were sent to the SRD via the GUI. Chronic ICMS (biphasic, 1 ms duration, 1 Hz) was delivered to the contralateral forelimb SI cortex for 0.5-3 hours. Stimulation amplitudes were set to 1.5x threshold values. Cortical enhancement was monitored by continuously collecting evoked responses from the ipsilateral recording electrode at a sampling rate of 15 ksps and sampling duration of 100 ms per ICMS pulse. In some animals, cortical enhancement was evaluated during both awake and lightly anesthetized states. Functional reorganization was examined periodically during chronic ICMS (every 0.5 – 1.0 hours) by lightly anesthetizing the animals with Isoflurane (5% for 2 min, 1.1 % during forelimb stimulation) and applying electrical stimulation to the ipsilateral forelimb while simultaneously recording evoked responses in the ipsilateral forelimb cortex.

Lesions to Mark Recording/Stimulation Sites

Immediately following the final day of experimentation, animals were euthanized by a lethal dose of Nembutal (100 mg/kg, i.p.) and transcardially perfused. Cortices were removed, stored overnight in 4% paraformaldehyde at 4˚ C, and cut in coronal sections (100 µm thicknesses) the following day. Tissue was stained using DAB protocols. Brain sections were then mounted in distilled water onto gelatin-coated glass slides, air dried

overnight, and cover slipped for visual analysis. To gauge problems associated with biocompatibility, infection, and electrode shifting, we processed cortical tissue for histological analysis. We also examined tissue for signs of infection.

Data Analysis

Transcallosal pathway enhancement was defined as a 50% increase in corticocortical evoked response amplitudes and/or 50% increase in peak amplitude of the instantaneous RMS signal within the time window corresponding to corticocortical evoked response activity (7 – 20 ms after the onset of stimulation). Functional reorganization was defined as the presence of evoked responses in ipsilateral forelimb cortex following ipsilateral forelimb peripheral stimulation that was not present prior to enhancement. All measurements were performed in MATLAB. One-way repeated measures analysis of variance (ANOVA) with Tukey post-comparison tests were used to measure statistical significance of 15 consecutive response at differing time points using Prism Graphpad.

5.2 Results

Our dataset is described in Table 6. Electrodes were successfully implanted in wrist representations of four animals, forearm representations of one animal, and a combination of wrist and forearm representations in one animal. An additional four animals were attempted to be implanted but were not because of surgical or mapping complications. The total duration of experiments measured from day of implant to animal euthanasia ranged from 12 to 49 days. Low impedance platinum-iridium electrodes were used for stimulation in all animals and were implanted within cortical layer V at depths

between 900 – 1000 μm (relative to cortical surface). Chronic ICMS amplitudes varied between 30 to 100 μA (1 ms pulse duration, 1 Hz stimulation frequency) while chronic ICMS stimulation duration for a given day ranged between 0.5 - 3 hrs. The electrodes used for recording evolved as the project progressed. Higher impedance tungsten electrodes (2 MΩ) were used in the first experiment. Platinum-iridium (1 MΩ) electrodes and low impedance tungsten (0.8 MΩ) electrodes were used in two and three experiments respectively. Recording electrodes were implanted within cortical layer V at depths between 750 – 1000 μm. Receptive fields of the recording electrodes were the same as that of the stimulating electrode within each experiment.

Table 6. Experiment implant summary data. For each experiment the experiment number and duration of implantation listed in left most columns. Electrode, electrode impedance, receptive field, implant depth, and cortical layer of implantation are listed for both stimulation and recording sites for each experiment. Additionally, stimulation parameters such as ICMS current, pulse duration, stimulation frequency, and ICMS duration per day are listed.

Experiment No.	Implant Duration (days)	Stimulation Site (Contralateral SI Cortex)								Recording Site (Ipsilateral SI Cortex)			
		Electrode and Impedance	Receptive Field	Implant Depth (μm)	Cortical Layer	ICMS Current (μA)	Pulse Duration (ms)	Freq. (Hz)	ICMS Duration per day (hrs)	Electrode and Impedance	Receptive Field	Implant Depth (μm)	Cortical Layer
JTFB_03	12	P/I, 10K	F	1000	V	30-75	1	1	?	Tung, 2M	F	900	V
JTFB_04	19	P/I, 10K	W	1000	V	70	1	1	1-2	P/I, 1M	W	750?	V
JTFB_07	17	P/I, 10K	W	1000	V	50	1	1	0.5-3	P/I, 1M	W	1000	V
JTFB_08	27	P/I, 10K	W	900	V	?	1	1	1-2	Tung, 0.8M	W	900	V
JTFB_09	15	P/I, 10K	W	1000	V	70-100	1	1	1-3	Tung, 0.8M	W	1000	V
JTFB_10	48+	P/I, 10K	W/F	900	V	50	1	1	1-2	Tung, 0.8M	W/F	900	V

Legend: Tung: tungsten, P/I: platinum/iridium, W: wrist, F: forearm

Table 7 shows a chronological summary of the implantation data for each rat. The days of experimentation are indicated with blocks diagonal hatches. Red blocks indicate that corticocortical evoked responses was observed and green blocks indicate that peripheral stimulation from the contralateral forelimb was effective in evoking a contralateral response.

A total of 30 post-implantation days were examined in the 6 implanted rats. Each rat was examined on an average of 5 days post-implantation. On 11 days contralateral peripheral stimulation was not used to test the efficacy of the cells around the stimulation and recording electrodes, but these were confined to the first three implanted rats. On the succeeding three rats contralateral peripheral input was examined on each test day.

Table 7. Daily summary of chronic experiments. Experiment days are indicated blocks with diagonal lines. Colored bocks represent the observance of corticocortical evoked response (red) or contralateral forelimb evoked response (green). Duration of chronic experiments are indicated by the length of white boxes relative to the time scale. Impl = implant.

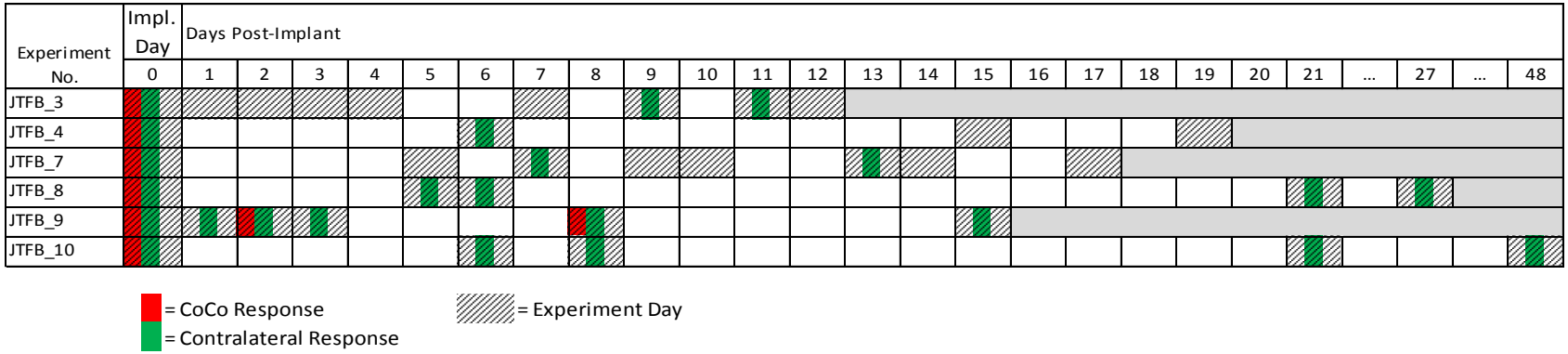

Surgical Implantation Day

Animals were allowed to recover from surgical implantation for a minimum of 24 hours but up to 5 days in some experiments before testing began. Chronic ICMS was delivered to the contralateral SI forelimb cortex for 0.5 - 3 hours on days indicated with blocks with diagonal lines. ICMS consisting of biphasic pulses, 1 ms duration, and 1 Hz was delivered to layer V of the contralateral forelimb SI. Cortical enhancement was monitored by continuously collecting evoked responses. Recording from the ipsilateral electrode was set to a sampling rate of 15 ksps and sampling duration of 100 ms per ICMS pulse. Functional reorganization was examined periodically during chronic ICMS (every 0.5 – 1.0 hours) by lightly anesthetizing the animals with Isoflurane (5% for 2 min, 1.1 % during forelimb stimulation) and applying electrical stimulation through a pair of silver wires to the ipsilateral forepaw while simultaneously recording evoked responses in the ipsilateral forelimb cortex. An example of an animal wearing the SRD system is shown in Figure 34.

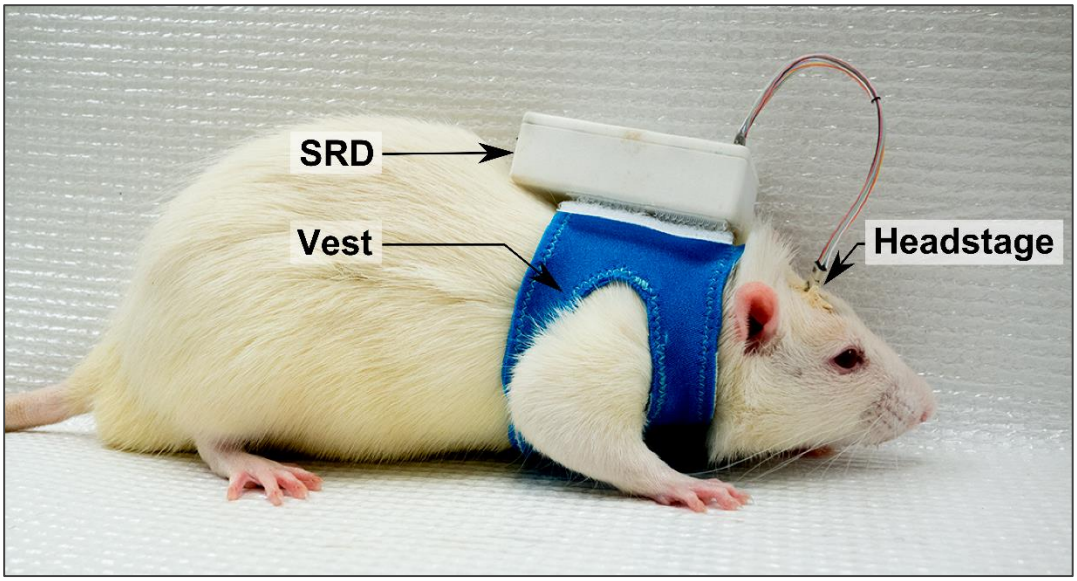

Figure 34. Photograph of rat wearing the SRD system. Rat was wearing a vest by Lomir Biomedical. The SRD was fixed to the vest with Velcro and connected to the electrode interface board using a prototype wire interconnect.

Cortico-Cortical Evoked Responses Day of Implantation

Enhancement of the interhemispheric pathway was examined with chronic ICMS delivered to the contralateral SI in a total of 30 days across the 6 implanted rats. We successively recorded corticocortical evoked response in all implanted animal experiments immediately after implantation, and immediately after animals awoke from anesthesia. Results observed with the SRD were also verified using the lab's existing rack mounted recording and stimulation system. Signal records from the rack system were saved to file using Igor Pro (Wavemetrics). Using both the SRD and rack system we successfully evoked corticocortical responses with ICMS during surgery and immediately following surgery and a result from one rat is shown in Figure 35. In this example six evoked responses to ICMS are shown which are recording using either the rack recording/stimulation system or SRD systems. Calculated mean instantaneous RMS

signals are also shown and clearly indicate an increase in signal power within the time window (7-20 ms post stimulus) associated with corticocortical evoked response latency. Thus, results from the rack system corroborated corticocortical evoked response results seen using the SRD system during the day of implantation.

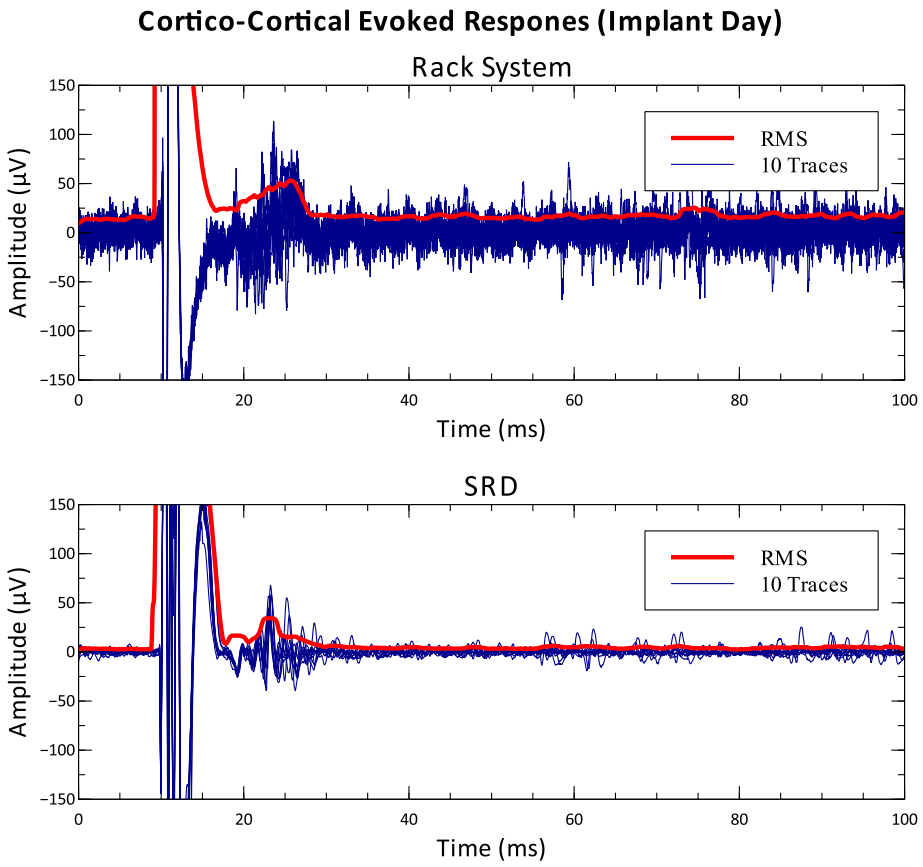

Figure 35. Corticocortical evoked responses to ICMS post-implant. Following implant of electrodes both the rack recording/stimulation system (top) and the SRD (bottom) are able to evoke cortical responses with ICMS (40 µA). Each plot shows 6 traces (blue) and the mean instantaneous RMS signal (red).

Post Implantation Days

In spite of being able to evoke corticocortical responses with ICMS at the day of implantation, we were only able to evoke responses in one rat (JTFB9) during two of the post-implantation experiments. Interestingly, corticocortical responses were only evoked during the initial period of stimulation on the first instance and only at higher ICMS amplitudes for the second instances of cortical response. However, we could not produce cortical enhancement nor did we produce functional reorganization whereby ipsilateral forelimb cortex becomes responsive to input from the ipsilateral forelimb.

The first instance of evoking corticocortical responses with ICMS occurred at two days post-implantation. Initial efforts to evoke corticocortical response failed using ICMS currents up to 70 µA. One hour of chronic ICMS (70 µA) was started despite not being able to evoke any responses. At no time during this initial chronic stimulation session were we able to evoke response. We subsequently increased the ICMS amplitude to 250 µA and succeeded at evoking corticocortical response. A stimulation threshold was then determined to be approximately 45 µA. Again using 70 µA (≈1.5x threshold), two 30-minute sessions (S1 and S2) of chronic stimulation were completed. Enhancement was evaluated before chronic ICMS (0 min), at 15 minutes post ICMS (15 min), and at the end of ICMS (30 min) for each session of stimulation. Functional reorganization was checked by stimulation the ipsilateral forepaw at the end of each stimulation session stimulation.

We were unable to evoke any response to ipsilateral forelimb stimulation. Corticocortical evoked response (Figure 36(A)) were produced during these two chronic ICMS sessions, but peak-to-peak response amplitudes (Figure 36(B)), peak instantaneous

RMS amplitudes (Figure 36(C)), and occurrence of responses lessened with time. There were no measureable evoked responses compared to background activity by the end of S2. Cortical evoked responses were not enhanced, but reduced with time ($\alpha < 0.001$) ranging from 64.7±18.0 μV at the start of ICMS (S1 - 0 min) to 24.8±7.2 μV at the end of the second ICMS session (S2 – 30 min). Similar, peak instantaneous RMS signals were not enhanced, but reduced ($\alpha < 0.001$) with time ranging from 29.4±7.9 μV at the start of S1 to 13.3±3.7 μV at the end of S2.

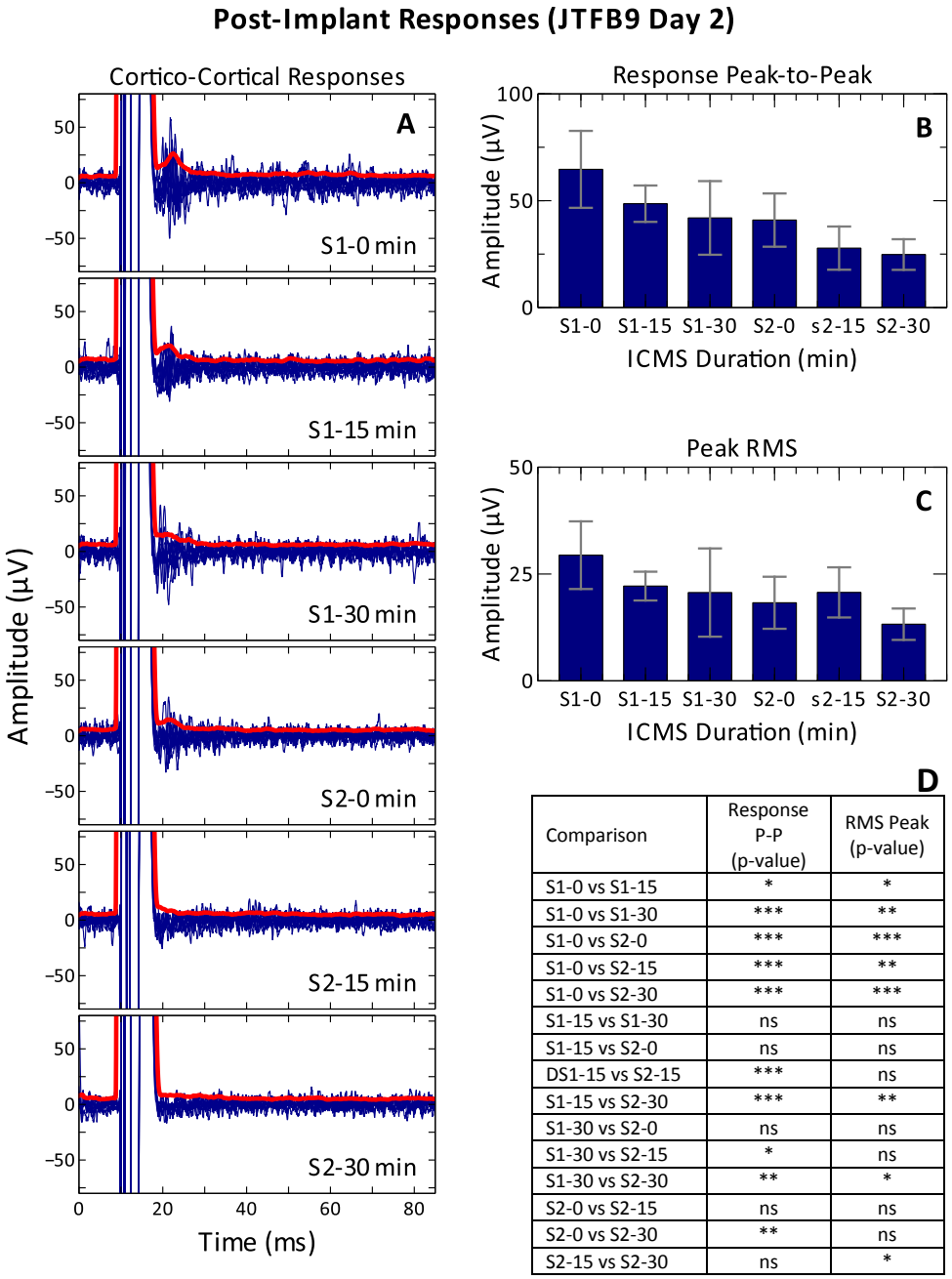

D

Comparison	Response P-P (p-value)	RMS Peak (p-value)
S1-0 vs S1-15	*	*
S1-0 vs S1-30	***	**
S1-0 vs S2-0	***	***
S1-0 vs S2-15	***	**
S1-0 vs S2-30	***	***
S1-15 vs S1-30	ns	ns
S1-15 vs S2-0	ns	ns
DS1-15 vs S2-15	***	ns
S1-15 vs S2-30	***	**
S1-30 vs S2-0	ns	ns
S1-30 vs S2-15	*	ns
S1-30 vs S2-30	**	*
S2-0 vs S2-15	ns	ns
S2-0 vs S2-30	**	ns
S2-15 vs S2-30	ns	*

Figure 36. Corticocortical exception post-implant day 2: Corticocortical evoked responses to ICMS in JTFB9 at 2 day post implantation. (A) Each of the six rows of traces represents corticocortical evoked response seen during two 30-minute sessions (S1 and S2) of chronic ICMS (70 µA). Fifteen minutes was used after S1 to check for ipsilateral responses. Each plot shows 10 traces (blue) and the mean instantaneous RMS signal (red). (B) Peak to peak signal amplitudes for each time point are shown with error bars representing one standard deviation. (C) Instantaneous RMS (not mean) peaks for each time point are shown with error bars representing one standard deviation. (D) Results of multiple comparison test for both the response peak-to-peak and RMS peak. * ($p < 0.05$), ** ($p < 0.01$), *** ($p < 0.001$), ns ($p > 0.05$).

The second instance of evoking corticocortical responses with ICMS occurred at eight days post-implantation for subject JTFB9. Stimulation threshold was determined to be approximately 65 µA. Two 60-minute sessions (S1 and S2) of chronic stimulation were completed each using 100 µA (≈1.5x threshold) ICMS. Enhancement was evaluated before chronic ICMS (0 min), at 30 minutes post ICMS (30 min), and at the end of ICMS (60 min) for each session of stimulation. Functional reorganization was checked by stimulating the ipsilateral forepaw at the end of each stimulation session.

Corticocortical evoked response (Figure 37(A)) were produced throughout both chronic ICMS sessions. Peak-to-peak response amplitudes (Figure 37(B)), peak instantaneous RMS amplitudes (Figure 37(C)), and occurrence of responses remained steady with time. However, we were unable to evoke any response to ipsilateral forelimb stimulation. Cortical evoked responses were not statistically different ($\alpha = 0.175$) across either stimulation sessions. Corticocortical evoked responses ranged from 59.8±21.3 µV at the start of ICMS (S1 - 0 min) to 53.2±15.6 µV at the end of the second ICMS session (S2 – 60 min). Similar, peak instantaneous RMS signals were not statistically different across sessions ($\alpha = 0.100$) ranging from 21.1±8.0 µV at the start of S1 to 20.3±4.1 µV at the end of S2.

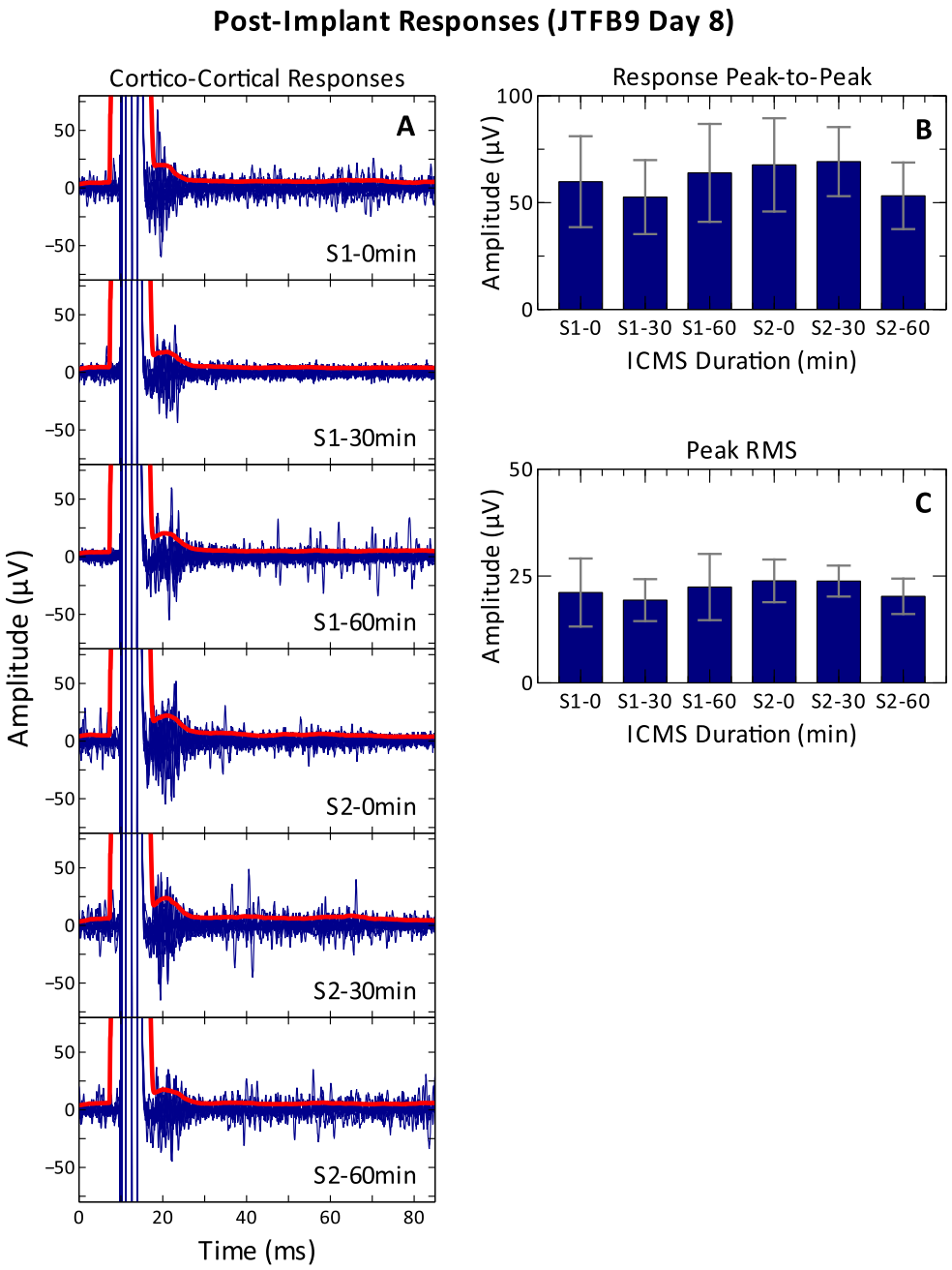

Figure 37. Corticocortical exception post-implant day 8: Corticocortical evoked responses to ICMS in JTFB9 at 8 day post implantation. (A) Each of the six rows of traces represents corticocortical evoked response seen during two 60-minute sessions (S1 and S2) of chronic ICMS (100 µA). Fifteen minutes was used after S1 to check for ipsilateral responses. Each plot shows 10 traces (blue) and the mean instantaneous RMS signal (red). (B) Peak to peak signal amplitudes for each time point are shown with error bars representing one standard deviation. (C) Instantaneous RMS (not mean) peaks for each time point are shown with error bars representing one standard deviation.

Contralateral Forelimb Evoked Responses

Although we were not able to observe corticocortical evoked responses in almost all days following implantation, we were able to verify the presence of contralateral forelimb input (18 times) by observing and/or recording evoked responses to respective contralateral forelimb stimulation for both implanted electrodes (Table 7, green boxes). Furthermore, post-recovery receptive fields were found to be comparable to pre-implant receptive fields. Figure 38 shows 10 consecutive contralateral forelimb evoked responses (blue) recorded with both systems and shows the mean instantaneous RMS signal computed for those 10 evoked responses (red) in one animal. Traces recorded from the rack system are displayed in the top row of Figure 38(A1-A2) while traces recorded with the SRD system are displayed in the bottom row of Figure 38(B1-B2). Contralateral evoked responses are shown for both the implanted recording electrode (A1 and B1) and the implanted stimulating electrode (A2 and B2). Evoked responses can clearly be seen in both the recorded traces and mean RMS signal following the stimulus artifact of each electrode. This result was observed using both the SRD and rack system. These results suggest that the electrodes remained within the cortical volume responsive to forelimb representations similar to that observed during electrode implantation.

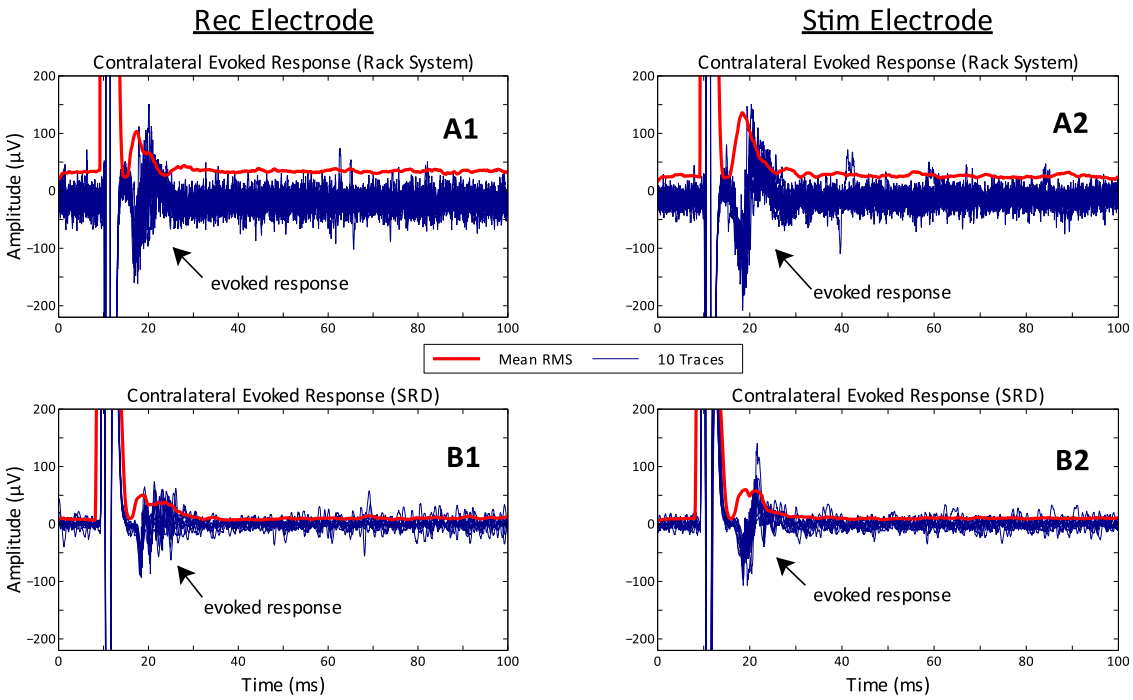

Figure 38. Contralateral evoked response post recovery in one animal. Following recovery (3 wks) both the tethered system Igor (top) and the SRD (bottom) are able to recorded evoked responses to contralateral peripheral forelimb stimulation (100 µA). Each plot shows 10 stacked traces (blue) and the mean instantaneous RMS signal (red) using a 2 ms window.

Stimulation and Recording Sites in SI

During time of implantation both stimulation and recording electrodes were targeted to a depth between 900 – 1000 µm that corresponded to layer V. An example of the location of stimulating and recording sites is shown in Figure 39. Prior to euthanasia, lesions at both the recording site and stimulating site were produces by delivering 5-7 µA of direct current to the electrodes for 7 - 10 s. Lesions are highlighted by colored circles and indicate where the active electrode sites were located within the cortex.

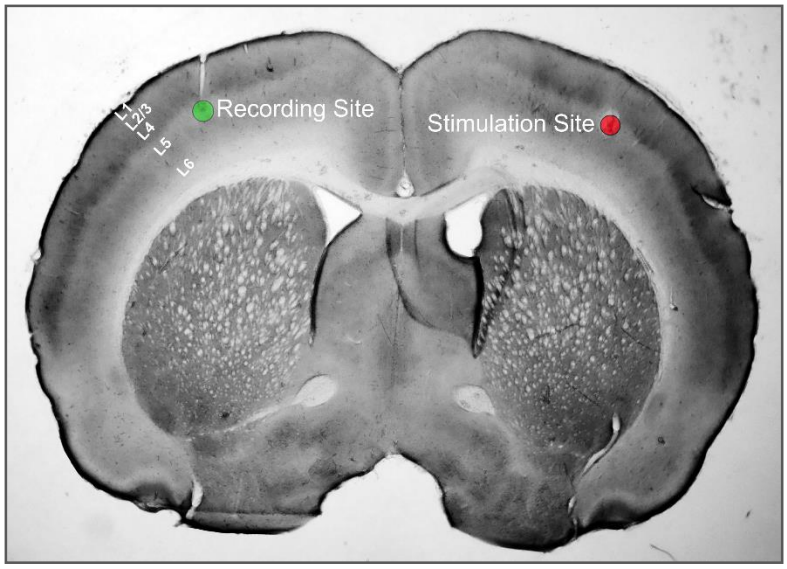

Figure 39. Example photomicrograph of coronal slice showing lesions made at stimulation and recording electrode locations. Lesions indicate recording (green circle) and stimulation (red circle) locations within the cortex. Both the recording and stimulation electrode were located in layer V and are highlighted above with colored circles. Cortical layers are labeled L1-L5. (Subject: JTFB_09)

Effects of Chronic ICMS

The effect of chronic ICMS on brain tissue and stimulating electrode was examined. First, the cortex of two implanted animals were not lesioned before sacrifice in efforts to visualize any gross tissue damage caused by multiple days of chronic stimulation. Tissue damage was defined as the appearance of lesion-like staining around the active site of the stimulating electrode similar to that of direct current lesioning. Figure 40 shows an example photomicrograph (100 µm coronal slice) from an animal that received no direct current lesion prior to sacrifice (control) and stained using DAB. Based on the photomicrographs, repeated days of chronic ICMS from the SRD did not produce any visible signs of tissue damage in the form of lesioning.

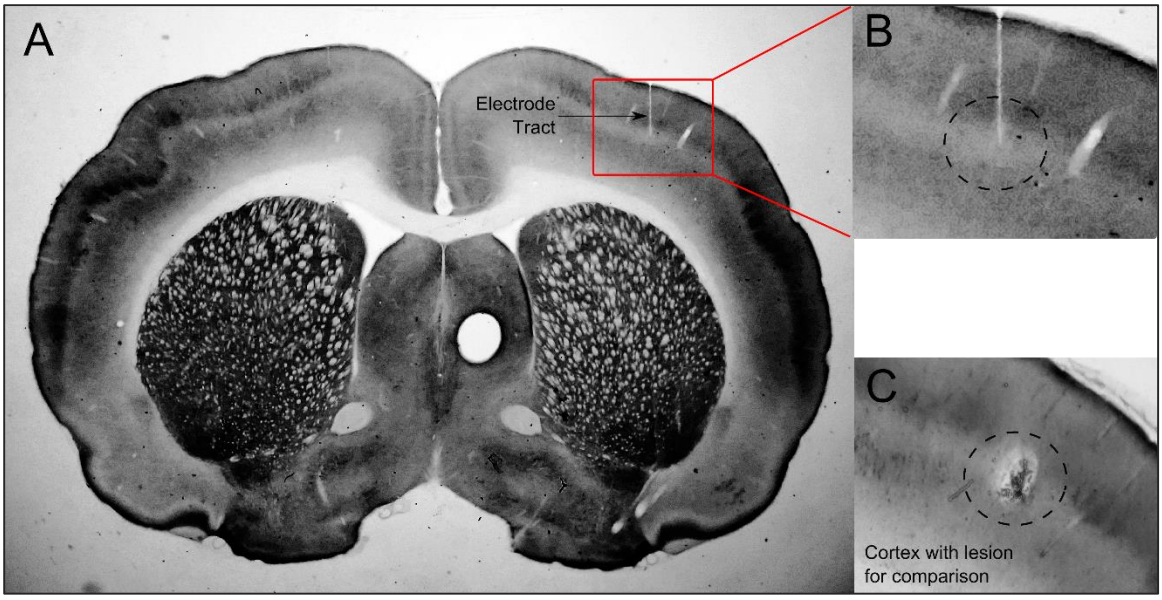

Figure 40. Example photomicrograph of cortical slice in control. Animal was not lesioned at time of perfusion. Both the recording electrode and stimulating electrode were located in layer V. Electrode tract is denoted by the arrow found the whole image (A). The absence of significant DAB staining (B) near the active site of the stimulating electrode indicates that repeated episodes of chronic ICMS did not significantly damage the cortical tissue. For comparison (C) shows a close-up of DAB stained cortical section after lesion produced with 10 nA for 5 seconds.

The goal of the second stimulation related analysis was to compare stimulating electrode impedance prior to and after chronic ICMS. The preferred method of in vivo impedance measurement is to measure impedance at 1 kHz. However, we did not possess the instrumentation to perform a 1 kHz in vivo impedance measurement. A compromise was made by capturing both the current and voltage waveforms (similar to Figure 27) during ICMS at time of implantation and post-recovery and subsequently computing a maximum impedance value using Ohm's law (V=IR). Results showed that stimulation waveforms remained accurate in timing and amplitude pre-implant and after chronic ICMS. Maximum impedance values for the stimulating electrode did not differ (α=0.53) pre-implant (30.7 ± 5.5 kΩ) verses after chronic ICMS (31.3 ± 7.0 kΩ).

5.3 Discussion

The SRD was used to deliver intracortical microstimulation to interhemispheric connections between homotopic forelimb representations and to test the hypothesis that chronic intracortical microstimulation enhances the interhemispheric pathway between homotopic SI cortices and leads to functional reorganization in awake rats. Electrodes were implanted into layer V of homotopic wrist or forearm representations within each hemisphere. During each day of experimentation, following recovery, ICMS was delivered for up to 3 hours to the contralateral forelimb SI while simultaneously monitoring for corticocortical evoked responses in the opposite SI. Functional reorganization of the ipsilateral forelimb cortex was examined by lightly anesthetizing the animal and inspecting cortical signals for responses to ipsilateral forelimb stimulation. Findings from these experiments showed that the SRD could record evoked responses to ICMS immediately before and after electrode implantation. The SRD could also record both spontaneous and contralateral forelimb evoked responses throughout survival (3-7 weeks) for both the stimulating and recording electrodes. However, the SRD nor the previously tested rack system was able to produce corticocortical evoked responses, interhemispheric pathway enhancement, or functional reorganization of the ipsilateral SI cortex after as little as 24 hours post-surgery.

The primary reason for non-enhancement and lack of functional reorganization was likely due to inability to activate the interhemispheric pathway in days following implantation of electrodes. Causes of this inability can be classified into difficulties with either the SRD system, electrodes, or physiological changes. Each of these points will be discussed below.

SRD

In response to the first point, testing in awake animals demonstrated that the SRD functioned as designed and was both recording and performing similarly as observed in the anesthetized experiments. Supporting evidence of a properly functioning recording subsystem included the facts that during each post-surgical day of experimentation we successfully recorded spontaneous cellular activity in the form of spikes and bursting activity and when tested we recorded contralateral forelimb evoked potentials from each implanted electrode (Figure 35 and Figure 38). Proper functionality of the stimulation subsystem was verified by measuring the current output of the SRD while simultaneously measuring the voltage drop across the tissue-electrode load (not shown). All instances in which stimulator functionality was tested the stimulator produced accurate current waveforms and similar voltage waveforms post-recovery compared to pre-implant, though this was not checked in all animals. In addition to verifying proper recording and stimulating functionality, all results seen while using the SRD were validated using the rack system including the ability to record contralateral forelimb evoked responses (Figure 38) and inability to evoke corticocortical response using ICMS. These results make it less likely that the SRD was responsible for the absence of corticocortical response.

State of the Animal

If the SRD functioned in a similar way as the rack system and similar to itself during the anesthetized experiments (Chapter 4) then differences between awake animal tests and acute anesthetized animal experiments exist not with the SRD but elsewhere. One difference between these experiments and the acute anesthetized experiments was

the anesthesia. We tested the effects of anesthesia on both the SRD's and rack system's ability to evoke corticocortical responses with ICMS while the animals were either awake, lightly anesthetizing with isoflurane (0.8 – 1.25%), or with comparable doses of ketamine/xylazine used in previous experiments [99]. Both systems' inability to evoke corticocortical responses post-recovery remained and did not differ between types of anesthesia, concentrations of anesthesia, nor absence of anesthesia. The presence of anesthesia made no difference either system's ability to produce responses with ICMS post-recovery.

Electrode Issues

Other reasons of the inability to evoke corticocortical responses using ICMS are issues related to electrodes or changes to the cortical tissue in response to the electrode implants. One initial theory was that inflammatory processes or even infection caused by the implanting of electrodes were affecting the surrounding neurons. However, after progressing further with data collection we believe that inflammation or infection were not significantly effecting our ability to record local cellular activity. The fact that we could record normal spontaneous cortical activity each day of post-surgical experimentation (24 hrs. to 7+ wks.) and record evoked responses to contralateral forelimb stimulation for each electrode was again useful. If inflammation or infection were causing significant changes to the local cellular activity then we would expect to observe a lack of spontaneous activity and possibly an absence of contralateral forelimb evoked responses which was not the case. Also, no evidence of infection at time of euthanasia were observed within the histological tissue staining results (Figure 39). At more than 3 weeks any symptoms of inflammation or infection should be absent in rats

and particular so rats receiving antibiotics such as the ones in this study. Yet we were unable to use ICMS to evoke corticocortical responses, produce enhancement, or produce functional reorganization at up to 7 weeks post-implantation. There remains an unexplained phenomenon causing a difference between pre-recovery results and post-recovery results.

Electrode Relocation

Another possible cause of differences between pre and post recovery results may relate to relative movements between the active site of the electrode and its target tissue volume. Recall that the electrodes were fixed to the skull with dental cement and thus were fixed relative to the skull. If the brain swells, or in some way shifts, the relative electrode-tissue position could change. Based on the visible lesions (see example in Figure 39) we have shown that the active electrode sites at time of sacrifice were within the desired layer V. In addition, we also have shown that both systems could observe/record contralateral forelimb evoked responses, and we confirmed receptive fields of several animals during post-recovery experiments and found that receptive fields were similar to that found during the original mapping at surgery. All of these facts indicate that the active site of both the stimulating and recording electrodes remained at the correct depth and within the volume of tissue representing pre-implant forelimb representations. Thus, the reason for no corticocortical evoked response was not related to electrode/tissue movements. Furthermore, corticocortical responses were not observed even when ICMS amplitude was increased which should have allowed current spread to neighboring cortical sites in layer V if the electrode had indeed shifted. A summary of results and interpretations that were discussed above are shown in Table 8.

Table 8. Summary of test results from awake animal experiments and interpretations.

Result	Interpretation
SRD and racked system can produce and record evoked responses to ICMS immediately before and after implant.	SRD was functioning properly and comparable to the rack system. Electrodes are in the proper location.
SRD and rack system can record cortical activity throughout animal survival.	SRD was functioning properly; cells remain viable; no severe glial scaring encapsulating the electrode occurred.
Contralateral evoked responses were observed on both electrodes throughout survival.	Cells in both stimulation and recording sites remained viable and electrode location has not significantly shifted.
Lesions in tissue were located in layer V.	Electrodes remained in desired cortical layer after implant and indicate no gross movement.
Receptive fields post-recovery were similar to that of pre-recovery receptive fields.	Electrodes remained in desired cortical volume after implant and indicate no gross movement.
Repeated episodes of chronic stimulation produced no visible lesions in cortex seen by DAB staining of non-lesioned cortical slices.	Chronic ICMS did not produce visible damage to the surrounding cortical tissue.
Compliance voltage of SRD stimulation remains within specification and similar in amplitude to baseline.	No significant changes in electrode impedance indicating that the electrode and/or the tissue interface did not significantly change.

Experimental Technical Considerations

To date there has been no strong indication of why the SRD was unable to produce corticocortical evoked response with ICMS, enhancement, nor functional reorganization post-recovery in awake and lightly anesthetized animals. Neither is there strong indications of why comparative testing for corticocortical evoked response using the rack system also resulted in the absence of evoked responses. Therefore, it is important to suggest experimental variations to improve results for future experiments. The results suggest that electrode/tissue position do not undergo any large movements; however, having the ability to adjust the electrode depths could add useful information. Installing a wearable microdrive system would provide this ability. Commercially available wearable microdrive systems include the EDDS Microdrive System by

Microprobes and the Nano-Drive by Cambridge NeuroTech. One could implant both electrodes at a shallow depth and allow time for recovery. Following recovery the electrodes could then be lowered to the desired cortical depth and ICMS delivered to forelimb SI while recording in the opposite SI cortex. Stice and Muthuswamy gave evidence that brain implants which are moved post-implantation can reduce levels of gliosis around the electrode tip [185]. This modification could answer the question as to whether the chronic presence of the electrode in some way modulates the results seen post-recovery vs pre-recovery. Another option possible with the addition of the microdrive would be to independently drive the electrodes post-recovery for fine tuning their position. Even though we showed that the electrodes remain within layer V, perhaps the electrodes have shifted to more shallow depths within layer V and are no longer able to evoke interhemispheric activity. A wearable microdrive could provide information as to whether recording/stimulating at different depths in layer V post-recovery makes a difference.

Another suggested experimental modification would be performing more thorough histological testing to quantify possible gliosis and/or to quantify changes in neural density or viability in response to electrode implants. DAB staining procedures in this project did not provide any cell-type specific methods of quantification. Therefore, there were no distinctions made between neurons and cell types associated with scar tissue formation in the brain such as microglia and astrocytes [186]. Neuronal cell viability could be studied with immunohistochemistry by quantifying the presence of neuronal nuclei (NeuN) antibody [187–189]. Neuronal death has been shown to affect excitation thresholds leading to the need for higher stimulation values or the loss of the

ability to produce activation [190]. Similarly, glial scar formation or gliosis around the electrode could be studied by using immunohistochemistry for glial fibrillary acidic protein (GFAP) to quantify astrocytes [191] and CD68 (ED1) to quantify microglia [192,193]. Activated microglia and astrocytes are the primary cell types associated in gliosis of chronically implanted electrodes within the brain [186,188,194–199].

A second step in providing a more thorough scar tissue analysis would be to monitor for changes in total impedance of the electrode-tissue load. Others have suggested that the gliosis leads to an increasze in measured impedance [200] and reduction in recorded neuronal spike amplitudes [189]. Although we saw no significant change in our simplified impedance measurement, a more standardized method of impedance measurement would be to deliver a small sinusoidal current waveform and measure the corresponding peak-to-peak voltage drop across the load. The RHD2000 series chip used by the SRD for recording has such a feature and will be discussed later. Enabling this feature would allow for in vivo monitoring of total impedance throughout animal survival.

Modifications in stimulation parameters could also provide useful information. There is some thought that using a short train of pulses would be more efficacious at evoking responses compared to single pulses. However, we did try using several very long trains (20 second duration, 200 Hz) of pulses to produce enhancement in one rat, but were unsuccessful at producing evoked corticocortical evoked response before or after several trains of ICMS stimulation. It is not clear as to whether modifying the stimulation parameters alone would provide any different results.

5.4 Conclusion

We anticipated that, in awake animals, chronic microstimulation using the SRD would enhance interhemispheric connections between homotopic forelimb representations in SI and that the enhancement would bring about functional reorganization similar to that seen in anesthetized animals. However, we were unable to produce enhancement in chronically implanted animals nor show any form of functional reorganization. The implementation of additional and/or modified experimental procedures could highlight sources of discrepancies with previous acute results within anesthetized animals compared to results found in awake animals post-recovery in this experiment. Despite the SRD's inability to produce enhancement or functional reorganization in awake animals, results show that the SRD did function as designed and functioned comparable to the rack recording and stimulation system of which it was designed to replace.

6. Project Summary

6.1 Project Review

We described for the first time the design, implementation, and testing of a telemetry controlled simultaneous stimulation and recording device (SRD) to deliver chronic intracortical microstimulation (ICMS) to physiologically identified sites in rat somatosensory cortex (SI) and test hypotheses that chronic ICMS strengthens interhemispheric pathways and leads to functional reorganization in the enhanced cortex. Specific goals of this project were to (1) design a wireless simultaneous stimulation-and-recording device to train cortical circuits in rat primary somatosensory cortex, (2) evaluate the SRD on the bench and in vivo, (3) evaluate the SRD's ability to chronically

deliver ICMS in anesthetized animals, and (4) implement the SRD to deliver chronic ICMS in awake animals.

We have created a $500 open-source, wireless brain-computer interface system that was capable of simultaneous stimulation and recording in rat cortex in awake rats. All components used to build the SRD were commercial-off-the-shelf (COTS) components. Biopotential signals from biological tissue were amplified, filtered, and digitized by an integrated digital electrophysiology interface chip. Digitized data were transferred via SPI communication to a core processor, where data was then buffered and transmitted to a host PC via Bluetooth for visualization and offline analysis. Bluetooth communication was also used to send stimulation, recording, calibration, and filter settings to the SRD from a GUI. The SRD was capable of simultaneously recording from two channels at a maximum sample rate of 15 ksps\channel. Users have the ability to select any two channels from 12 available channels, or have the system sweep through all channels two at a time. Biological tissue stimulation was delivered using an adjustable constant current stimulator capable of delivering ±255 μA of current with a compliance voltage up to ±10 volts. The battery and SRD PCB was housed in a custom 3D printed enclosure with magnetically secured top.

The SRD's various subsystems were tested on the bench and in vivo to ensure proper function and to confirm that they met desired system requirements. The SRD consumed an average of 27 mA and could operate about 37 hours on an 850 mAh LiPo battery. SRD stimulator successfully produced accurate monophasic, biphasic, and pseudophasic current waveforms when applied to artificial loads (resistor or saline) on the bench and when applied to platinum/iridium electrodes inserted into the rat cortex.

Noise floor of the SRD recording system was ±5 μV measured with grounded inputs. Bluetooth communication provided a sufficient and reliable connection for desired data transfer rates and two-way communication for setting experimental parameters.

Following bench and in vivo testing we evaluated the SRD's ability to train cortical circuits by delivering chronic ICMS to a physiologically identified region in SI cortex and simultaneously recording evoked responses in a homotopic site in contralateral SI. The goal of this evaluation was to test the hypothesis that chronic ICMS delivered by the SRD enhances the interhemispheric pathway and leads to functional reorganization in anesthetized rats. Results from this evaluation are as follows. The SRD was capable of simultaneously stimulating and recording in rat cortex. The SRD could produce accurate monophasic, biphasic, and pseudophasic constant current stimulation waveforms. The SRD's recorded cortical signals were comparable to the tethered system used in previous experiments. The SRD was able to enhance the interhemispheric pathway through chronic microstimulation (ICMS) in anesthetized rats as shown in figure 4(A2) similar to the tethered system. The SRD was able to show that enhancement of the interhemispheric pathway led to functional reorganization whereby cortical neurons in forelimb cortex responded to new input from the ipsilateral forelimb as shown in figure 4(B2).

Once confident that the SRD functioned as desired in-vivo, we then turned to implementing the SRD in awake rats while the animal wore the SRD during stimulation and recording. Our goal was to enhance the interhemispheric pathway between similar SI forelimb cortices as done in acute anesthetized animals. We also wanted to observe functional reorganization that follows pathway enhancement again as observed in acute

anesthetized animals. Methods were: (1) implant electrodes, (2) animal recovery, (3) attach SRD to vest on animal, (4) provide chronic ICMS stimulation and simultaneously record responses, (5) monitor responses for signs of enhancement, (6) periodically evaluate for functional reorganization by stimulating the ipsilateral forepaw.

Results were corroborated using the previously described rack recording and stimulation system. Results from awake animal implementation are as follows. The SRD and rack system produced and recorded evoked responses to ICMS immediately before and after implant. SRD and rack system successfully recorded cortical activity from the implanted electrodes at various time points throughout animal survival (up to 7 weeks). Contralateral evoked responses were observed on both electrodes throughout survival. Receptive fields post-recovery were similar to that of pre-recovery receptive fields mapped during implantation. Lesions used to mark electrode tip positions within tissue in sacrificed animals were located in layer V. Repeated episodes of chronic stimulation produced no visible lesions in cortex seen by DAB staining of non-lesioned cortical slices. Compliance voltage of SRD stimulation remained within the specifications and similar in amplitude to that seen before chronic ICMS. It was unclear why, following recovery, the SRD or the rack system could not evoke responses with ICMS, enhance the interhemispheric pathway, nor produce functional reorganization in implanted animals. Additional procedures in the experimental protocol such as adjustable depth electrodes and in vivo impedance monitoring could add valuable information as to the cause(s) in discrepancies seen between acute anesthetized experiments and implanted awake animal experiments. However, the evidence shows that the SRD functioned as intended and

comparable to the rack system on which it was based although the goal to produce enhancement and functional reorganization was not achieved.

6.2 Future Directions

Several aspects of the SRD system may be improved and include reducing power consumption, increasing data acquisition throughput, altering the RHD2216 configuration, optimizing the PCB layout, and changing the stimulator design. This section is intended to discuss some of those improvements and changes for future work.

Power Consumption Reductions

Several options exist to further reduce power consumption of the SRD in future revisions of the hardware and firmware. These options include disabling unused portions of the circuit, optimizing the wireless configuration, and optimizing the PSoC's sleep and awake states. Recall that each power domain uses one or more power supply chips to generate required voltages for components. All chips chosen for the SRD's design have enable/disable pins that can be used to enable or disable the chip and any subsequent components that use the power supply chip. Disabling an entire power domain would eliminate virtually any wasted power due to component's quiescent currents. For example, disabling the analog domain when data acquisition is not in use would turn off the Intan RHD2216 and its power supply chip and eliminate any wasted quiescent current used by the linear regulator. However, in the most recent version of the SRD described in this project the enable/disable capabilities are not implemented. To use the enable/disable capabilities the MIC5393 and AS1302 enable pins must be routed and connected to the

PSoC and firmware modifications must be made to allow programmed control of the on/off states.

Power could be further conserved by placing the PSoC into lower power operating modes, such as sleep mode, more often than what is currently implemented in the firmware. The existing implementation only sleeps the PSoC between stimulation epochs. If the stimulation and data transmission terminate before the next stimulation event or cycle, then placing the PSoC and other components to sleep would reduce the average power consumption further.

Bluetooth can be an extremely low power way to wirelessly send and receive data. However, when data transmission times become long and closer to continuous transmissions, energy savings of BT are non-existent. We do take advantage of some of the RN42's power saving options such as sniff mode. This mode goes into a low power state then periodically wakes to determine if any data needs to be processed. We use a 100 ms sniff mode on both the SRD BT module and the RN42 module plugged into the computer. Further, power savings could be acquired by optimizing the sniff mode times, lowering the transmission power of the module, and completely putting the RN42 into an extremely low power state between transmissions. To implement all these changes care must be taken to ensure the RN42 could wake quick enough to transmit when needed. Attempts were made to use the very low power modes between transmissions, but were eventually abandoned due to difficulty waking the device remotely to receive experimental parameter updates.

Data Acquisition Throughput

The current SRD system allows two simultaneous channels of data acquisition. This limitation is defined by limits in data transmission speeds, transmission power requirements, CPU speed, and data buffer size. Increasing any of these would allow increased ability to record from more channels simultaneously.

Much time and effort went into choosing a wireless solution, and during most of the system design stage the RN42 was the best fit for the design when considering power, size, and ease of use. An updated search for available wireless modules resulted in finding the AMW004 (Wallaby) WiFi module (ACKme Networks), which states power consumption almost 3 times less than that of the RN42 even at 1 Mbps. The datasheet states that the current consumption during active receive mode is 6.9 mA and during active transmit mode is 12.5 mA using 1 Mbps UDP. The AMW004 also has UART, SPI, I2C, and USB interface to allow faster throughput between chip and wireless module. Not only could this allow lower SRD operating power, but potentially increase the transmission bandwidth to a point of allowing much more than 2 simultaneous recording channels without the need to buffer large amounts of data.

The SRD uses a Cypress PSoC 3 as its CPU. This chip is sufficient for the current intended application, however if one needs more data throughput or processing power then the easiest option may be to replace the PSoC 3 with a PSoC 5 Low Power (LP) chip. PSoC5 LP comes in a 68 pin QFN footprint that matches the SRD's PCB layout. The power pins and GPIO pins are located at the same pins. The processing core of the 5LP has considerably more processing power with 80 MHz 32bit ARM Cortex M3 verses the PSoC3's 67 MHz 8bit 8051 core. The 5LP also has more memory for data buffering

and firmware code with 256 KB Flash and 64 KB SRAM verses the PSoC3's 64 KB Flash and 8 KB SRAM. The increased SRAM alone would allow 8 times more signal data buffering if using the same buffering scheme. That would allow 16 channels to be simultaneously buffered instead of 2. However, the biggest drawbacks to using the PSoC 5LP would be a potential increase in power usage (depends on implementation) and the time required to port firmware code to a different processor. Cypress allegedly makes this process easy with some conversion tools and the fact that both chips use the same design software with similar high level API function calls. Although there are some differences such as the CPU cores, the programmable analog, programmable digital, programmable routing, pin functions, and other features are quite similar. Furthermore, the PSoC Creator IDE handles many migration issues automatically. Often, migrating a PSoC Creator design is as simple as specifying a new part then rebuilding the project. There is a detail application note about migrating from PSoC 3 to PSoC 5LP (AN77835) on the Cypress website.

Intan RHD2000 Configuration

Improvements to how the Intan RHD2000 series chip is configured on the SRD could improve performance and add additional functionality to the SRD.

Reference electrodes

After performing several tests in vivo while simultaneously recording and stimulating, it was noticed the stimulus artifact could be shortened if using separate points on the animal for reference and stimulation ground return. This was not obvious in initial tests. The SRD's PCB currently uses the RHD2216 bipolar chip in a monopolar

configuration because of lower cost. All negative inputs of the RHD2216 amplifiers are connected to SRD ground, which in turn is the same ground point for the stimulator. An improved PCB configuration would be to connect all the RHD2216's negative inputs to a common point on the animal via a separate reference bone screw in the skull distal to the ground screw. The RHD2216 could also be replaced by the RHD2132 32 channel monopolar version. Again, the reference pin would need to be connected to a separate bone screw. This modification would shorten the stimulation artifact duration seen in the recorded signals.

Fast Settle Function

Due to the potentially long time constant associated with the low cutoff frequency f_L, it may be useful to reset the amplifiers if a large input signal causes the output signals to saturate. Large signal deflections are typical of stimulation artifacts which is inherent in experiments in this project. A feature of the RHD2000 series chip is the ability to quickly return the amplifier to baseline. To settle the amplifiers, the amp fast settle bit in Register 0 is set high momentarily and then returned to zero. The recommended duration of a fast settle pulse is $2.5/f_H$; as the upper bandwidth of the amplifiers is lowered, settling takes more time. Using this guideline, if f_H is set to 10 kHz then setting the amp fast settle bit high for 250 μs, should be sufficient to settle the amplifiers to baseline. A possible implementation scheme for the SRD would be to turn on the fast settle function just before stimulation occurs then promptly turn it off following the end of the stimulation pulse assuming the minimum time has passed using the above criteria. Adding this feature and the reference screw modification could dramatically reduce the stimulus artifact duration.

Impedance measurements

Another feature that could be added to the SRD is the ability to check the impedance of implanted electrodes at any time. The RHD2000 chips have an on-chip AC current waveform generator whose output can be directed to any connected electrode. To implement this feature the PSoC would send a repeating sequence of digital data to the RHD2000 that represents the desired current waveform. In turn the RHD2000 chip would output the desired current waveform, typically a sinusoidal wave of 1 kHz, while simultaneously sampling the voltage drop at the electrode and sending it back to the PSoC. The impedance would be computed by using the peak-to-peak voltage and peak-to-peak output current and substituting into Ohm's Law (V=IR). Having the ability to measure electrode impedance would allow the user to monitor electrode performance and indirectly tissue status over the course of an experiment which could prove useful in trouble shooting problems with recording signals.

PCB

The SRD's PCB was not made as small as possible due to the smallest battery size used and time constraints. If the battery choice remains, then there may be little gained by reducing the PCB size. However, if a smaller battery is used due to shorter operating time requirements or reduced power consumption, a smaller PCB could prove useful in reducing the overall weight and size of the SRD. There are several physical areas on the PCB that are unpopulated with components (Appendix B) and could be used to optimize PCB size.

Stimulator

An anticipated new product from Intan Technologies could greatly reduce the PCB size, lower the SRD power consumption, and increase the number of stimulation output channels. An Intan Technologies digital electrophysiology interface chip combined with on-chip stimulation capabilities will be commercially available in the near future (personal communication with Intan personnel). With a chip combining both amplifiers, ADC, and stimulation, the SRD's stimulator design and stimulator power supply could be eliminated leading to a significantly smaller PCB. Other than the RN42, the entire bottom side of the SRD PCB is comprised of stimulation components. At this time there are no definite details about the chip specifications other than planned features include multiple stimulation channels and less current consumption than the SRD's present stimulator design.

6.3 Project Conclusion

In this project we described the system development, system testing, and system implementation of a low cost and open-source, wireless simultaneous stimulation-and-recording device (SRD) to modulate cortical circuits in an awake rodent animal model. No such commercial or research system existed that met all our experimental requirements and prompted the design of the SRD. Following design and testing of the system, the SRD produced interhemispheric enhancement that lead to functional changes within forelimb SI of anesthetized rats. We showed that the SRD also functions as designed in awake animal experiments with implanted electrodes despite not being able to produce enhancement or functional reorganization. We are confident that the SRD will

be able to enhance interhemispheric pathways and produce functional reorganization in awake animals with further testing and with possible modifications of experimental procedures. Once we fully validate the SRD in awake animals we will examine how enhancement and functional reorganization persist over a prolonged period of time. We would then be in a position to use the SRD to train cortical circuits in pathological animal models. Possessing the ability to modify cortical circuitry will have important applications in stroke patients and could serve to rescue and/or enhance responsiveness in surviving cells around the stroke region. Also, the ability to induce functional reorganization within the deafferented cortical map, which follows limb amputation, provides a resource for modulating maladaptive cortical reorganization often associated with phantom limb pain thus potentially leading to reduced pain. Finally, features such as the low cost, open-source platform, and wide recording bandwidths make the SRD an attractive system for many electrophysiology research applications.

References

[1] Brodmann K 1909 *Vergleichende Lokalisationslehre des Grosshirninde in Ihren Prinzipien dargestellt auf Grund des Zellenbauen* (Leipzig, Germany: Johann Ambrosius Barth Verlag)

[2] Purves D, Augustine G J, Fitzpatrick D, Hall W C, LaMantia A-S, McNamara J O and White L E 2008 *Neuroscience* (Sunderland, MA: Sinauer Associates, Inc.)

[3] Woolsey T A, Van Der Loos H and Woosley T A 1970 The structural organization of layer IV in the somatosensory region (SI) of mouse cerebral cortex: The description of a cortical field composed of discrete cytoarchitectonic units *Brain Res.* **17** 205–42

[4] Welker C 1976 Receptive fields of barrels in the somatosensory neocortex of the rat. *J. Comp. Neurol.* **166** 173–89

[5] Chapin J K and Lin C S 1984 Mapping the body representation in the SI cortex of anesthetized and awake rats. *J. Comp. Neurol.* **229** 199–213

[6] Waters R S, McCandlish C A and Li C X 1995 Organization and Development of the Forepaw Representation in Forepaw Barrel Subfield in Somatosensory Cortex in Rat *Cerebral Cortex: The Barrel Cortex of Rodents* (in Cerebral Cortex, vol. 103, no. 2, E. G. Jones and I. T. Diamond, Eds. New York: Plenum Press pp. 183-197)

[7] Pearson P P, Oladehin A, Li C X, Johnson E F, Weeden A M, Daniel C H and Waters R S 1996 Relationship between representation of hindpaw and hindpaw barrel subfield (HBS) in layer IV of rat somatosensory cortex. *Neuroreport* **7** 2317–23

[8] Waters R S, Li C X and McCandlish C A 1995 Relationship between the organization of the forepaw barrel subfield and the representation of the forepaw in layer IV of rat somatosensory cortex. *Exp. brain Res.* **103** 183–97

[9] Pearson P P, Li C X and Waters R S 1999 Effects of large-scale limb deafferentation on the morphological and physiological organization of the forepaw barrel subfield (FBS) in somatosensory cortex (SI) in adult and neonatal rats. *Exp. Brain Res.* **128** 315–31

[10] DeFelipe J 2012 The neocortical column *Front. Neuroanat.* **6** 1–2

[11] Lorente de No' R 1933 Studies on the structure of the cerebral cortex I *J. Psychol. Neurol.* **45** 381–438

[12] Mountcastle V 1978 An organizing principle for cerebral function: the unit model and the distributed system *The Mindful Brain* ed G M Edelman and V B Mountcastle (MIT Press) pp 7–50

[13] Nolte J 2009 *The human brain: an introduction to its functional anatomy* (Philadelphia: Mosby Inc. / Elseiver Inc.)

[14] Paxinos G 2014 *The Rat Nervous System* (Academic Press)

[15] Jacquin M F, Woerner D, Szczepanik A M, Riecker V, Mooney R D and Rhoades R W 1986 Structure-function relationships in rat brainstem subnucleus interpolaris. I. Vibrissa primary afferents. *J. Comp. Neurol.* **243** 266–79

[16] Lu S M and Lin R C 1993 Thalamic afferents of the rat barrel cortex: a light- and electron-microscopic study using Phaseolus vulgaris leucoagglutinin as an anterograde tracer. *Somatosens. Mot. Res.* **10** 1–16

[17] Belford G R and Killackey H P 1978 Anatomical correlates of the forelimb in the ventrobasal complex and the cuneate nucleus of the neonatal rat. *Brain Res.* **158** 450–5

[18] Angel A and Clarke K A 1973 Fine somatotopic representation of the forelimb area of the ventrobasal thalamus of the albino rat. *J. Physiol.* **233** 43P – 44P

[19] Francis J T, Xu S and Chapin J K 2008 Proprioceptive and cutaneous representations in the rat ventral posterolateral thalamus. *J. Neurophysiol.* **99** 2291–304

[20] EMMERS R 1965 Organization of the first and the second somesthetic regions (SI and SII) in the rat thalamus *J. Comp. Neurol.* **124** 215–27

[21] Jones E 1985 *The Thalamus* (New York: Plenum Press)

[22] Jensen K F and Killackey H P 1987 Terminal arbors of axons projecting to the somatosensory cortex of the adult rat. II. The altered morphology of thalamocortical afferents following neonatal infraorbital nerve cut. *J. Neurosci.* **7** 3544–53

[23] Arnold P, Li C and Waters R 2001 Thalamocortical arbors extend beyond single cortical barrels: an in vivo intracellular tracing study in rat *Exp. brain Res.* **136** 152–68

[24] Li H and Crair M C 2011 How do barrels form in somatosensory cortex? *Ann. N. Y. Acad. Sci.* **1225** 119–29

[25] Chapin J K, Sadeq M and Guise J L 1987 Corticocortical connections within the primary somatosensory cortex of the rat. *J. Comp. Neurol.* **263** 326–46

[26] Qi G and Feldmeyer D 2010 Cell type-specific excitatory synaptic connections from layer 4 to layer 6A in rat barrel cortex *Acta Physiol.* **198**

[27] Tanaka Y R, Tanaka Y H, Konno M, Fujiyama F, Sonomura T, Okamoto-Furuta K, Kameda H, Hioki H, Furuta T, Nakamura K C and Kaneko T 2011 Local connections of excitatory neurons to corticothalamic neurons in the rat barrel cortex. *J. Neurosci.* **31** 18223–36

[28] Feldmeyer D, Roth A and Sakmann B 2005 Monosynaptic connections between pairs of spiny stellate cells in layer 4 and pyramidal cells in layer 5A indicate that lemniscal and paralemniscal afferent pathways converge in the infragranular somatosensory cortex. *J. Neurosci.* **25** 3423–31

[29] Schubert D, Kötter R, Luhmann H J and Staiger J F 2006 Morphology, electrophysiology and functional input connectivity of pyramidal neurons characterizes a genuine layer va in the primary somatosensory cortex. *Cereb. Cortex* **16** 223–36

[30] Schubert D, Staiger J F, Cho N, Kötter R, Zilles K and Luhmann H J 2001 Layer-specific intracolumnar and transcolumnar functional connectivity of layer V pyramidal cells in rat barrel cortex. *J. Neurosci.* **21** 3580–92

[31] Lübke J, Egger V, Sakmann B and Feldmeyer D 2000 Columnar organization of dendrites and axons of single and synaptically coupled excitatory spiny neurons in layer 4 of the rat barrel cortex. *J. Neurosci.* **20** 5300–11

[32] Mountcastle V B 1957 Modality and topographic properties of single neurons of cat's somatic sensory cortex. *J. Neurophysiol.* **20** 408–34

[33] Mountcastle V B, Davies P W and Berman A L 1957 Response properties of neurons of cat's somatic sensory cortex to peripheral stimuli. *J. Neurophysiol.* **20** 374–407

[34] Innocenti G M, Manzoni T and Spidalieri G 1973 Relevance of the callosal transfer in defining the peripheral reactivity of somesthetic cortical neurones. *Arch. Ital. Biol.* **111** 187–221

[35] Manzoni T, Barbaresi P, Bellardinelli E and Caminiti R 1980 Callosal projections from the two body midlines. *Exp. Brain Res.* **39** 1–9

[36] Manzoni T, Barbaresi P, Conti F and Fabri M 1989 The callosal connections of the primary somatosensory cortex and the neural bases of midline fusion. *Exp. Brain Res.* **76** 251–66

[37] Iwamura Y, Iriki A and Tanaka M 1994 Bilateral hand representation in the postcentral somatosensory cortex. *Nature* **369** 554–6

[38] Taoka M, Toda T and Iwamura Y 1998 Representation of the midline trunk, bilateral arms, and shoulders in the monkey postcentral somatosensory cortex. *Exp. Brain Res.* **123** 315–22

[39] Michael L Lipton, Kai-Ming G Fu, Craig A Branch and Charles E Schroeder 2006 Ipsilateral hand input to area 3b revealed by converging hemodynamic and electrophysiological analyses in macaque monkeys. **26** 180–5

[40] Tommerdahl M, Simons S B, Chiu J S, Favorov O and Whitsel B L 2006 Ipsilateral input modifies the primary somatosensory cortex response to contralateral skin flutter. *J. Neurosci.* **26** 5970–7

[41] Calford M B and Tweedale R 1988 Immediate and chronic changes in responses of somatosensory cortex in adult flying-fox after digit amputation. *Nature* **332** 446–8

[42] Calford M B and Tweedale R 1990 Interhemispheric transfer of plasticity in the cerebral cortex. *Science* **249** 805–7

[43] Pidoux B and Verley R 1979 Projections on the cortical somatic I barrel subfield from ipsilateral vibrissae in adult rodents. *Electroencephalogr. Clin. Neurophysiol.* **46** 715–26

[44] Chapin J and Lin C 1984 Mapping the body representation in the SI cortex of anesthetized and awake rats *J. Comp. Neurol.*

[45] Shuler M G, Krupa D J and Nicolelis M A 2001 Bilateral integration of whisker information in the primary somatosensory cortex of rats. *J. Neurosci.* **21** 5251–61

[46] Pluto C P, Chiaia N L, Rhoades R W and Lane R D 2005 Reducing contralateral SI activity reveals hindlimb receptive fields in the SI forelimb-stump representation of neonatally amputated rats. *J. Neurophysiol.* **94** 1727–32

[47] Angel A and Lemon R N 1975 Sensorimotor cortical representation in the rat and the role of the cortex in the production of sensory myoclonic jerks. *J. Physiol.* **248** 465–88

[48] Yorke C H and Caviness V S 1975 Interhemispheric neocortical connections of the corpus callosum in the normal mouse: a study based on anterograde and retrograde methods. *J. Comp. Neurol.* **164** 233–45

[49] Wise S P and Jones E G 1976 The organization and postnatal development of the commissural projection of the rat somatic sensory cortex. *J. Comp. Neurol.* **168** 313–43

[50] Favorov O V, Whitsel B L, Chiu J S and Tommerdahl M 2006 Activation of cat SII cortex by flutter stimulation of contralateral vs. ipsilateral forepaws. *Brain Res.* **1071** 81–90

[51] Brooks V B, Rudomin P and Slayman C L 1961 Peripheral receptive fields of neurons in the cat's cerebral cortex *J Neurophysiol* **24** 302–25

[52] Iwamura Y, Tanaka M, Iriki A, Taoka M and Toda T 2002 Processing of tactile and kinesthetic signals from bilateral sides of the body in the postcentral gyrus of awake monkeys. *Behav. Brain Res.* **135** 185–90

[53] Pelled G, Chuang K-H, Dodd S J and Koretsky A P 2007 Functional MRI detection of bilateral cortical reorganization in the rodent brain following peripheral nerve deafferentation. *Neuroimage* **37** 262–73

[54] Engineer N D, Percaccio C R, Pandya P K, Moucha R, Rathbun D L and Kilgard M P 2004 Environmental enrichment improves response strength, threshold, selectivity, and latency of auditory cortex neurons. *J. Neurophysiol.* **92** 73–82

[55] Clarey J C, Tweedale R and Calford M B 1996 Interhemispheric modulation of somatosensory receptive fields: evidence for plasticity in primary somatosensory cortex. *Cereb. Cortex* **6** 196–206

[56] Sur M, Garraghty P and Roe A 1988 Experimentally induced visual projections into auditory thalamus and cortex *Science (80-.).* **242** 1437–41

[57] Kalaska J and Pomeranz B 1979 Chronic paw denervation causes an age-dependent appearance of novel responses from forearm in "paw cortex" of kittens and adult cats. *J. Neurophysiol.* **42** 618–33

[58] Florence S L, Jain N, Pospichal M W, Beck P D, Sly D L and Kaas J H 1996 Central reorganization of sensory pathways following peripheral nerve regeneration in fetal monkeys. *Nature* **381** 69–71

[59] McCandlish C A, Li C X, Waters R S and Howard E M 1996 Digit removal leads to discrepancies between the structural and functional organization of the forepaw barrel subfield in layer IV of rat primary somatosensory cortex. *Exp. Brain Res.* **108** 417–26

[60] Rasmusson D D 1982 Reorganization of raccoon somatosensory cortex following removal of the fifth digit. *J. Comp. Neurol.* **205** 313–26

[61] Merzenich M M, Nelson R J, Stryker M P, Cynader M S, Schoppmann A and Zook J M 1984 Somatosensory cortical map changes following digit amputation in adult monkeys. *J. Comp. Neurol.* **224** 591–605

[62] Pearson P P, Arnold P B, Oladehin A, Li C X and Waters R S 2001 Large-scale cortical reorganization following forelimb deafferentation in rat does not involve plasticity of intracortical connections *Exp. Brain Res.* **138** 8–25

[63] Pearson P P, Li C X, Chappell T D and Waters R S 2003 Delayed reorganization of the shoulder representation in forepaw barrel subfield (FBS) in first somatosensory cortex (SI) following forelimb deafferentation in adult rats. *Exp. Brain Res.* **153** 100–12

[64] Allard T, Clark S A, Jenkins W M and Merzenich M M 1991 Reorganization of somatosensory area 3b representations in adult owl monkeys after digital syndactyly. *J. Neurophysiol.* **66** 1048–58

[65] Hebb D O 1949 *The organization of behavior: A neuropsychological theory* (New York: Wiley)

[66] Bliss T V and Collingridge G L 1993 A synaptic model of memory: long-term potentiation in the hippocampus. *Nature* **361** 31–9

[67] Aroniadou-Anderjaska V and Keller A 1995 LTP in the barrel cortex of adult rats *Neuroreport* **6** 2297–300

[68] Banerjee A, González-Rueda A, Sampaio-Baptista C, Paulsen O and Rodríguez-Moreno A 2014 Distinct mechanisms of spike timing-dependent LTD at vertical and horizontal inputs onto L2/3 pyramidal neurons in mouse barrel cortex. *Physiol. Rep.* **2** e00271

[69] Jackson A, Mavoori J and Fetz E E 2006 Long-term motor cortex plasticity induced by an electronic neural implant. *Nature* **444** 56–60

[70] Recanzone G H, Merzenich M M and Dinse H R 1992 Expansion of the cortical representation of a specific skin field in primary somatosensory cortex by intracortical microstimulation. *Cereb. Cortex* **2** 181–96

[71] Dinse H R, Recanzone G H and Merzenich M M 1993 Alterations in correlated activity parallel ICMS-induced representational plasticity. *Neuroreport* **5** 173–6

[72] Kalarickal G J and Marshall J A 2002 Rearrangement of receptive field topography after intracortical and peripheral stimulation: the role of plasticity in inhibitory pathways. *Network* **13** 1–40

[73] Heusler P, Cebulla B, Boehmer G and Dinse H R 2000 A repetitive intracortical microstimulation pattern induces long-lasting synaptic depression in brain slices of the rat primary somatosensory cortex. *Exp. Brain Res.* **135** 300–10

[74] Bogdanova O and Sil'kis I 2002 Post-tetanic modification of the efficiency of excitatory transmission in neural networks including interhemispheric connections *Neurosci. Behav. Physiol.* **32** 15–24

[75] Quairiaux C, Armstrong-James M and Welker E 2007 Modified sensory processing in the barrel cortex of the adult mouse after chronic whisker stimulation. *J. Neurophysiol.* **97** 2130–47

[76] Li C X, Callaway J C and Waters R S 2002 Removal of GABAergic inhibition alters subthreshold input in neurons in forepaw barrel subfield (FBS) in rat first somatosensory cortex (SI) after digit stimulation. *Exp. Brain Res.* **145** 411–28

[77] Fuchs J L and Salazar E 1998 Effects of whisker trimming on GABA(A) receptor binding in the barrel cortex of developing and adult rats. *J. Comp. Neurol.* **395** 209–16

[78] Lane R D, Killackey H P and Rhoades R W 1997 Blockade of GABAergic inhibition reveals reordered cortical somatotopic maps in rats that sustained neonatal forelimb removal. *J. Neurophysiol.* **77** 2723–35

[79] Salin P A and Prince D A 1996 Electrophysiological mapping of GABAA receptor-mediated inhibition in adult rat somatosensory cortex. *J. Neurophysiol.* **75** 1589–600

[80] Perrenoud Q, Rossier J, Geoffroy H, Vitalis T and Gallopin T 2013 Diversity of GABAergic interneurons in layer VIa and VIb of mouse barrel cortex. *Cereb. Cortex* **23** 423–41

[81] Dykes R W, Landry P, Metherate R and Hicks T P 1984 Functional role of GABA in cat primary somatosensory cortex: shaping receptive fields of cortical neurons. *J. Neurophysiol.* **52** 1066–93

[82] Glazewski S, Herman C and McKenna M 1998 Long-term potentiation in vivo in layers II/III of rat barrel cortex *Neuropharmacology* **37** 581–92

[83] Stewart D H, Preston J B and Whitlock D G 1968 Spinal pathways mediating motor cortex evoked excitability changes in segmental motoneurons in pyramidal cats. *J. Neurophysiol.* **31** 928–37

[84] Stewart D H and Preston J B 1968 Spinal pathways mediating motor cortex evoked excitability changes in segmental motoneurons in pyramidal primates. *J. Neurophysiol.* **31** 938–46

[85] Cooke D F, Padberg J, Zahner T and Krubitzer L 2012 The functional organization and cortical connections of motor cortex in squirrels. *Cereb. Cortex* **22** 1959–78

[86] Griffin D M, Hudson H M, Belhaj-Saïf A and Cheney P D 2014 EMG activation patterns associated with high frequency, long-duration intracortical microstimulation of primary motor cortex. *J. Neurosci.* **34** 1647–56

[87] Seong H Y, Cho J Y, Choi B S, Min J K, Kim Y H, Roh S W, Kim J H and Jeon S R 2014 Analysis on bilateral hindlimb mapping in motor cortex of the rat by an intracortical microstimulation method. *J. Korean Med. Sci.* **29** 587–92

[88] Van Acker G M, Amundsen S L, Messamore W G, Zhang H Y, Luchies C W and Cheney P D 2014 Equilibrium-based movement endpoints elicited from primary motor cortex using repetitive microstimulation. *J. Neurosci.* **34** 15722–34

[89] Yumiya H, Larsen K D and Asanuma H 1979 Motor readjustment and input-output relationship of motor cortex following cross-connection of forearm muscles in cats. *Brain Res.* **177** 566–70

[90] Ozen L J and Teskey G C 2009 One hertz stimulation to the corpus callosum quenches seizure development and attenuates motor map expansion. *Neuroscience* **160** 567–75

[91] Stepniewska I, Fang P-C Y and Kaas J H 2009 Organization of the posterior parietal cortex in galagos: I. Functional zones identified by microstimulation. *J. Comp. Neurol.* **517** 765–82

[92] Avivi-Arber L, Lee J-C and Sessle B J 2010 Effects of incisor extraction on jaw and tongue motor representations within face sensorimotor cortex of adult rats. *J. Comp. Neurol.* **518** 1030–45

[93] Smith N J, Horst N K, Liu B, Caetano M S and Laubach M 2010 Reversible Inactivation of Rat Premotor Cortex Impairs Temporal Preparation, but not Inhibitory Control, During Simple Reaction-Time Performance. *Front. Integr. Neurosci.* **4** 124

[94] Rousche P J and Normann R A 1999 Chronic intracortical microstimulation (ICMS) of cat sensory cortex using the Utah Intracortical Electrode Array. *IEEE Trans. Rehabil. Eng.* **7** 56–68

[95] Anderson T R, Hu B, Iremonger K and Kiss Z H T 2006 Selective attenuation of afferent synaptic transmission as a mechanism of thalamic deep brain stimulation-induced tremor arrest. *J. Neurosci.* **26** 841–50

[96] Hatanaka N, Tokuno H, Nambu A, Inoue T and Takada M 2005 Input-output organization of jaw movement-related areas in monkey frontal cortex. *J. Comp. Neurol.* **492** 401–25

[97] Fang P-C, Stepniewska I and Kaas J H 2006 The thalamic connections of motor, premotor, and prefrontal areas of cortex in a prosimian primate (Otolemur garnetti). *Neuroscience* **143** 987–1020

[98] Lee S M and Ebner F F 1992 Induction of high frequency activity in the somatosensory thalamus of rats in vivo results in long-term potentiation of responses in SI cortex *Exp. brain Res.* **90** 253–61

[99] Decosta-Fortune T M 2013 *Telemetry Controlled Brain Machine Interface to Train Cortical Circuits* (Thesis: University of Memphis)

[100] Ziegler-Graham K, MacKenzie E J, Ephraim P L, Travison T G and Brookmeyer R 2008 Estimating the prevalence of limb loss in the United States: 2005 to 2050. *Arch. Phys. Med. Rehabil.* **89** 422–9

[101] Ephraim P L, Wegener S T, MacKenzie E J, Dillingham T R and Pezzin L E 2005 Phantom pain, residual limb pain, and back pain in amputees: results of a national survey. *Arch. Phys. Med. Rehabil.* **86** 1910–9

[102] (NIS) H N I S 2009 *Healthcare Cost and Utilization Project (HCUP)* (Rockville, MD)

[103] Clark R L, Bowling F L, Jepson F and Rajbhandari S 2013 Phantom limb pain after amputation in diabetic patients does not differ from that after amputation in nondiabetic patients. *Pain* **154** 729–32

[104] Dijkstra P U, Geertzen J H B, Stewart R and van der Schans C P 2002 Phantom pain and risk factors: a multivariate analysis. *J. Pain Symptom Manage.* **24** 578–85

[105] Go A S, Mozaffarian D, Roger V L, Benjamin E J, Berry J D, Blaha M J, Dai S, Ford E S, Fox C S, Franco S, Fullerton H J, Gillespie C, Hailpern S M, Heit J A, Howard V J, Huffman M D, Judd S E, Kissela B M, Kittner S J, Lackland D T, Lichtman J H, Lisabeth L D, Mackey R H, Magid D J, Marcus G M, Marelli A, Matchar D B, McGuire D K, Mohler E R, Moy C S, Mussolino M E, Neumar R W, Nichol G, Pandey D K, Paynter N P, Reeves M J, Sorlie P D, Stein J, Towfighi A, Turan T N, Virani S S, Wong N D, Woo D and Turner M B 2014 Heart disease and stroke statistics--2014 update: a report from the American Heart Association. *Circulation* **129** e28–292

[106] Brown D L, Boden-Albala B, Langa K M, Lisabeth L D, Fair M, Smith M A, Sacco R L and Morgenstern L B 2006 Projected costs of ischemic stroke in the United States. *Neurology* **67** 1390–5

[107] Flor H, Elbert T, Mühlnickel W, Pantev C, Wienbruch C and Taub E 1998 Cortical reorganization and phantom phenomena in congenital and traumatic upper-extremity amputees. *Exp. Brain Res.* **119** 205–12

[108] Flor H, Elbert T, Knecht S, Wienbruch C, Pantev C, Birbaumer N, Larbig W and Taub E 1995 Phantom-limb pain as a perceptual correlate of cortical reorganization following arm amputation. *Nature* **375** 482–4

[109] Lotze M, Flor H, Grodd W, Larbig W and Birbaumer N 2001 Phantom movements and pain. An fMRI study in upper limb amputees. *Brain* **124** 2268–77

[110] Boström K J, de Lussanet M H E, Weiss T, Puta C and Wagner H 2014 A computational model unifies apparently contradictory findings concerning phantom pain. *Sci. Rep.* **4** 5298

[111] Schaechter J D, Moore C I, Connell B D, Rosen B R and Dijkhuizen R M 2006 Structural and functional plasticity in the somatosensory cortex of chronic stroke patients. *Brain* **129** 2722–33

[112] Roiha K, Kirveskari E, Kaste M, Mustanoja S, Mäkelä J P, Salonen O, Tatlisumak T and Forss N 2011 Reorganization of the primary somatosensory cortex during stroke recovery. *Clin. Neurophysiol.* **122** 339–45

[113] Murphy T H and Corbett D 2009 Plasticity during stroke recovery: from synapse to behaviour. *Nat. Rev. Neurosci.* **10** 861–72

[114] Kerr A L, Cheng S-Y and Jones T A Experience-dependent neural plasticity in the adult damaged brain. *J. Commun. Disord.* **44** 538–48

[115] Stanslaski S, Cong P, Carlson D, Santa W, Jensen R, Molnar G, Marks W J, Shafquat A and Denison T 2009 An implantable bi-directional brain-machine interface system for chronic neuroprosthesis research. *Conf. Proc. IEEE Eng. Med. Biol. Soc.* **2009** 5494–7

[116] Patrick E, Sankar V, Rowe W, Sanchez J C and Nishida T 2009 Design of an implantable intracortical microelectrode system for brain-machine interfaces *2009 4th Int. IEEE/EMBS Conf. Neural Eng.* 379–82

[117] Chih-Kuo Liang et al 2005 An implantable bi-directional wireless transmission system for transcutaneous biological signal recording *Physiol. Meas.* **26** 83

[118] Venkatraman S, Elkabany K, Long J D, Yao Y and Carmena J M 2009 A system for neural recording and closed-loop intracortical microstimulation in awake rodents. *IEEE Trans. Biomed. Eng.* **56** 15–22

[119] Rolston J D, Gross R E and Potter S M 2009 A low-cost multielectrode system for data acquisition enabling real-time closed-loop processing with rapid recovery from stimulation artifacts. *Front. Neuroeng.* **2** 12

[120] Li Y 2007 *An Integragted Multichannel Neural Recording System with Spike Outputs* (Thesis: University of Florida)

[121] Chen T C, Chen K, Yang Z, Cockerham K and Liu W 2009 A biomedical multiprocessor soc for closed-loop neuroprosthetic applications *Solid-State Circuits Conference-Digest of Technical Papers, 2009. ISSCC 2009. IEEE International* (IEEE) pp 434–5

[122] Sooksood K, Stieglitz T and Ortmanns M 2009 An experimental study on passive charge balancing *Adv. Radio Sci.* 197–200

[123] Müller J, Bakkum D J and Hierlemann A 2012 Sub-millisecond closed-loop feedback stimulation between arbitrary sets of individual neurons. *Front. Neural Circuits* **6** 121

[124] Xu S, Talwar S K, Hawley E S, Li L and Chapin J K 2004 A multi-channel telemetry system for brain microstimulation in freely roaming animals. *J. Neurosci. Methods* **133** 57–63

[125] Hawley E S, Hargreaves E L, Kubie J L, Rivard B and Muller R U 2002 Telemetry system for reliable recording of action potentials from freely moving rats. *Hippocampus* **12** 505–13

[126] Wise K D 2004 Wireless Implantable Microsystems: High-Density Electronic Interfaces to the Nervous System *Proc. IEEE* **BME-34** 499–97

[127] Feng Z, Chen W, Ye X, Zhang S, Zheng X, Wang P, Jiang J, Jin L, Xu Z, Liu C, Liu F, Luo J, Zhuang Y and Zheng X 2007 A remote control training system for rat navigation in complicated environment *J. Zhejiang Univ. Sci. A* **8** 323–30

[128] Wang M, Song Y, Suen J, Zhao Y, Jia A and Zhu J 2010 A telemetery system for neuronal signal acquiring and processing *IEEE Computer Society* vol 28 pp 49–53

[129] Ye X, Wang P, Liu J, Zhang S, Jiang J, Wang Q, Chen W and Zheng X 2008 A portable telemetry system for brain stimulation and neuronal activity recording in freely behaving small animals. *J. Neurosci. Methods* **174** 186–93

[130] Fernando N X, Macklin D N, Hsu M Y and Judy J W 2007 An Embedded Wireless Neural Stimulation and Recording System *2007 3rd Int. IEEE/EMBS Conf. Neural Eng.* 333–6

[131] Jackson A, Moritz C T, Mavoori J, Lucas T H and Fetz E E 2006 The Neurochip BCI: towards a neural prosthesis for upper limb function. *IEEE Trans. Neural Syst. Rehabil. Eng.* **14** 187–90

[132] Mavoori J, Jackson A, Diorio C and Fetz E 2005 An autonomous implantable computer for neural recording and stimulation in unrestrained primates. *J. Neurosci. Methods* **148** 71–7

[133] Schregardus D S, Pieneman A W, Ter Maat A, Jansen R F, Brouwer T J F and Gahr M L 2006 A lightweight telemetry system for recording neuronal activity in freely behaving small animals. *J. Neurosci. Methods* **155** 62–71

[134] Chestek C a, Gilja V, Nuyujukian P, Kier R J, Solzbacher F, Ryu S I, Harrison R R and Shenoy K V 2009 HermesC: low-power wireless neural recording system for freely moving primates. *IEEE Trans. Neural Syst. Rehabil. Eng.* **17** 330–8

[135] Farshchi S 2006 *An Embedded-System Architecture for Wireless Neural Recording* (Thesis: University of California, LA)

[136] Gregory J A, Borna A, Roy S, Wang X, Lewandowski B, Schmidt M and Najafi K 2009 Low-cost wireless neural recording system and software. *Conf. Proc. IEEE Eng. Med. Biol. Soc.* **2009** 3833–6

[137] Arfin S K, Long M A, Fee M S and Sarpeshkar R 2009 Wireless neural stimulation in freely behaving small animals. *J. Neurophysiol.* **102** 598–605

[138] Harrison R R, Watkins P T, Kier R J, Lovejoy R O, Black D J, Greger B and Solzbacher F 2007 A Low-Power Integrated Circuit for a Wireless 100-Electrode Neural Recording System *IEEE J. Solid-State Circuits* **42** 123–33

[139] Farshchi S, Markovic D, Pamarti S, Razavi B and Judy J W 2007 Towards neuromote: a single-chip, 100-channel, neural-signal acquisition, processing, and telemetry device. *Conf. Proc. IEEE Eng. Med. Biol. Soc.* **2007** 437–40

[140] Fan D, Rich D, Holtzman T, Ruther P, Dalley J W, Lopez A, Rossi M A, Barter J W, Salas-Meza D, Herwik S, Holzhammer T, Morizio J and Yin H H 2011 A wireless multi-channel recording system for freely behaving mice and rats. *PLoS One* **6** e22033

[141] Albet Torres B 2011 *Wireless system for the measurement of bioelectric signals using capacitive electrodes* (Thesis: Universitat Politècnica de Catalunya)

[142] Chae M S, Yang Z, Yuce M R, Hoang L and Liu W 2009 A 128-channel 6 mW wireless neural recording IC with spike feature extraction and UWB transmitter. *IEEE Trans. Neural Syst. Rehabil. Eng.* **17** 312–21

[143] Zanos S, Richardson A G, Shupe L, Miles F P and Fetz E E 2011 The neurochip-2: an autonomous head-fixed computer for recording and stimulating in freely behaving monkeys. *IEEE Trans. Neural Syst. Rehabil. Eng.* **19** 427–35

[144] Fernando N X 2008 *Miniature Wireless Neural Stimulating and Recording System* (Thesis: University of California, LA)

[145] Harrison R R, Kier R J, Member S, Chestek C A, Gilja V, Nuyujukian P, Ryu S, Greger B, Solzbacher F, Shenoy K V, Member S and Terms I 2009 Wireless neural recording with single low-power integrated circuit *Rehabilitation* **17** 322–9

[146] Hampson R E, Collins V and Deadwyler S A 2009 A wireless recording system that utilizes Bluetooth technology to transmit neural activity in freely moving animals. *J. Neurosci. Methods* **182** 195–204

[147] Aghagolzadeh M, Zhang F and Oweiss K 2010 An implantable VLSI architecture for real time spike sorting in cortically controlled Brain Machine Interfaces. *Conf. Proc. IEEE Eng. Med. Biol. Soc.* **2010** 1569–72

[148] Harrison R R, Fotowat H, Chan R, Kier R J, Olberg R, Leonardo A and Gabbiani F 2011 Wireless Neural/EMG Telemetry Systems for Small Freely Moving Animals *IEEE Trans. Biomed. Circuits Syst.* **5** 103–11

[149] Bagheri a., Gabran S R I, Salam M T, Perez Velazquez J L, Mansour R R, Salama M M a. and Genov R 2012 1024-Channel-Scalable Wireless Neuromonitoring and

Neurostimulation Rodent Headset With Nanotextured Flexible Microelectrodes *2012 IEEE Biomed. Circuits Syst. Conf.* 184–7

[150] Farshchi S, Nuyujukian P H, Pesterev A, Mody I and Judy J W 2006 A TinyOS-enabled MICA2-based wireless neural interface. *IEEE Trans. Biomed. Eng.* **53** 1416–24

[151] Gosselin B 2011 Approaches for the efficient extraction and processing of biopotentials in implantable neural interfacing microsystems. *Conf. Proc. IEEE Eng. Med. Biol. Soc.* **2011** 5855–9

[152] Harrison R R 2008 The Design of Integrated Circuits to Observe Brain Activity *Proc. IEEE* **96** 1203–16

[153] Dac M, Diogo S and Disserta P C 2012 *Microelectronics Circuits for Neuronal Sensing and Stimulation Engenharia Eletrotécnica e de Computadores*

[154] Sooksood K, Noorsal E, Bihr U and Ortmanns M 2012 Recent advances in power efficient output stage for high density implantable stimulators. *Conf. Proc. IEEE Eng. Med. Biol. Soc.* **2012** 855–8

[155] Bu B, Bouwens F, Konijnenburg M, De Nil M, Ashouei M, Hulzink J, Zhou J, Stuyt J, Huisken J, de Groot H, Santana O, Abbo A, Yseboodt L, van Meerbergen J and Bennebroek M 2010 Ultra Low Power programmable biomedical SoC for on-body ECG and EEG processing *2010 IEEE Asian Solid-State Circuits Conference* (IEEE) pp 1–4

[156] Liu W, Chae M S, Yang Z and Kim H 2009 Design of advanced neuroscience platform. *Conf. Proc. IEEE Eng. Med. Biol. Soc.* **2009** 5535–8

[157] Majidzadeh V, Schmid A and Leblebici Y 2011 Energy Efficient Low-Noise Neural Recording **5** 262–71

[158] De Lima J a. and Cordeiro A S 2001 A simple constant-current neural stimulator with accurate pulse-amplitude control *2001 Conf. Proc. 23rd Annu. Int. Conf. IEEE Eng. Med. Biol. Soc.* 1328–31

[159] Sawigun C, Ngamkham W, van Dongen M and Wouter a. S 2010 A least-voltage drop high output resistance current source for neural stimulation *2010 Biomed. Circuits Syst. Conf.* 110–3

[160] Sit J and Sarpeshkar R 2007 A Low-Power Blocking-Capacitor-Free With Less Than 6 nA DC Error for 1-mA *IEEE Trans. Biomed. Circuits Syst.* **1** 172–83

[161] Ghovanloo M and Najafi K 2005 A compact large voltage-compliance high output-impedance programmable current source for implantable microstimulators. *IEEE Trans. Biomed. Eng.* **52** 97–105

[162] Constandinou T G, Georgiou J and Toumazou C 2008 A Partial-Current-Steering Biphasic Stimulation Driver for Vestibular Prostheses *IEEE Trans. Biomed. Circuits Syst.* **2** 106–13

[163] Hafkemeyer K M, Galjan W, Tomasik J M, Schroeder D and Krautschneider W H 2007 System-on-Chip Approach for Biomedical Signal Acquisition *Proc. ProRISC Workshop* pp 26–9

[164] Gosselin B, Simard V, Roy J-F J F, Marrouche W, Dumortier C and Sawan M 2004 Multichannel wireless cortical recording: circuits, system design and assembly challenges *Biomedical Circuits and Systems, 2004 IEEE International Workshop on* (Ieee) pp 365–8

[165] Amara A, Amiel F and Ea T 2006 FPGA vs. ASIC for low power applications *Microelectronics J.* **37** 669–77

[166] Zemelman B V, Lee G A, Ng M and Miesenböck G 2002 Selective photostimulation of genetically chARGed neurons. *Neuron* **33** 15–22

[167] Deng W, Goldys E M, Farnham M M and Pilowsky P M 2014 Optogenetics, the intersection between physics and neuroscience: Light stimulation of neurons in physiological conditions. *Am. J. Physiol. Regul. Integr. Comp. Physiol.* **307** ajpregu.00072.2014

[168] Zhu Y, Feng B, Schwartz E S, Gebhart G F and Prescott S A 2015 Novel method to assess axonal excitability using channelrhodopsin-based photoactivation. *J. Neurophysiol.* jn.00982.2014

[169] Kim T, McCall J G, Jung Y H, Huang X, Siuda E R, Li Y, Song J, Song Y M, Pao H A, Kim R-H, Lu C, Lee S D, Song I-S, Shin G, Al-Hasani R, Kim S, Tan M P, Huang Y, Omenetto F G, Rogers J a and Bruchas M R 2013 Injectable, cellular-scale optoelectronics with applications for wireless optogenetics. *Science* **340** 211–6

[170] Terao Y and Ugawa Y 2002 Basic mechanisms of TMS. *J. Clin. Neurophysiol.* **19** 322–43

[171] Chen X L, Xiong Y Y, Xu G L and Liu X F 2013 Deep brain stimulation. *Interv. Neurol.* **1** 200–12

[172] Patel D M, Walker H C, Brooks R, Omar N, Ditty B and Guthrie B L 2015 Adverse Events Associated With Deep Brain Stimulation for Movement Disorders: Analysis of 510 Consecutive Cases. *Neurosurgery*

[173] Intan Technologies LLC 2012 Datasheet: RHD2000 Series Digital Electrophysiology Interface Chips 1–36

[174] Decosta-Fortune T, Li C-X, Curry A and Waters R 2010 Pattern of interhemispheric connections between forelimb representations in rat barrel field cortex *Soc. Neurosci. XXXVIIII Neurosci. Meet. Plan.*

[175] Armstrong-James M and Millar J 1979 Carbon fibre microelectrodes. *J. Neurosci. Methods* **1** 279–87

[176] Farfán F D, Politti J C and Felice C J 2010 Evaluation of EMG processing techniques using Information Theory. *Biomed. Eng. Online* **9** 72

[177] Beniczky S, Conradsen I, Moldovan M, Jennum P, Fabricius M, Benedek K, Andersen N, Hjalgrim H and Wolf P 2014 Quantitative analysis of surface electromyography during epileptic and nonepileptic convulsive seizures. *Epilepsia* **55** 1128–34

[178] Merletti R and Parker P A 2004 *Electromyography: Physiology, Engineering, and Non-Invasive Applications* (New Jersey: John Wiley & Sons, Inc.)

[179] DeCosta-Fortune T, Ramshur J, Curry A and Waters R 2012 Interactive neuronal embedded system for the controlled delivery of telemetry-based stimulation and real-time recordings *Society for Neuroscience 42nd Annual Meeting*

[180] Merrill D R, Bikson M and Jefferys J G R 2005 Electrical stimulation of excitable tissue: design of efficacious and safe protocols. *J. Neurosci. Methods* **141** 171–98

[181] Lempka S F, Durand D M, Mcintyre C C, Vitek J L, Kirsch R F and Taylor D M 2010 *The Electrode-Tissue Interface During Recording and Stimulation in the Central Nervous System*

[182] Hatsopoulos N G and Donoghue J P 2009 The science of neural interface systems. *Annu. Rev. Neurosci.* **32** 249–66

[183] Bergamini C M, Gambetti S, Dondi A and Cervellati C 2004 Oxygen, reactive oxygen species and tissue damage. *Curr. Pharm. Des.* **10** 1611–26

[184] Halliwell B 1992 Reactive oxygen species and the central nervous system. *J. Neurochem.* **59** 1609–23

[185] Stice P and Muthuswamy J 2009 Assessment of gliosis around moveable implants in the brain. *J. Neural Eng.* **6** 046004

[186] Kawano H, Kimura-Kuroda J, Komuta Y, Yoshioka N, Li H P, Kawamura K, Li Y and Raisman G 2012 Role of the lesion scar in the response to damage and repair of the central nervous system. *Cell Tissue Res.* **349** 169–80

[187] Mullen R J, Buck C R and Smith A M 1992 NeuN, a neuronal specific nuclear protein in vertebrates. *Development* **116** 201–11

[188] Lind G, Linsmeier C E and Schouenborg J 2013 The density difference between tissue and neural probes is a key factor for glial scarring. *Sci. Rep.* **3** 2942

[189] Biran R, Martin D C and Tresco P A 2005 Neuronal cell loss accompanies the brain tissue response to chronically implanted silicon microelectrode arrays. *Exp. Neurol.* **195** 115–26

[190] Grill W M 2008 Signal Considerations for Chronically Implanted Electrodes for Brain Interfacing *Indwelling Neural Implants: Strategies for Contending with the In Vivo Environment* ed W Reichert (Boca Raton, FL: CRC Press)

[191] Bignami A, Eng L F, Dahl D and Uyeda C T 1972 Localization of the glial fibrillary acidic protein in astrocytes by immunofluorescence. *Brain Res.* **43** 429–35

[192] Andjelkovic A V, Nikolic B, Pachter J S and Zecevic N 1998 Macrophages/microglial cells in human central nervous system during development: an immunohistochemical study. *Brain Res.* **814** 13–25

[193] Pulford K A, Sipos A, Cordell J L, Stross W P and Mason D Y 1990 Distribution of the CD68 macrophage/myeloid associated antigen. *Int. Immunol.* **2** 973–80

[194] Wanner I B, Anderson M A, Song B, Levine J, Fernandez A, Gray-Thompson Z, Ao Y and Sofroniew M V 2013 Glial scar borders are formed by newly proliferated, elongated astrocytes that interact to corral inflammatory and fibrotic cells via STAT3-dependent mechanisms after spinal cord injury. *J. Neurosci.* **33** 12870–86

[195] Taub A H, Hogri R, Magal A, Mintz M and Shacham-Diamand Y 2012 Bioactive anti-inflammatory coating for chronic neural electrodes. *J. Biomed. Mater. Res. A* **100** 1854–8

[196] Goc J, Liu J Y W, Sisodiya S M and Thom M 2014 A spatiotemporal study of gliosis in relation to depth electrode tracks in drug-resistant epilepsy. *Eur. J. Neurosci.* **39** 2151–62

[197] Polikov V S, Tresco P A and Reichert W M 2005 Response of brain tissue to chronically implanted neural electrodes. *J. Neurosci. Methods* **148** 1–18

[198] Biran R, Martin D C and Tresco P A 2007 The brain tissue response to implanted silicon microelectrode arrays is increased when the device is tethered to the skull. *J. Biomed. Mater. Res. A* **82** 169–78

[199] Winslow B D, Christensen M B, Yang W-K, Solzbacher F and Tresco P A 2010 A comparison of the tissue response to chronically implanted Parylene-C-coated and uncoated planar silicon microelectrode arrays in rat cortex. *Biomaterials* **31** 9163–72

[200] McConnell G C, Butera R J and Bellamkonda R V 2009 Bioimpedance modeling to monitor astrocytic response to chronically implanted electrodes. *J. Neural Eng.* **6** 055005

Appendices

Appendix A: SRD Bill of Materials (BOM)

Part	Value	Manufacturer	Package	Description
LED1	TLMS1100-GS08	Vishay	0603	LED
Q1	MTD8000M3B-T	Marktech Optoelectronics	TH	IR Phototransistor
C41	10nF, X7R		0402	Capacitor
C31	1uF, X5R		0805	Capacitor
H10	A79043-001	Omnetics	18PIN-SMD	Omnetics 18 2Row Female, 2post
U2	AS1302	AMS	BGA9	5V Charge Pump w/ reg
U4	CY8C3866	Cypress	QFN68	PSoC
U9	DG9409DN	Vishay	QFN65	Analog Multiplexers
D2	UPS115UE3/TR7	Microsemi	DO-216AA	Protection Diode
RGB1	APTF1616SEJ3Z GGVBDC	Kingbright	SMD 1.6 x 1.6mm	RGB LED
U3	MAX865	Maximum	UMAX8	Dual output charge pump
U1	MIC5393	Micrel	THIN_DFN	Micrel High-Performance Dual 150mA LDO
Q2	OP501,DA	Optek	0805	Darlington IR transister
U6	RHD2216	Intan	QFN56	Electrophys Chip
U5	RN42-SM	Microchip	30-pin SMD	BT Module
SW1	KMR2	C&K	KMR2	Reset Button
BAT	2013499-1	TE Connectivity	USB-MICRO	USB Micro-B Plug
C23 C27	1uF, X7R		0402	Capacitor
C5 C6	2.2uF, X5R		0603	Capacitor
C8 C9	222nF, X7R		0402	Capacitor
C10 C11	3.3uF, X5R		0805	Capacitor
U7 U8	ALD1105	Analog Linear Devices	SO14	Matched pair MOSFET

C7 C30 C50 C51	0.1uF, X7R		0603	Capacitor
R23 R24 R31 R32	1k		0402	Resistor
C1 C2 C3 C4	1uF, X5R		0603	Capacitor
R20 R21 R22 R30	4.7k		0402	Resistor
C12 C13 C14 C15 C52 C53	10uF, X5R	Samsung	0805	Capacitor
C20 C21 C22 C24 C25 C26 C26A C28 C29 C40 C42	0.1uF, X7R		0402	Capacitor
PROG	52746-6	Molex	Ziff	Programming Header
AUX	52746-6	Molex	Ziff	Aux I/O Header
Battery	850 mAh	Sparkfun		LiPo Battery

Appendix B: PCB Copper Layout

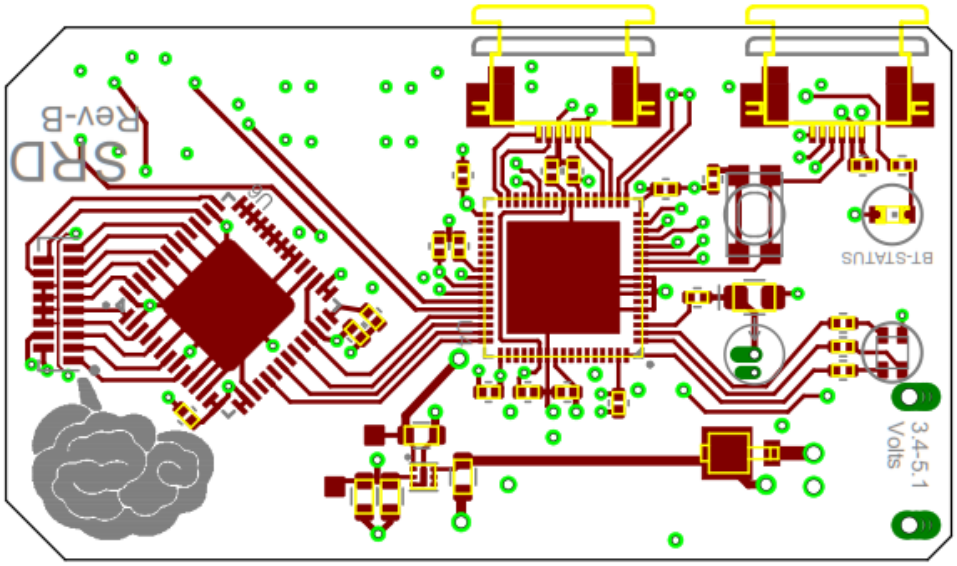

Figure B1. Top Copper Layer of SRD PCB

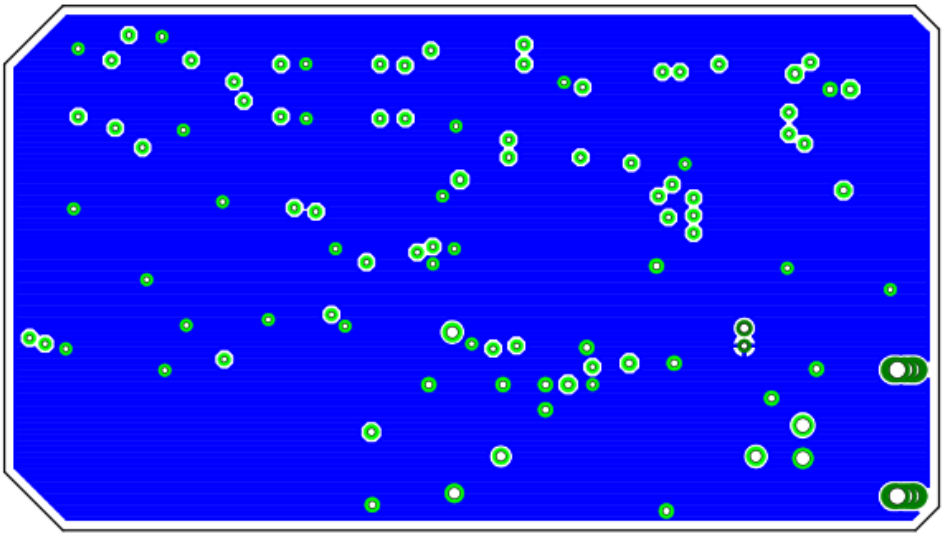

Figure B2. Layer II (GND) of SRD PCB

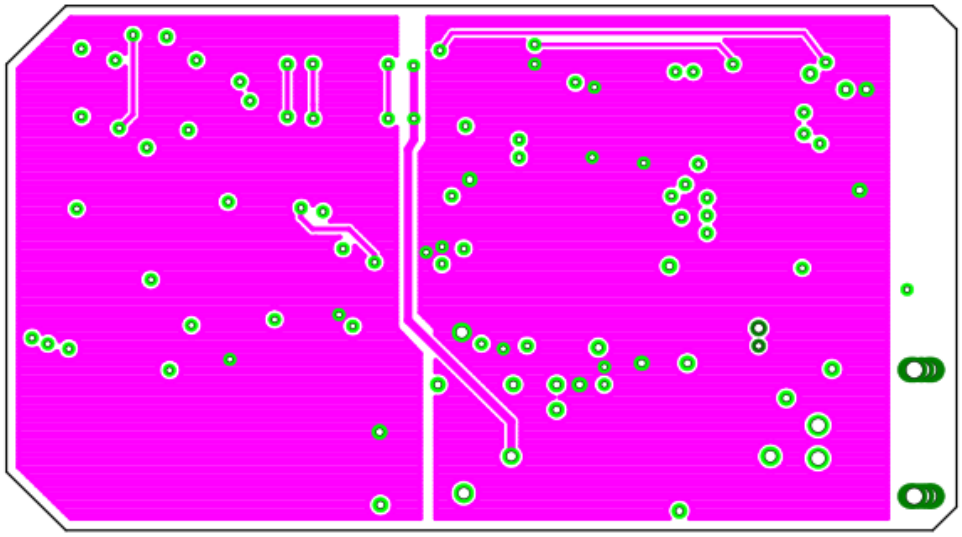

Figure B3. Layer III (VDDA and VDDD) of SRD PCB

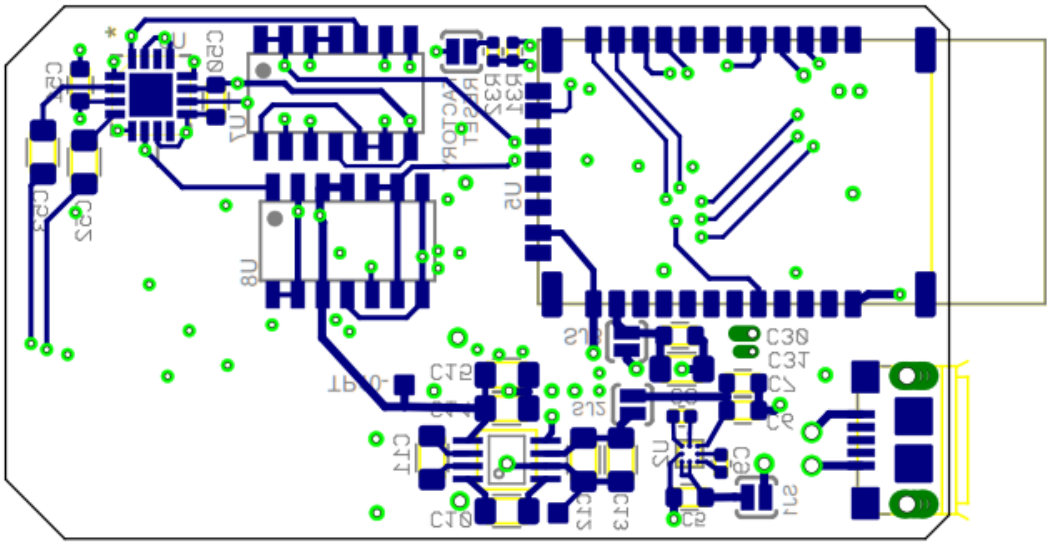

Figure B4. Bottom Copper Layer of SRD PCB

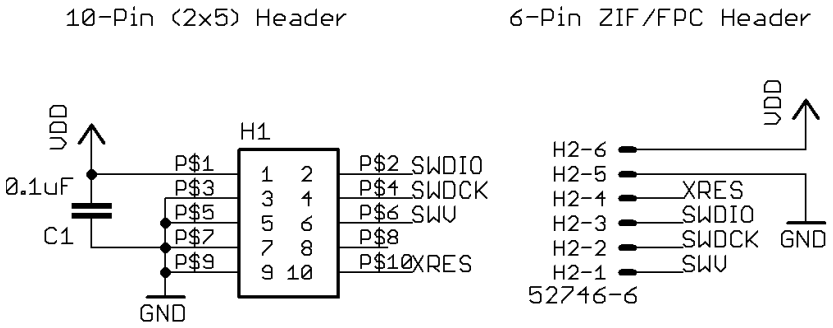

Figure C1. Schematic for the PSoC programming adaptor used for on-board PSoC programming.

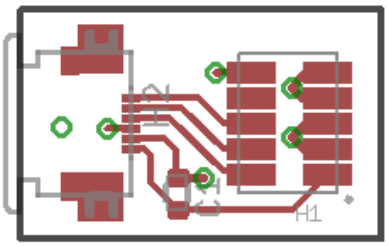

Figure C2. Top copper layer of the PSoC programming adaptor used for on-board PSoC programming.

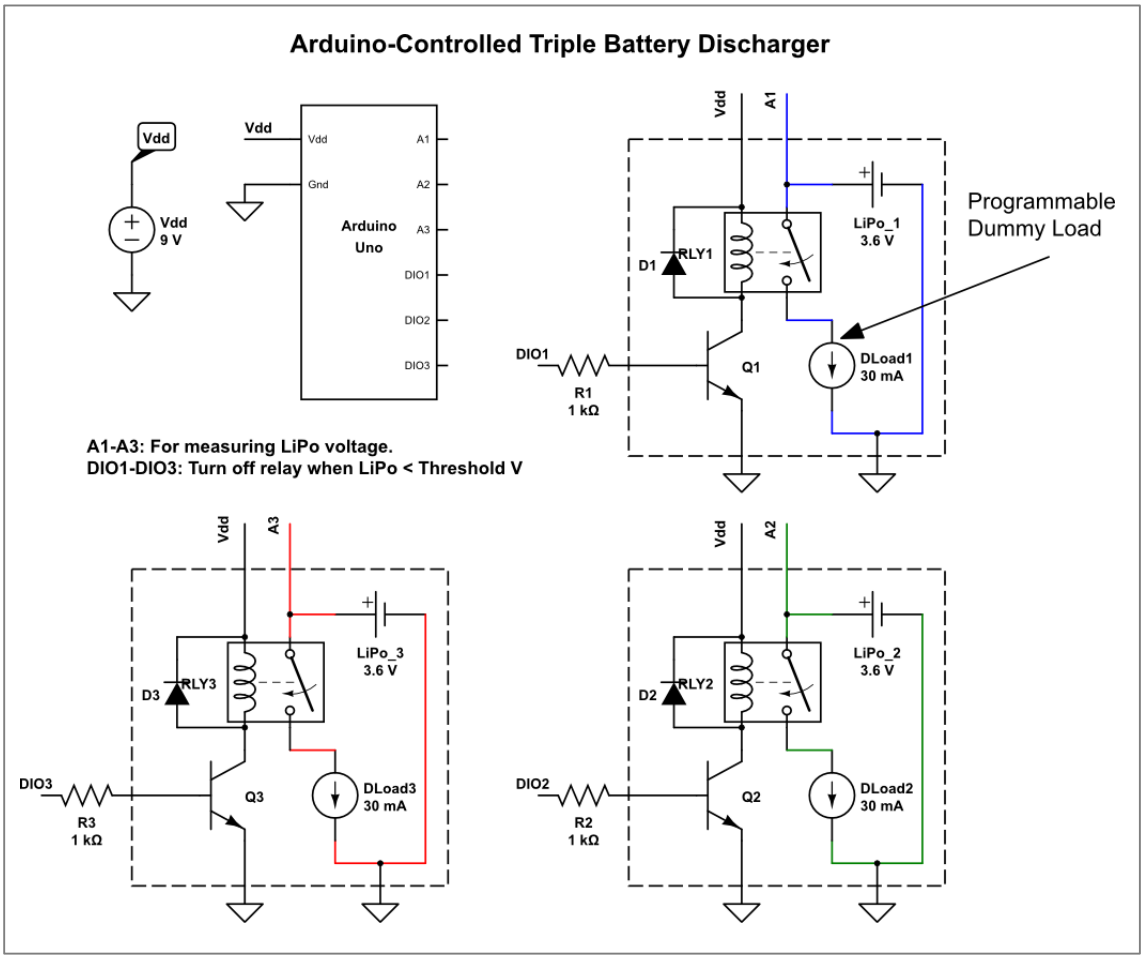

Figure D1. Hardware schematic used for bench testing the SRD battery discharge characteristics. Data (current and battery voltage) was logged using and Arduino Uno and Arduino SD card shield. Once the battery voltage dropped below 3.0 V the Arduino opened a relay that disconnected the battery from the load as to not damage the battery with excessive discharge. A programmable dummy load was used to set the testing current and to output a voltage related to the current passing through the dummy load.

Appendix E: Pictorial Sequence of Electrode Implantation

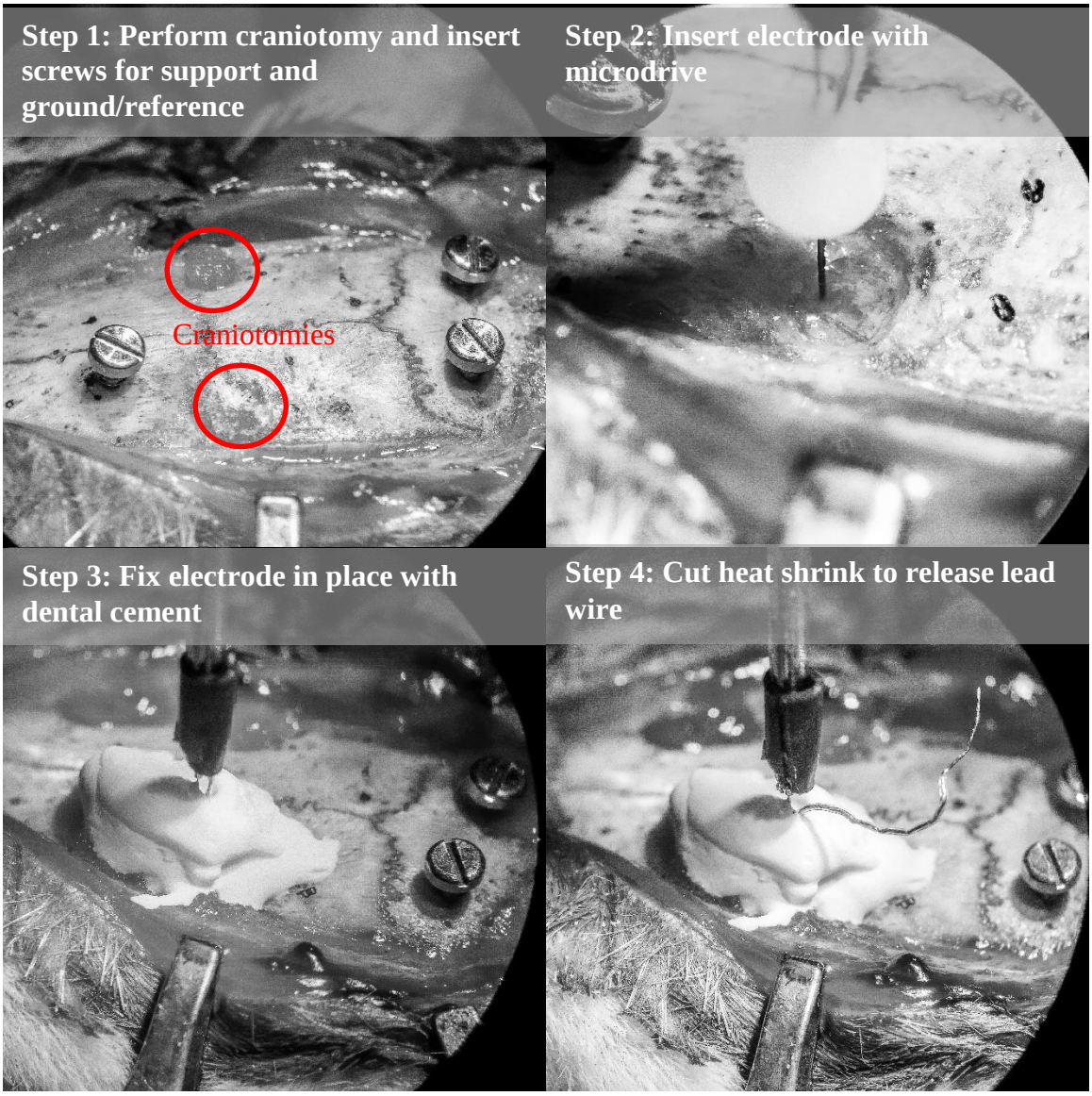

Step 5: Snip electrode shaft just above cement, and retract the electrode guide system

Step 6: Implant the second electrode following the previous steps.

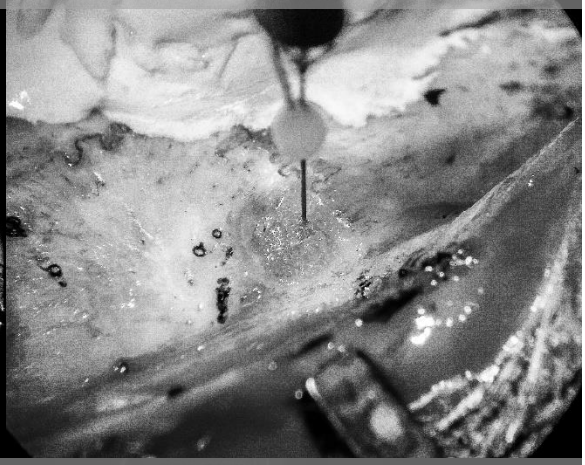

Step 7: Connect electrodes and ground/reference wires to EIB. Position EIB just above cement.

Step 8: Cover EIB and screws with dental cement using multiple small applications. Apply antibiotic

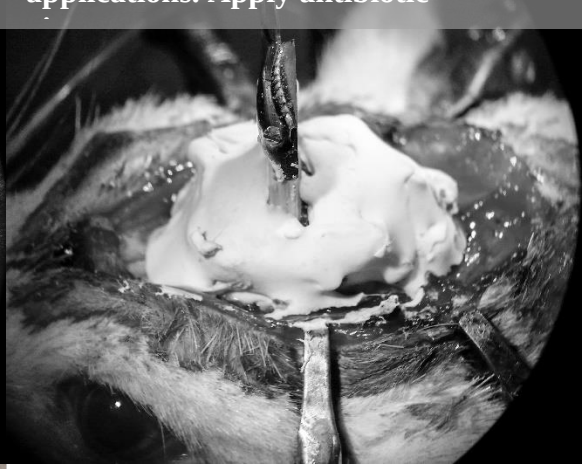

Step 9: Recovery